Designer Silica Layers for Advanced Applications: Processing and Properties

Except where reference is made to the work of others, the work described in this dissertation is my own or was done in collaboration with my advisory committee. This dissertation does not include proprietary or classified information.

Adam Anderson

Certificate of Approval:

Christopher B. Roberts
Uthlaut Professor
Chemical Engineering

William R. Ashurst, Chair
Assistant Professor
Chemical Engineering

Ram B. Gupta
Philpott and West Point Stevens Distinguished Professor
Chemical Engineering

Mark E. Byrne
Mary and John Sanders Associate Professor
Chemical Engineering

Aleksandr Simonian
Professor
Materials Engineering

George T. Flowers
Dean
Graduate School

Designer Silica Layers for Advanced Applications: Processing and Properties

Adam Anderson

A Dissertation

Submitted to

the Graduate Faculty of

Auburn University

in Partial Fulfillment of the

Requirements for the

Degree of

Doctor of Philosophy

Auburn, Alabama
May 9, 2009

Designer Silica Layers for Advanced Applications: Processing and Properties

Adam Anderson

Signature of Author

Date of Graduation

Vita

Adam Neil Anderson, son of Gary Neil and Christine Jones Anderson, was born October 22, 1980, in Montgomery, AL. He graduated from Jefferson Davis High School in 1999, and then entered Auburn University in August, 1999. Adam graduated *Magna Cum Laude* with a Bachelor of Chemical Engineering in August, 2003. After working in process automation for one year, Adam returned to Auburn University to pursue a doctoral degree in Chemical Engineering under the guidance of Dr. William R. Ashurst. Adam is married to Danette Michelle Anderson, and they have three wonderful sons, Gavin, Maddox, and Lucas.

Dissertation Abstract

Designer Silica Layers for Advanced Applications: Processing and Properties

Adam Anderson

Doctor of Philosophy, May 9, 2009
(B.Che., Auburn University–Auburn, 2003)

191 Typed Pages

Directed by William R. Ashurst

Recently, as scientists have investigated the application of conventional MEMS devices to biological systems, the exciting fields of bio-MEMS and microfluidics have emerged. Due to their small size, bio-MEMS and microfluidics devices offer the advantage of requiring only small sample and reagent volumes, in a potentially low-cost, integrated package. Such devices have the potential to significantly advance point-of-care diagnostics devices and improve overall patient care. However, due to the extremely small feature size, the large surface area-to-volume ratio in these devices makes controlling surface interactions of critical importance. Recently, there has been a shift to polymeric materials for fabrication of microfluidics devices due to their lower cost, ease of device fabrication by various processes, varied and favorable material properties, and, in some cases, pre-existing regulatory agency approvals. As a result, various surface modification strategies for polymeric surfaces have been proposed, but with only limited success.

The proven success of organosilicon-based precursors in a wide variety of surface modification strategies has been demonstrated, with a body of knowledge on the general subject dating back nearly fifty years. However, these proven methodologies cannot be transferred to many important polymeric materials due to a lack of sufficient reactive groups on the surface. If any polymer surface could be made reactive by some intermediate treatment,

the wide body of knowledge of organosilicon-based surface modification chemistries could be leveraged to advance the state-of-the-art in surface modification for microfluidics applications, where polymeric substrates are commonly encountered.

This thesis reports on the processing properties and chemical properties of a vapor deposited silica layer, which is formed from the vapor phase hydrolysis of silicon tetrachloride. This layer can be deposited at low temperatures to a wide variety of substrates, including glasses, metals, fibers, polymers, and plastics. This process has the potential to enable common organosilicon-based chemistries on polymer surfaces, but before the potential impact of this technology can be realized, the fundamental groundwork must be laid.

In this work, a series of investigations into the properties of the vapor deposited silica layer are conducted. It is determined that the morphology of the silica layer depends strongly on the relative pressures of the precursor gases. Furthermore, the vapor deposited silica layer has many commonalities with conventionally prepared silica materials (fumed or precipitated) and does support the formation of self-assembled monolayers for organosilicon-based precursors. However, there are also some differences in chemical reactivity of surface groups on the vapor deposited silica layer relative to the surface of conventionally prepared silica materials, which contribute to different chemical behavior in some circumstances. Also, the deposition of the silica layers under study here is confirmed on several model polymeric substrates by ATR-FTIR and atomic force microscopy.

Acknowledgments

First and foremost, I must thank my wonderful wife, Danette, for her patience, understanding, love, and unending support during my pursuit of this degree. Without her understanding and acceptance of my desire to pursue graduate studies, her willingness to put our lives on hold while I pursue this degree, her hard work in raising our children, and her constant encouragement, this degree, and the work detailed in this dissertation, would not have been possible. Danette, you are so wonderful, and I love you so much.

I must also express deep appreciation for the mentorship of my advisor, Dr. Bob Ashurst. Under his guidance, I have developed the necessary competencies to think as a scientist, and I have confidence that I will be able to solve any research problem that I may encounter in the future. For the many laughs, the many conversations, and for the guidance in completing this research–thank you.

I express gratitude to Dr. Shankar Balasubramanian and Mrs. Madhumati Ramanathan for their help with bacterial cell adhesion experiments, and protein adsorption experiments, respectively.

Finally, I thank the friends that I have made along the way–my labmates, Aimee Poda, Naveed Ansari, Sagar Gururaj, Kendall Hurst, and Mohammad Biswas. Thank all of you for making my tenure here enjoyable.

Style manual or journal used Journal of Approximation Theory (together with the style known as "aums"). Bibliography follows van Leunen's *A Handbook for Scholars*.

Computer software used The document preparation package TEX (specifically LATEX) together with the departmental style-file `auphd.sty`.

Table of Contents

List of Figures

Chapter 1

Introduction

1.1 Interfacial Engineering

Interfacial engineering, or surface modification, is a useful technique to change the surface properties of a material without significantly affecting its bulk properties. It has been employed in reducing friction and stiction in microelectromechanical (MEMS) devices [2–5], in altering surface wettability [6], in tethering biomolecules [7–11] and inorganic nanoparticles [12] to surfaces, and in reducing non-specific protein adsorption on surfaces [13–16] and in micro-channels [17–20].

Surface modification strategies have become increasingly important with the progression of MEMS devices. Surface microstructures in MEMS devices have lateral dimensions of 50–500 μm, thicknesses of 0.1–10 μm, and are raised 0.1–5 μm from the substrate surface. At this size scale, interfacial forces dominate body forces, and controlling interactions at the surfaces of these devices becomes critically important in improving their performance. For instance, surface modification of MEMS devices has been demonstrated to reduce the work of adhesion by over five orders of magnitude and to reduce the coefficient of static friction by over two orders of magnitude [2], thereby greatly improving their performance and reliability.

Recently, as scientists have investigated the application of conventional MEMS devices to biological systems, the exciting fields of bio-MEMS and microfluidics have emerged. Due to their small size, bio-MEMS and microfluidics devices offer the advantage of requiring only small sample and reagent volumes, in a potentially low-cost, integrated package. Hence, these devices are being increasingly investigated for assays, characterization, and sensing of biomolecules and organisms [20]. Presently, devices capable of recording from, sensing,

stimulating, and delivering to biological systems are being developed [21]. Although technology in this area is developing rapidly at the laboratory scale, commercialization of these technologies has been hindered by the inability of such devices to interact with biological systems in a non-immunogenic and stable manner [21]. Non-specific protein adsorption and cell adhesion, two processes that contribute to the phenomena known as biofouling, have proven especially problematic. Silicon microdevices, which can easily be fabricated from standard micromachining processes, are especially susceptible to this phenomena due to their negative surface charge at physiological pH [21]. Furthermore, biofouling has been shown to cause undesirable device function in various implantable microdevices, such as pH and glucose biosensors. Biofouling of subcutaneously implanted glucose biosensors developed by Nishida and coworkers resulted in loss of sensitivity, and *in vivo* recalibrations were required after seven days [22]. While monitoring tissue pH *in vivo* in canine hearts, Auerbach and coworkers noted questionable rises in pH as high as 0.2 pH units in as little as four hours, which they attributed to biofouling of the sensor [23].

In light of these considerations, much research has been aimed at improving the biocompatibility of bio-MEMS and microfluidics devices, and surface modification with molecular films has emerged as a promising approach. For instance, surface modification by organosilane precursors has been shown to alleviate non-specific protein adsorption on surfaces [13–16] and in micro-channels [17–20], to affect electroosmotic flow (EOF) [24], and to alleviate cell adhesion in microchannels [19, 20].

1.2 Silane Chemistry

Organosilane compounds consist of at least one silicon atom covalently bonded to an organic substituent, which is sometimes referred to as a pendant group. In order to be useful for surface modification, they must also consist of at least one chemically labile group that is either converted to a reactive intermediate, usually by hydrolysis, or which is displaced during reaction with the target surface. These groups are also bonded to the silicon atom, and this portion of the molecule is sometimes referred to as the head group. The chemical

functionality of the pendant group is transferred to the target surface after the head group forms a covalent bond to the surface. Some organosilanes commonly employed in various surface modification strategies are shown in figure 1.1.

The most common organosilane compounds for surface modification are chlorosilanes and alkoxysilanes. Chlorosilanes contain Si-Cl bonds in the head group, while alkoxysilanes usually contain either methoxy or ethoxy groups. For chlorosilanes, the Si-Cl bonds are hydrolyzed in the presence of trace water to Si-OH bonds (called silanols), which then condense with other -OH groups, resulting in the formation of an Si-O-Si linkage and the elimination of a water molecule. One notable drawback of this surface coating strategy is the likelihood of particulate formation, which can occur when the head group contains more than one Si-Cl bond. The hydrolysis of the Si-Cl bond is very rapid, and once the precursor molecules are hydrolyzed to the silanol state, they may react with other hydrolyzed precursor molecules, resulting in the formation of polymeric species. These species continue to grow until they precipitate out of solution and settle on the target surface. In general, particulate matter on the target surface is undesirable, especially for MEMS devices, and a conformal monolayer coating is preferred. As a result, trace water and ambient water must be strictly controlled, and bulk water must be absent. Surface modification reactions by chlorosilane precursors are generally described to proceed by a mechanism loosely depicted in figure 1.2, which abounds in literature on this topic.

When trace water is present, alkoxysilanes can also hydrolyze to reactive silanols, and then proceed by a mechanism very similar to the mechanism followed by chlorosilanes. The likelihood of particulate formation is lower than for chlorosilanes since the hydrolysis to the silanol state is much slower. In the absence of trace water, alkoxysilanes may interact with the target surface by forming hydrogen bonds with reactive surface groups. The condensation reaction can be catalyzed chemically, usually by amine bases, or driven thermally. Schematic representations of these mechanisms are shown in figure 1.3.

Dimethylaminosilanes are a relatively new class of organosilanes for surface modification. The head group of these molecules is comprised of a silicon atom bonded to three

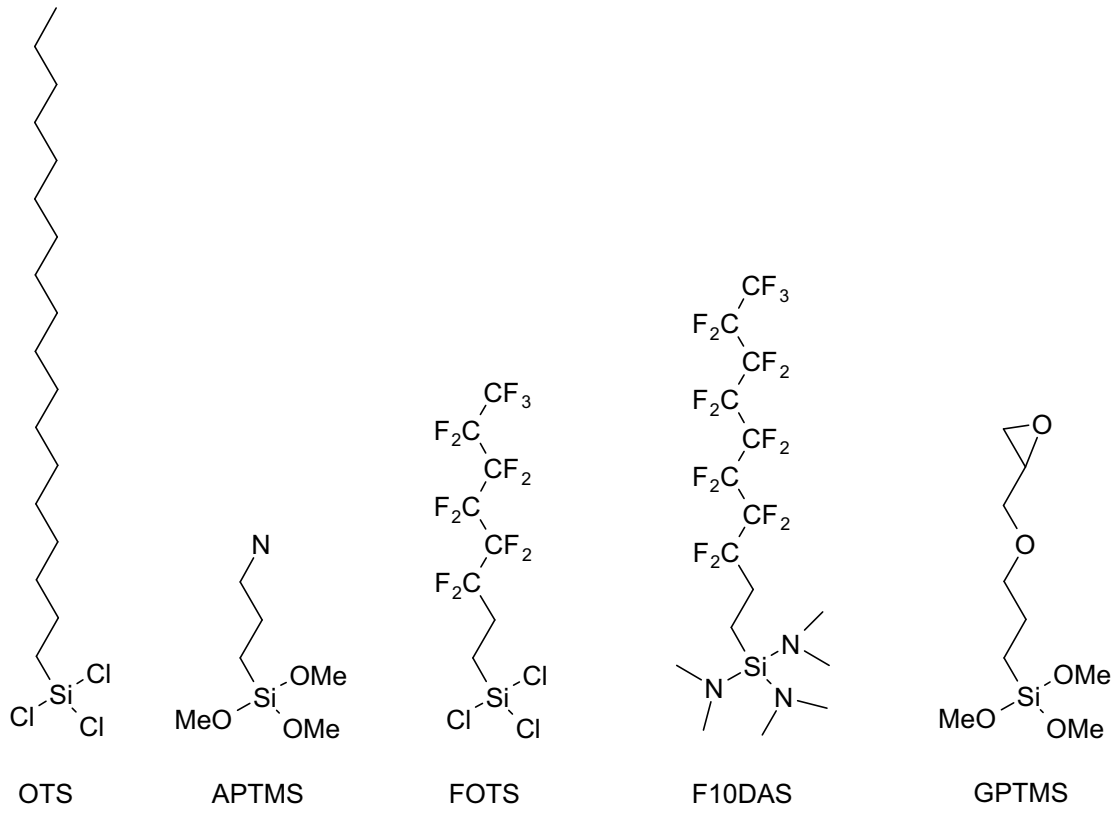

Figure 1.1: Schematic depicting some organosilane compounds commonly employed in various surface modification strategies. They are, from left to right: octadecyltrichlorosilane, 3-aminopropyltrimethoxysilane, (tridecafluoro-1,1,2,2-tetrahydrooctyl)trichlorosilane, (heptadecafluoro-1,1,2,2-tetrahydrodecyl)tris-dimethylaminosilane, and 3-glycidoxypropyltrimethoxysilane.

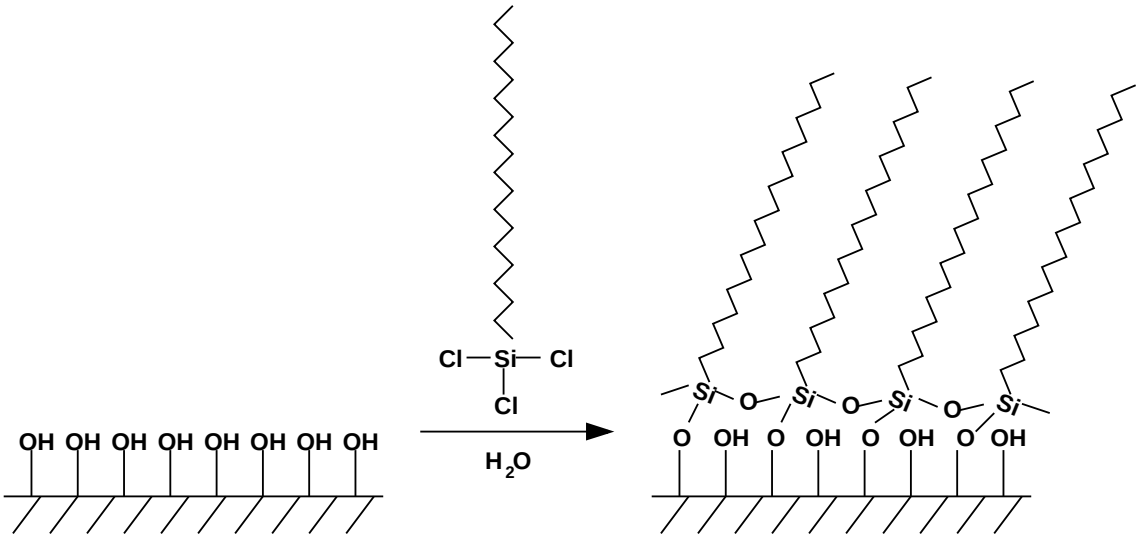

Figure 1.2: A depiction of a typical chlorosilane compound reacting with a target surface.

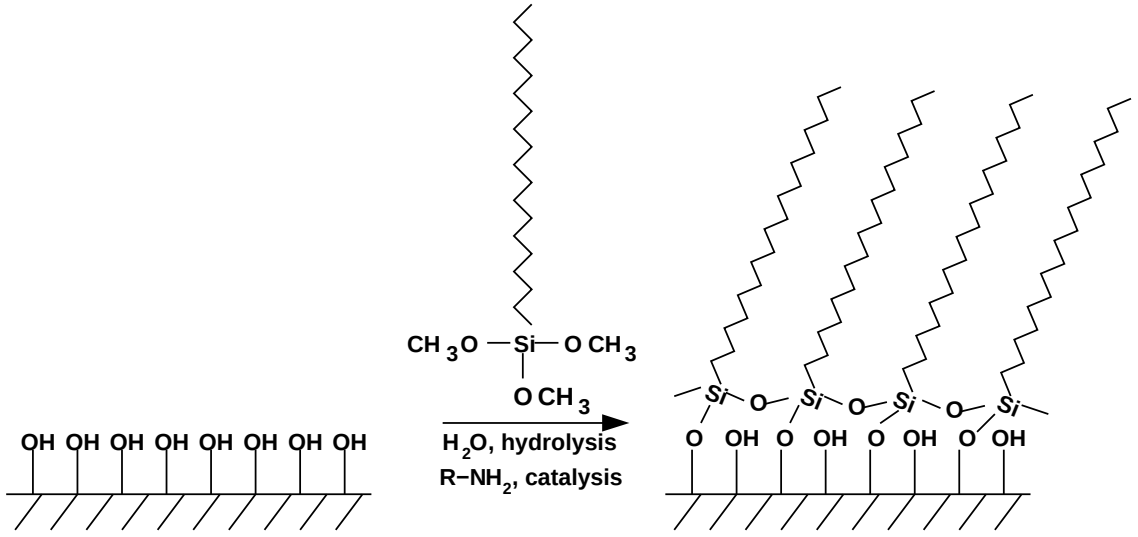

Figure 1.3: A depiction of a typical alkoxysilane compound (in this case, a methoxysilane) reacting with a target surface.

dimethylamino groups. These molecules are extremely reactive with water, so they must be kept rigorously anhydrous at all times. They react directly with -OH groups on the target surface, and eliminate dimethylamine, a volatile byproduct. Since the reaction requires no water, the surface itself is the second reactive constituent, and once all available reactive sites are consumed, the reaction is quenched. As a result, dimethylaminosilanes form high quality, conformal monolayers and result in no particulate formation. They have been utilized in vapor deposition strategies for surface modification of MEMS devices [2].

The common thread between all of the various organosilane surface modification chemistries is the requirement that the surface possess a sufficient concentration of reactive groups. If the surface is not reactive, or lacking -OH functionality, surface modification by organosilane chemistry cannot proceed.

1.2.1 The Potential Technological Impact of Organosilane-based Monolayers

Molecular layers formed from organosilane agents have broad applications in many different areas including their use as coupling agents in composites, glass fibers, and adhesive joints [8,11], immobilization of proteins, enzymes, antibodies, and DNA [8–11] and inorganic nanoparticles [10,12], chromatographic stationary phases [8,11,25], and in chemical sensors [26]. Since the synthesis chemistry of silicon is very similar to that of carbon [27], a wide variety of organosilicon compounds can be readily synthesized from well-understood organic synthesis procedures. As a result, an enormous variety of organosilicon compounds, with varying head groups and pendant groups, are already commercially available. This also opens the door for rational and intelligent design of organosilane compounds to meet specific application needs, offering the potential to engineer new materials at the molecular scale.

Their facile deposition to silicon and glass substrates makes this class of precursors ideally suited to applications involving MEMS, bio-MEMS, and microfluidics devices, which are frequently made from silicon and glass. For example, surface modification by organosilane precursors has been shown to alleviate non-specific protein adsorption on surfaces [13–16] and in micro-channels [17–20], to affect electroosmotic flow (EOF) [24], and to alleviate cell

adhesion in microchannels [19, 20]. In light of these considerations, surface modification by organosilane precursors is potentially an enabling technology for the commercialization of bio-MEMS and microfluidics devices.

1.2.2 Limitations of Organosilane-based Films

As the bio-MEMS and microfluidics industries continue to evolve, a recent shift from silicon and glass-based devices to polymeric devices has been observed. Initially, microfluidics devices were fabricated by leveraging the rich knowledge of silicon micromachining and bulk micromachining, but due to the high costs of silicon and glass, these devices were too expensive for commercial application. Polymeric materials, due to their lower cost, ease of device fabrication by various processes, varied and favorable material properties, and, in some cases, pre-existing regulatory agency approvals, have become the preferred materials in these industries [28]. Several polymers, including polydimethylsiloxane (PDMS), poly(ethylene terephthalate) (PET), poly(methyl methacrylate) (PMMA), and polystyrene, have emerged as potential candidates for biological and microfluidics applications. Chemical structures for these polymers are available in figure 1.4.

But the chemistry involved in tethering organosilane molecules to surfaces requires a favorable concentration of reactive surface groups (usually hydroxyl), thus preventing their application to many materials of technological relevance, such as many polymers and plastics. In fact, the surfaces of the polymers mentioned in the previous paragraph are fairly inert [18, 28–30], making surface modification difficult.

Polydimethylsiloxane (PDMS), for example, is now perhaps the most widely-researched material in microfluidics applications [28], due, in part, to a wide variety of favorable properties. Devices made from PDMS are easily fabricated in high-throughput processes, resulting in lower device costs. PDMS is optically transparent and rather biocompatible (in vitro) [29], making it ideally suited for biological assays, where facile monitoring during analysis is desirable [28]. It has high gas permeability, a useful property when considering the need to oxygenate cell cultures in closed systems [18]. It has a relatively high elasticity,

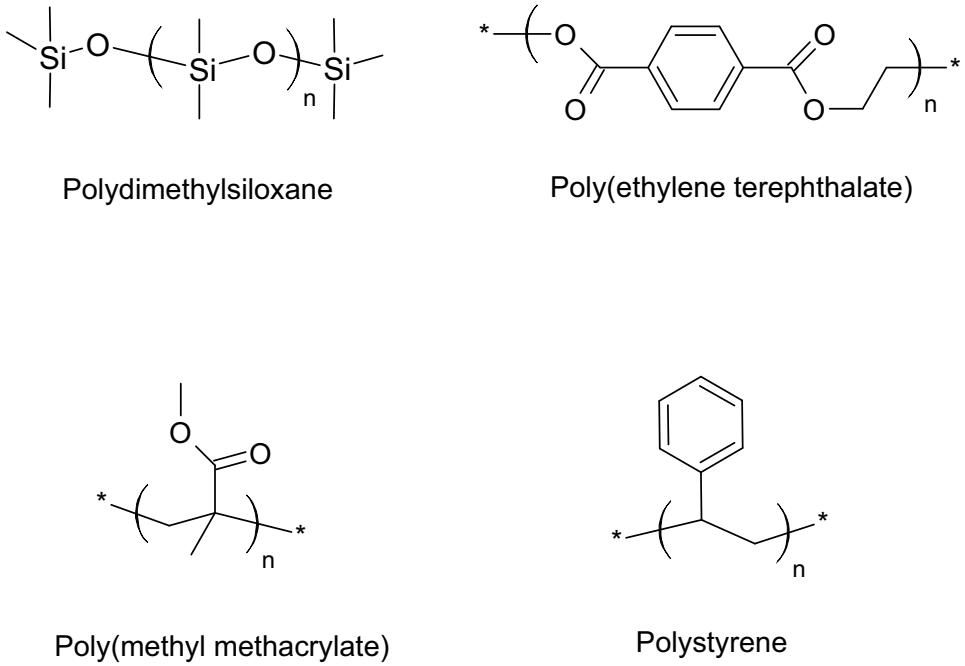

Polydimethylsiloxane

Poly(ethylene terephthalate)

Poly(methyl methacrylate)

Polystyrene

Figure 1.4: The chemical structures of some polymers commonly used in biological and microfluidics applications.

making it possible to fabricate valves in PDMS microfluidics devices, enabling the creation of very advanced devices [31, 32].

But PDMS does suffer from limitations. Its surface is hydrophobic, making it difficult to handle aqueous solutions, which is critical for biological applications [18]. Surface hydrophobicity has also been demonstrated as a problem for non-specific protein adsorption [33]. Since PDMS is ideally suited for bio-MEMS applications, the problem of non-specific protein adsorption has major implications for the future success of commercial devices fabricated from PDMS. These limitations could potentially be overcome by proven surface modification strategies, but surface modification of PDMS by existing methodologies if often difficult given that PDMS lacks sufficient reactive surface groups.

According to an excellent review article by Andrew deMello, the primary issue that will define the success or failure of polymer-based materials in microfluidics applications is the development of methodologies for achieving well-defined and stable surface chemistries [28]. Due to the large surface area to volume ratios commonly encountered in microfluidics devices, the ability to tune the surface chemistry is highly desirable, and therefore robust, stable, and versatile surface coatings are highly sought after [29]. Organosilane surface modification chemistry, with its wide availability of a variety of pendant group chemistries and established track record of success in various surface modification applications, could be leveraged in a powerful way to address this pressing technological need. However, many technologically important polymers, like PDMS, lack sufficient reactive surface groups, making surface modification strategies, especially those involving organosilane precursors, difficult. In fact, each organosilane compound discussed in section1.2 requires the presence of hydroxyl groups on the target surface in order for a covalent bond to form. One might imagine converting a polymer or plastic surface to a surface amenable to organosilane surface modification through the application of an intermediate layer that is rich in reactive hydroxyl groups. This would open the door for leveraging the proven success of organosilane precursors for surface modification of polymers and plastics, which could potentially lead to major breakthroughs in the fields of bio-MEMS and microfluidics. However, traditional

methods for depositing oxide layers such as silica require operating temperatures in excess of 300°C [34]. This high temperature requirement limits the application of such processes to thermally stable materials, and precludes their application to many polymers and plastics.

1.3 Silica Layer Processing—Bridging the Gap

The vapor-phase hydrolysis of silicon tetrachloride has been demonstrated to result in the deposition of silica layers at room temperature [35]. Previously, contact angle data has demonstrated that a similar "seed" layer can improve the thermal and aqueous immersion stability of molecular layers formed from heptadecafluoro-1,1,2,2-tetrahydrodecyltrichlorosilane (FOTS) on titanium nitride and aluminum substrates [36]. It is postulated that this seed layer provides an increased number of hydroxyl sites on the surface relative to surfaces without seed layer treatment, resulting in an increased density of available surface reaction sites. In fact, XPS data indicate that FOTS films deposited on seed layer surfaces exhibit approximately a 15% higher ratio of total fluorine to total silicon peaks as opposed to FOTS monolayers deposited on glass, indicating an increase in the density of the monolayer coating in terms of molecular coverage [36].

Much analytical work has been devoted to gaining a better understanding of conventional silica surfaces and the role of their surface chemistry in condensation reactions. However, there has been little if any work devoted to characterizing and understanding the silica surfaces formed from the vapor phase hydrolysis of tetrachlorosilane, a necessary undertaking if these films are to be leveraged in new applications.

Therefore this dissertation is focused on the fundamental groundwork that is necessary before silica layer processing can be leveraged in new areas of pressing technological importance. Of critical necessity is the characterization of the surface chemistry of the vapor-deposited silica layer and how it compares to the surface chemistry of traditional silica materials. It is also important to understand how the structure of the resulting films depends on processing parameters. Furthermore, if the silica layer is to be implemented in

biological and microfluidics applications, it is also necessary to determine how it behaves and performs in aqueous environments.

Chapter 2

Previous Work

2.1 Silica Layer Processing

In order to better appreciate the following body of work, a brief background on silica is presented. Obviously, the body of knowledge on silica and silica materials is extensive, and what follows is essential information for understanding the unique qualities of the silica layer currently under study.

The vapor phase deposition of "seed" layers to various materials is not a new approach. In fact, a similar seed layer, formed from an organo-chlorosilane, to the one studied in this work has been reported on in the literature [36–38]. In the previous work, it was demonstrated that layers formed from the organo-chlorosilane could be deposited onto various surfaces, including plastics, and that the layers did support the attachment of fluorinated chlorosilane precursors. It was also suggested that the presence of the seed layer had a positive effect on the stability of fluorinated monolayers on aluminum and titanium nitride surface, relative to monolayer stability on untreated surfaces [36, 37].

The vapor deposition of silica layers formed from a similar process to the one studied in this work has been known for quite some time. In fact, in an 1969 article by Bannikova *et al.* [35], a reference to another article suggests that the technique was first demonstrated in 1946 by Russian scientists. However, there have been no published systematic studies of the physical and chemical properties of such films, or on the characteristics of monolayers formed on them. It is unknown how the properties of these films depend on the deposition conditions employed, what their stability is in aqueous environments, whether or not they can be deposited onto plastic and polymer surfaces, and how they interact with biological

systems, all necessary pieces of information if they are to be leveraged in bio-MEMS and microfluidics applications.

2.2 Surface Modification of Inert Polymer Surfaces

Although many polymer surfaces are relatively inert, the need for controlling surface chemistry in microfluidics and bio-MEMS applications has necessitated the development of several surface modification protocols. For polyesters (PET, PMMA), aminolysis has been demonstrated for the introduction of amine groups on polymer surfaces [30], which can then be used for protein immobilization. However, the aminolysis reaction results in unacceptable degradation of PET surfaces, and although it has been shown that less degradation results when multifunctional amines are used, the degradation is not eliminated [30]. Polystyrene and polybutadiene surfaces have been modified by UV-assisted surface modification in the presence of trialkylsilanes. In this method, UV light is used to generate highly reactive alkylsilyl radical species, which react with olefins and aromatic rings with high rate constants [39]. However, the technique has not been demonstrated with a large variety of precursor species, but has only been demonstrated with alkylsilanes. Furthermore, the method has only been demonstrated to work on surfaces that contain double bonds or aromatic rings, which would preclude its application to other materials of interest, such as PDMS. This method is therefore of limited usefulness.

UV-induced surface graft polymerization is another technique that has been employed for the surface modification of inert polymeric materials. This method is powerful given that the grafted polymers can be precisely engineered in advance, and the surface structure of the grafted polymer can be controlled [40]. Most graft polymerization techniques are solvent-based, which is a potential drawback for microfluidics applications, but some vapor-phase techniques have also been developed [40].

Recently, a technique similar to the proposed work has been demonstrated by Hozumi *et al.* to result in the formation of a nanoscale thin silica film on polystyrene [41] and polyimide [42] surfaces. The three-step process involves activation of a polymer surface by exposing it

to vacuum ultraviolet (VUV) light, chemisorption of 1,3,5,7-tetramethylcyclotetrasiloxane, an organosilane precursor, from the vapor phase, followed by photooxidation of the chemisorbed precursor with VUV. This process results in a thin, uniform silica layer about 1 nm thick on the polymer surface. The authors have also demonstrated that the silica layer does support the formation of well-defined, amino-terminated self-assembled monolayers (from methoxysilane precursors) on polyimide substrates [42]. A potential drawback to this method, especially for processing on PDMS substrates, is discussed in section 2.2.1.

2.2.1 PDMS

Due to its wide variety of beneficial properties discussed it section 1.2.2, PDMS has become the most widely researched polymeric material for microfluidics applications. However, the biggest problems preventing commercialization of PDMS microfluidics devices (and, perhaps, all microfluidics devices) lie in the surface chemistry [18], which has also been discussed in section 1.2.2. As a result, a wide variety of approaches for controlling the surface chemistry of PDMS have been developed, and will be discussed here briefly.

The most commonly employed procedure for altering the surface chemistry of PDMS is modification by exposure to energy sources. For example, oxygen plasmas, ultraviolet light, and corona discharges have been used to create hydrophilic PDMS surfaces, which make it easier to work with aqueous solutions, create surfaces supportive of electroosmotic flow (EOF), and enable bonding of PDMS chips [18]. It has been shown that oxidation of PDMS surfaces by these energy sources converts the surface to an SiO_x silica-like layer, which is estimated to be 3-10 nm thick [43, 44]. The silica-like layer behaves similarly to other silica materials, and is therefore amenable to silanization by organosilicon compounds, as has been demonstrated [18, 45].

Besides exposure to energy sources, several other methods including exposure to surfactants and lipids [18, 46], polyelectrolyte multilayers [47, 48], and proteins [33] have been demonstrated. However, a common shortcoming of each of the previously discussed techniques is a lack of long-term coating stability. PDMS exhibits an interesting and challenging

property, which has been termed as hydrophobic recovery. In short, even after modifying PDMS surfaces by the previously discussed methods, the original, hydrophobic surface properties of PDMS are regained after several minutes to several hours [29]. It is generally agreed that the recovery of the original properties of PDMS is due to migration of free PDMS chains from the bulk phase to the surface [18]. In fact, it has been shown that after oxygen plasma treatment, cracks estimated at between 0.3-0.5 μm deep form in the PDMS surface, which is deep enough to penetrate through the silica like layer into the bulk phase [43, 49]. It is suspected that the presence of these cracks after exposure to energy sources may aid the process of hydrophobic recovery by providing a path for migration of free PDMS chains from the bulk phase to the surface.

Recently plasma polymerization has emerged as a promising technique for surface modification of PDMS. It is hypothesized that the formation of a continuous, covalently bonded polymer layer on the PDMS surface could act as a physical barrier inhibiting the migration of free PDMS chains from the bulk to the surface, thereby preventing hydrophobic recovery. Barbier *et al.* utilized a low-pressure plasma reactor to deposit films of polymerized acrylic acid 450 nm thick onto a PDMS microfluidic chip, and demonstrated a direct and double emulsion for the first time in a PDMS system. Furthermore, their experiments could run continuously for more than three weeks, indicating a significant inhibition of the hydrophobic recovery mechanism [29]. Chen *et al.* have also demonstrated plasma polymerized deposition of poly(p-xylylenes) of varying thicknesses (5–110 nm) into confined microgeometries [50]. Furthermore, the authors demonstrate the ability to bind different biomolecules to the films deposited into sealed microfluidics devices, enabling them to perform fluorimetric assays. No assessment of film stability was made by the authors. These methods are similar to the method of Hozumi and co-workers discussed in section 2.2, and one is left to wonder why Hozumi and co-workers have not reported on modification of PDMS surfaces by their technique. The author believes that perhaps it is because the oxide nanoskin described by Hozumi and co-workers, since it is only 1 nm thick, is not an effective barrier against hydrophobic recovery.

The ability to coat homogeneously highly complex substrates, such as confined microgeometries with high aspect ratios, is an advantage of vapor phase processes over liquid phase ones [50], since the vapor is able to more effectively permeate into microchannels than liquid solvents [45]. Vapor phase processes have other inherent benefits over liquid phase processes including the elimination of organic solvents, which mitigates the environmental impact and avoids the issue of solvent/polymer compatibility, greatly decreased sample handling, and the ease of more precisely controlling precursor stoichiometry [3].

It is believed that the vapor deposited silica layer proposed in this work can help to address the technologically pressing issues hindering commercialization of PDMS microfluidics devices. Firstly, it is a vapor phase process, which affords the previously discussed benefits. Secondly, the presence of a uniform, highly-crosslinked silica film may serve as an effective physical barrier against PDMS chain migration from the bulk phase to the surface, which would alleviate the problem of hydrophobic recovery. But a key potential benefit of this approach is the ability to immediately leverage the vast body of knowledge of organosilane surface modification strategies to controllably tune the surface chemistry of PDMS microfluidics devices.

Chapter 3

Objectives for this Work

The main objective of this work is to enable the application of silica layer processing in new and technologically important areas. Therefore, understanding the chemical and physical properties of the vapor deposited silica layer at a fundamental level is necessary. Several important questions must be answered, and they follow here.

- What is the proper technique for depositing a desirable silica layer, and how do the film properties depend on the deposition conditions employed?
- How do the chemical properties of the silica layer compare to conventionally prepared silica materials?
- Do organosilanes form molecular layers on the silica layer as well as they do on the native oxide on silicon surfaces?
- Does silica layer processing result in sufficient deposition on surfaces lacking reactive groups to enable organosilane surface modification on these surfaces?
- What is the stability of the silica layer in aqueous environments?
- What is the effect of the presence of the silica layer on biological samples, including proteins and cells?

Chapter 4

Design, Fabrication, and Operation of a Vapor Deposition System with *in situ* Infrared Interrogation Capabilities

4.1 The First Generation

The first vacuum deposition system is based on a previously described system [3]. Briefly, the vacuum deposition system consists of a rotary vane pump (base pressure 0.4 Pa) which is coupled to a glass reaction chamber that contains perforated electrodes which can be biased to create an *in situ*, capacitively-coupled, radio frequency (RF) plasma (13.56 MHz). The glass reaction chamber is also coupled to a vapor delivery system which allows for the introduction of the vapors of various volatile precursors into the glass reaction chamber. MKS Baratron capacitance manometers are used to monitor the system pressure up to 1.3×10^4 Pa. A simplified schematic and photograph of the vacuum deposition system can be seen in figure 4.1.

Two glass chambers were designed and constructed to be used with the first generation system, and they are pictured side by side in figure 4.2. The smaller chamber contains a grounded aluminum sample stage. The sample stage has a heater cartridge inserted into its center with a thermocouple mounted onto its surface, allowing for temperature control of $\pm1^\circ$C to in excess of 500°C. The smaller chamber is ideal for processing smaller samples, and can easily accommodate up to ten 8mm × 8mm silicon squares. The large chamber is not equipped with a heated sample stage, but it can accommodate many more samples, up to an entire six-inch silicon wafer. This makes it ideally suited for cleaning large quantities of samples simultaneously, or for performing vapor deposition on large, irregularly-shaped substrates.

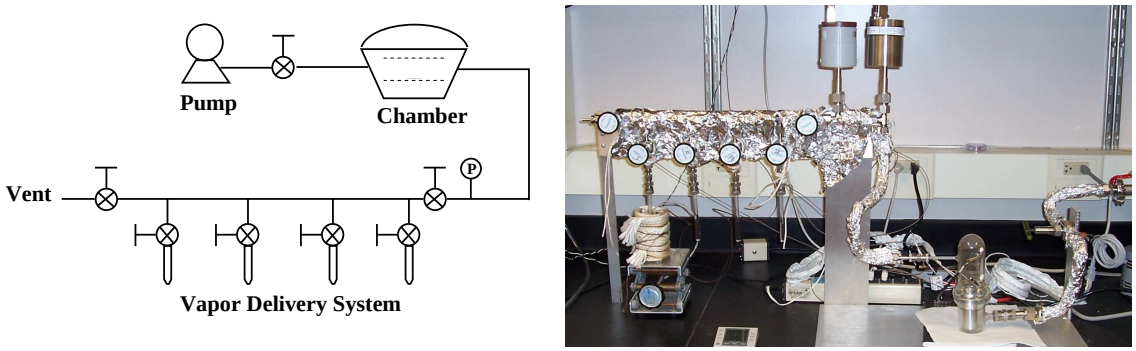

Figure 4.1: A schematic (left) and photograph (right) of the custom vacuum deposition system employed in this work.

Figure 4.2: The two custom-built glass chambers used with the first generation vapor deposition system are pictured side-by-side.

The first generation system is well-suited for oxygen plasma processing/cleaning of samples and other materials. It can also be used for relatively simple vapor deposition processes, but it is not without its limitations. When dosing two or more precursors for a vapor deposition recipe, there is no way to segregate the precursors once the first precursor has been dosed into the system. This is especially problematic if the precursors are very reactive. For instance, when depositing the silica layer, water and tetrachlorosilane are required. Controlled dosing of the first precursor is achieved easily, since it is dosed into the system when it is initially empty. But controlled dosing of the second precursor is not possible given that the reaction begins immediately when the two precursors begin to mix, and it is very rapid. As the reaction proceeds, the pressure changes, making it impossible to know exactly how much of the second precursor has been admitted to the system. As a result, controlled studies on the deposition of the silica layer, which are needed to meet the objectives of this work, cannot be performed.

4.2 The Second Generation

In order to address the previously-discussed drawback, the first generation vapor deposition system was modified with "expansion volumes." The expansion volumes are modified volumetric flasks that are attached to the vapor deposition in such a way as to allow for their complete segregation from each other and from the deposition chamber. A schematic and photograph of the second generation vacuum deposition system can be seen in figure 4.3. The second generation system allows for independent and controlled dosing of up to three separate precursors, one precursor in each of the two expansion volumes, and one precursor in the deposition chamber. The basic dosing strategy is as follows:

1. Evacuate the system
2. Isolate the chamber and expansion volume 2 from the vapor delivery system
3. Isolate the system from the pump
4. Fill expansion volume 1 to the desired pressure with the desired precursor

5. Isolate expansion volume 1, and evacuate the rest of the system

6. Repeat for the other expansion volume/chamber

4.3 Design of Chambers for *in situ* Infrared Spectroscopy

The first chamber is designed around the Perkin Elmer horizontal attenuated total reflection (HATR) accessory, which consists of a steel plate, with an attenuated total reflection (ATR) element sealed to it, that rests on top of an optical alignment box. The optical alignment box contains two planar mirrors and two focal mirrors which can be adjusted to focus the infrared beam on the incident face of the ATR element. At angles of incidence greater than the critical angle, total internal reflection is achieved. At the face of the crystal, an evanescent wave is established, which is attenuated by interaction with the sample material, resulting in the formation of the sample's infrared spectrum. A schematic reflecting the phenomenon of attenuated total reflection is shown in figure 4.4.

A custom aluminum plate was designed and fabricated and used in place of the steel plate that Perkin Elmer supplies with the HATR accessory. Briefly, the design of the plate was modified to include an o-ring groove on the underside so that an ATR element could be sealed to the bottom side and hold vacuum. A photograph of the bottom side of the aluminum plate is available in figure 4.5. A glass chamber with two ports for access to the source gases and to the pump was designed and constructed, and seals to the top of the aluminum plate with an o-ring. In both cases, viton o-rings are used, which are treated with Apiezon L grease.

Two aluminum blocks with embedded heater cartridges sit on top of the aluminum plate and surround the glass chamber, and a thermocouple is affixed to the surface of the aluminum plate for temperature feedback. In this manner, the temperature of the aluminum plate can be controlled from room temperature up to 200°C, which is the upper operating temperature for the viton o-rings. While the chemistry at the surface of the ATR element can be probed *in situ* with the infrared spectrometer, it is also important to note that this

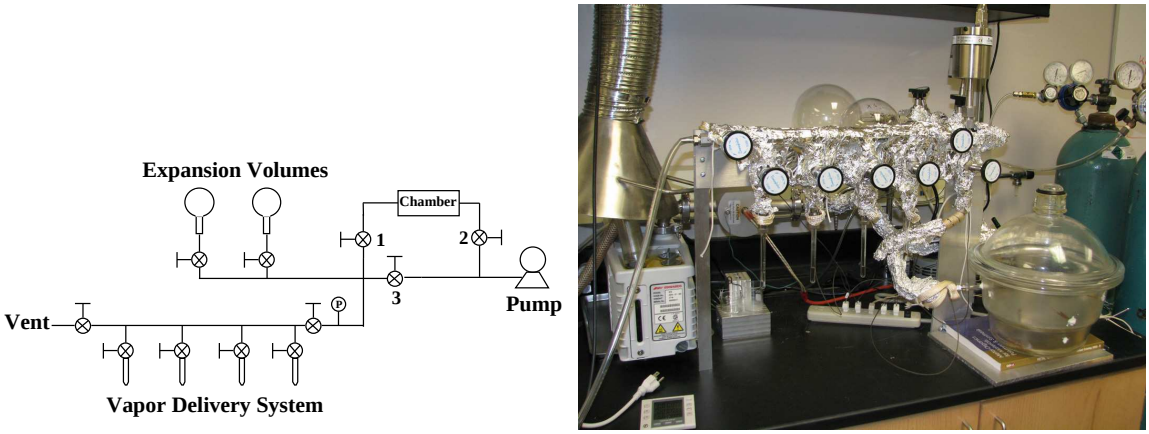

Figure 4.3: A schematic and photograph of the second generation vacuum deposition system.

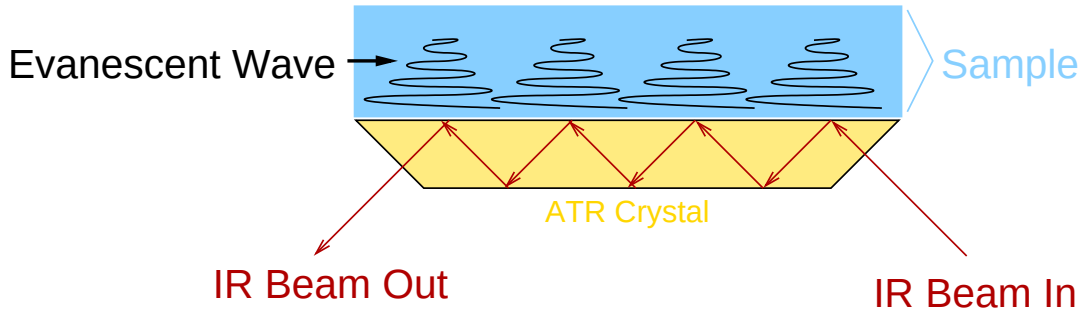

Figure 4.4: Schematic demonstrating the principle of the attenuated total reflection phenomenon (drawing not to scale).

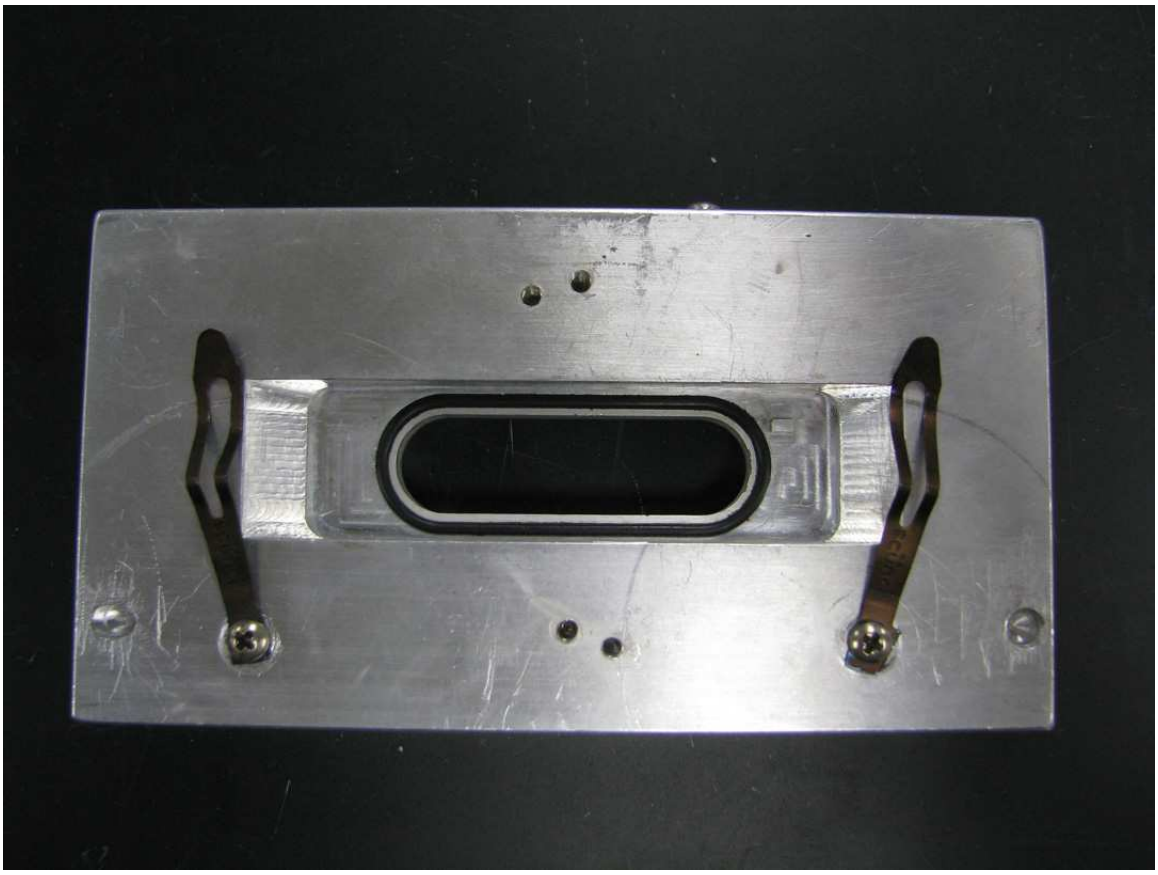

Figure 4.5: Photograph of the bottom side of the custom aluminum plate fabricated for the HATR accessory. The viton o-ring is clearly visible.

design enables the introduction of other samples into the chamber so other analyses can be conducted, *ex situ*. This allows for the potential collection of many different kinds of data, including infrared absorption characteristics, film thickness, surface topography, etc., all from a single experiment. A schematic and photograph of this chamber are available in figure 4.6.

The second chamber constructed is based on a previously reported high-temperature infrared cell, with some modifications [51]. It allows for the collection of gas-phase infrared spectra, and also for the collection of infrared spectra of surface-bound species, *in situ*. Briefly, two quartz o-ring joints were fused together to create a tube body, and then smaller tubes were sealed onto the body for access to the source gases and to the pump. The infrared windows are sealed to the joints with viton o-rings, and the windows are held in place until vacuum is applied with teflon caps and metal clamps. This design allows one to easily change between different infrared windows without damaging them (the previously reported design relied on an epoxy material to seal the infrared windows in place). Assembling the chamber as described allows for the collection of gas-phase infrared spectra.

For collecting infrared spectra of surface-bound species, an additional small infrared window is used to support a thin film of a material of interest. The small window is held upright by a slit cut into a quartz tube, and the quartz tube is then inserted into the large tube body. The section of the large tube body between the source gas and pump ports fits into a furnace, which allows for temperature control from room temperature to 1000°C. The entire apparatus fits inside the sample compartment of the FTIR spectrometer and is operated in transmission mode. As with the attenuated total reflection chamber, other samples can be placed inside this chamber, allowing for the collection of additional data, *ex situ*. A schematic and photograph of the transmission infrared chamber are shown in figure 4.7.

Finally, a second generation vapor deposition system was constructed around a Perkin Elmer Spectrum 2000 FTIR Spectrometer. This allows for the collection on infrared spectra *in situ*. Each of the two chambers discussed in section 4.3 fit directly into the instrument's

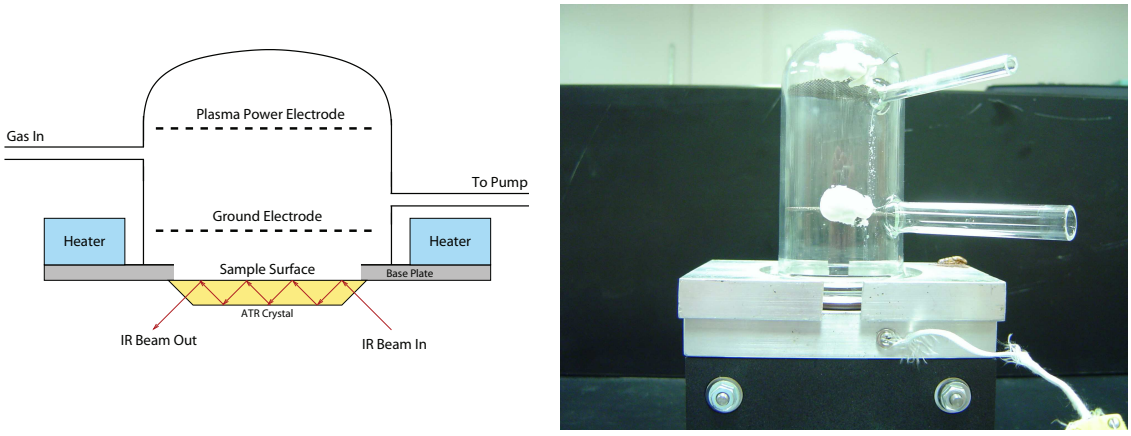

Figure 4.6: A schematic and a photograph of the attenuated total reflection infrared chamber.

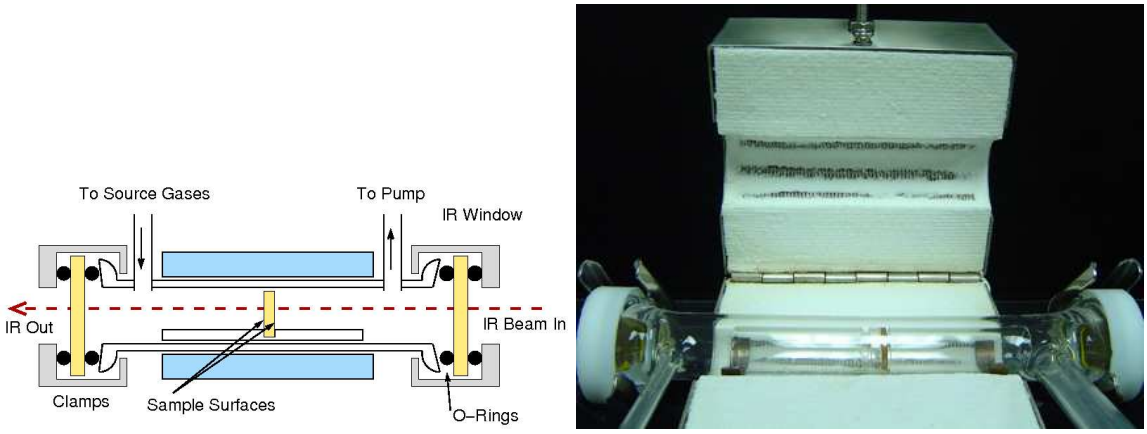

Figure 4.7: A schematic and a photograph of the transmission infrared chamber.

sample compartment, allowing for easy collection of infrared spectra, *in situ*, without the need for external optical components. A photograph of the system is available in figure 4.8.

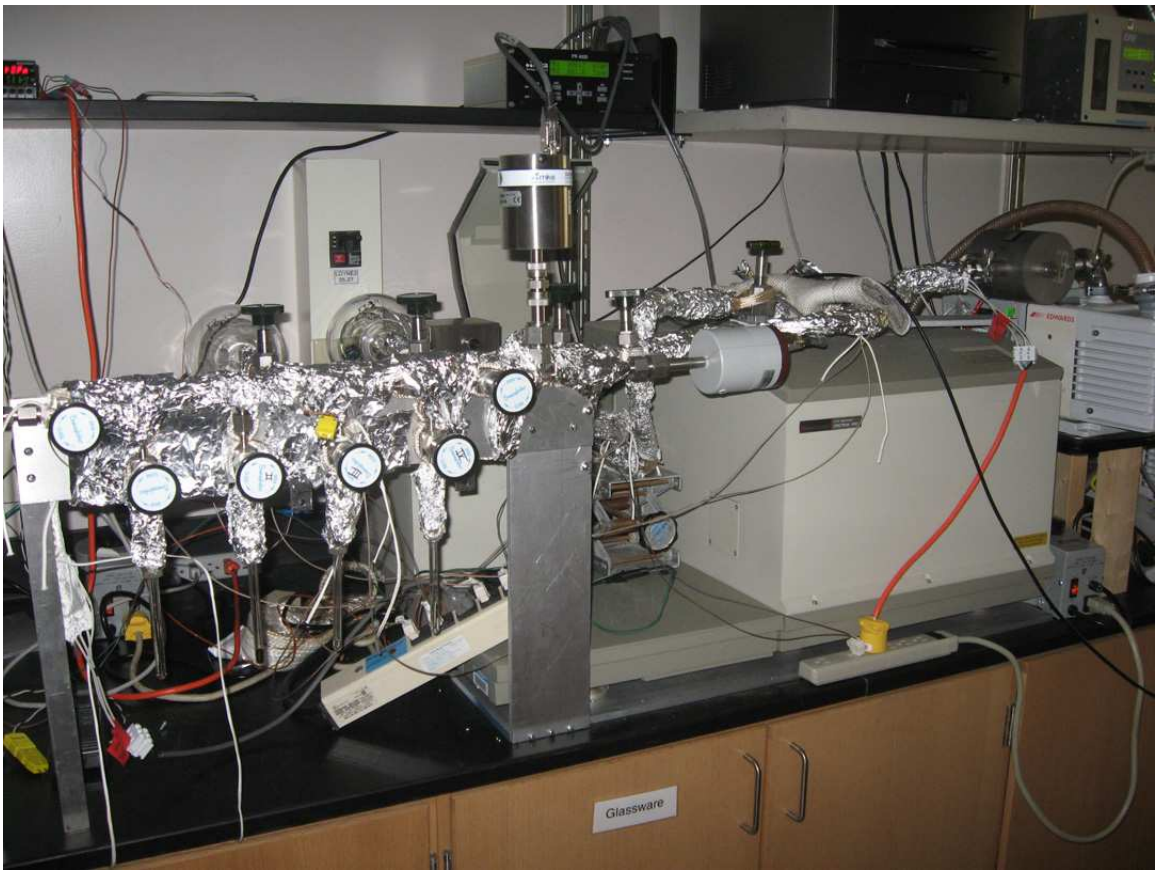

Figure 4.8: Photograph of the vapor deposition system with *in situ* infrared interrogation capabilities.

Chapter 5

Employing the Vapor-Deposited Silica Film as a Substrate for *in situ* Infrared Spectroscopic Studies

5.1 Background and Motivation

The use of infrared spectroscopy for studying physical and chemical interactions on silica surfaces is well-established, with literature dating back for decades. In the past, however, due to strong infrared absorption in the low-energy region of the spectrum, valuable information for surface interactions on most oxides (including silica) or zeolites below 1300–1000 cm^{-1} was unavailable [52]. The traditionally employed sample preparation technique in these early experiments was the self-supporting disk technique in which silica is mixed with an IR transparent material (i.e. KBr) and pressed into a disk. Typically, these disks contained $\sim$10 mg/cm^2 of silica material. With some care, the amount of silica utilized to form a self-supporting disk was reduced to $\sim$2 mg/cm^2, and although the transparency of the spectra obtained using such disks was improved, there were still regions in the spectrum that were completely opaque due to the strongly absorbing oxide [51]. It was not until the development of the thin film technique in 1984 by Morrow and coworkers [52] that information from this previously difficult to probe region of the spectrum could be gleaned. The thin film technique involves placing a very small amount of silica, typically $\sim$0.2 mg/cm^2, on the surface of an IR transparent window. This is accomplished by dispersing the silica in a volatile solvent, spraying the dispersion on the IR window, and allowing the solvent to evaporate, leaving behind a thin silica film. Since the thin film technique requires only a small amount of the strongly-absorbing oxide, transparency of the spectrum is drastically increased.

Tripp and Hair [51] employed the thin film technique to study the chemisorption of various chloromethylsilanes on the silica surface. Previously, the only spectral information available to researchers investigating these reactions were the surface silanol stretching modes and the C-H stretching modes from the surface-bound species. By implementing the thin film technique, Tripp and Hair were able to observe various absorption modes that were invaluable in helping them to determine the structure of the surface-adsorbed species, including the CH_3 symmetric deformation mode at 1260 cm^{-1}, the Si_s-O-Si mode which forms as a result of chemisorption at 1060 cm^{-1}, the CH_3 rocking modes at 840–780 cm^{-1}, and various Si-Cl absorption modes at 400–600 cm^{-1} [51].

Although the thin film technique offers the ability to probe previously unavailable regions of the infrared spectrum, which is a very important advancement, it is not without its shortcomings. Since it relies on the evaporation of a solvent from the surface of the IR window to leave behind a silica film, silica particles will concentrate in regions where the solvent evaporates from last, forming regions of larger silica agglomerates that are very loosely held to the surface of the IR window. As a result, extreme care must be taken in handling the window throughout the course of the experiment. Even evacuating an infrared cell too quickly in which a thin silica film is installed can cause portions of the film to become detached, leading to false negative absorbances in resulting spectra. Such an occurrence can make it difficult or even impossible to draw meaningful conclusions from the experimental data. The spectrum depicted in figure 5.1 shows evidence of this phenomena. This particular spectrum was the final spectrum collected in a series of experiments that had been conducted throughout the course of a day. The vital information being sought was the presence/absence of a peak at $\sim$1130 cm^{-1}, but due to the loss of some of the silica film, this information could not be determined conclusively from the spectrum.

Previous studies have shown that the vapor phase hydrolysis of tetrachlorosilane results in the deposition of a thin, uniform silica film [35, 53, 54] with chemical properties different from those of conventionally prepared (i.e. fumed or precipitated) silica materials [54]. Furthermore, these films can be deposited onto polymers such as poly (methyl methacrylate)

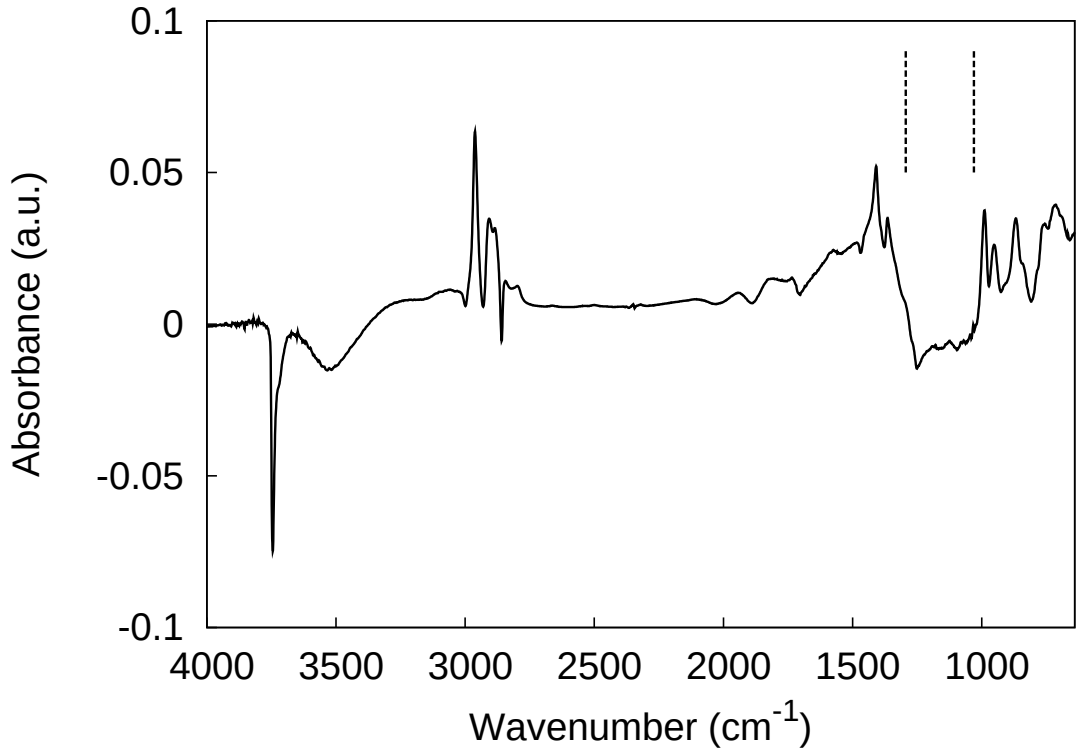

Figure 5.1: Difference spectrum (relative to a fumed silica thin film) of a chemisorbed precursor on a vapor deposited silica film. The strange shape of the spectrum in the region from 1250–1040 cm^{-1} is the result of a small fraction of the silica thin film falling off of the IR window during the experiment.

(PMMA) and polystyrene, offering the potential to expand the types of chemistry that can be performed on these surfaces [54]. For example, the deposition of a silica layer onto PMMA and polystyrene surfaces may enable the application of organosilane surface modification chemistry to these surfaces, which is usually not possible. Therefore, new experimental methods must be developed in order to fully investigate these types of silica materials so that their potential technological benefit can be realized. This paper reports on the novel application of a vapor deposited thin silica film for *in situ* $\tilde{\text{F}}$TIR surface studies on silica. Infrared spectra of the vapor deposited silica film are compared with spectra collected for conventional silica materials. Finally, the thin silica film is employed as a substrate for *in situ* infrared spectroscopy, and results are compared with previously reported data.

5.2 Silica Deposition

A previously described [3, 53] vapor deposition system was modified to include expansion volumes, which allow for the independent dosing of reactive precursor gases without exposing the reaction chamber to either gas until the experiment is ready to be started. Furthermore, this vapor deposition system was constructed around the FTIR instrument to enable the collection of *in situ* infrared spectra. A schematic of this system is available in figure 4.3.

Deionized water and tetrachlorosilane are loaded into clean glass vials, and then connected to the vapor delivery system. The precursors are degassed by employing multiple freeze-pump-thaw cycles with liquid nitrogen. The system is evacuated to base pressure, and then the chamber is isolated from the pump by closing valves 1 and 2. For dosing precursor gases, the remainder of the system is isolated from the pump by closing valve 3, and water vapor is allowed to fill the first expansion volume by opening the appropriate precursor and expansion volume valves. When the pressure has stabilized at the desired value, the precursor and expansion volume valves are closed, and the remainder of system is evacuated by opening valve 3. This process is repeated to fill the second expansion volume with tetrachlorosilane, and the system is then again evacuated to base pressure. Dosing in

this manner ensures that precursor gases remain completely segregated until the experiment is ready to begin, which is a necessity when dealing with reactive gases.

To begin the deposition, valves 2 and 3 are closed, and valve 1 is opened. This configuration effectively isolates the entire system from the pump, while allowing the admittance of precursor gases into the reaction chamber. Water and tetrachlorosilane vapors are admitted to the reaction chamber by opening both expansion volume valves, and they are allowed to react for ten minutes in a batch fashion. The system is then evacuated for five minutes by opening valves 2 and 3, and then the infrared spectrum is collected.

5.3 Results and Discussion

Characteristics of the vapor deposited silica films (thickness, RMS roughness, film morphology) are highly dependent on the pressures of tetrachlorosilane and water chosen for the deposition. For example, a deposition employing 20 Torr of water vapor and 13 Torr of tetrachlorosilane vapor produces a silica layer that is 17.5 nm thick with an RMS roughness of 6.9 nm, while a deposition employing 5 Torr of water vapor and 15 Torr of tetrachlorosilane vapor produces a silica layer that is 22.5 nm thick with an RMS roughness of 0.7 nm. A detailed investigation of the dependence of these properties on the precursor pressures has been conducted, and details are available elsewhere [54]. It is important to consult reference [54] when replicating this technique.

Infrared spectra of a conventional silica thin film and a vapor deposited silica film compare favorably and are available in figure 5.2. Major peaks present in the vapor deposited silica film include a broad feature centered at 3400 cm^{-1}, a strong, sharp peak at 1070 cm^{-1}, with a shoulder at 1220 cm^{-1}, and small peaks at 920 cm^{-1} and 810 cm^{-1}. Assignment of the various peaks has been reviewed elsewhere [51,55]. The broad feature at 3400 cm^{-1} has been assigned to O-H stretching vibrations of hydrogen bonded surface silanols, and the peaks at 1070 cm^{-1} and 810 cm^{-1} are due to various Si-O-Si network modes. The shoulder present at 1220 cm^{-1} is also common to amorphous silica materials [56]. The peak at 920 cm^{-1} has been assigned to an Si-OH bending mode or to an Si-O stretching mode in a

silanol group [54]. For the vapor deposited silica films, it is important to note the absence of a peak at 3747 cm^{-1}, which is present in the infrared spectra of the conventional silica film. It is attributed to the O-H stretching frequency of a freely vibrating, terminal surface silanol.

Not only do the spectra of vapor deposited silica films compare favorably with the spectra obtained by the conventional thin film method, but since the films formed by the vapor technique are highly uniform (lack of large agglomerates), the problem of portions of the film becoming detached during the experiment is eliminated.

5.3.1 Vapor deposited silica film as a substrate for infrared surface studies

The ATR chamber described in section 4.3 is fitted to the deposition system. The entire system is evacuated to base pressure, and a background spectrum is collected. A thin silica film is deposited from 20 Torr of water vapor and 20 Torr of tetrachlorosilane. These precursor pressures are chosen in order to produce a film with high surface coverage and high RMS roughness [54]. In order to remove physisorbed water vapor from the resulting film, the system is evacuated at room temperature until base pressure is recovered, which usually takes several hours. Then a spectrum is collected. Next the chamber is exposed to the vapors of a precursor of interest for 10 minutes, evacuated to base pressure, and a spectrum is collected. The difference spectrum between the two spectra collected before and after addition of the precursor represents the infrared spectrum of the adsorbed species. A spectrum obtained for DDMS by this method is available in figure 5.3. The spectrum is very similar to results obtained by Tripp and Hair [51], and the major peaks present, and their assignments, are as follows: 2970 and 2921 cm^{-1} (non-symmetric and symmetric CH_3 stretching, respectively), 1260 cm^{-1} (CH_3 symmetric deformation from $SiCH_3$), 1060 cm^{-1} (broad; various Si-O-Si linkages), 865 and 810 cm^{-1} (CH_3 symmetric and non-symmetric rocking modes). One major difference between the spectrum in figure 5.3 and the previous work reported by Tripp and Hair is the absence of a clear negative absorption peak in the high energy region of the spectrum, indicating which surface species have reacted with the

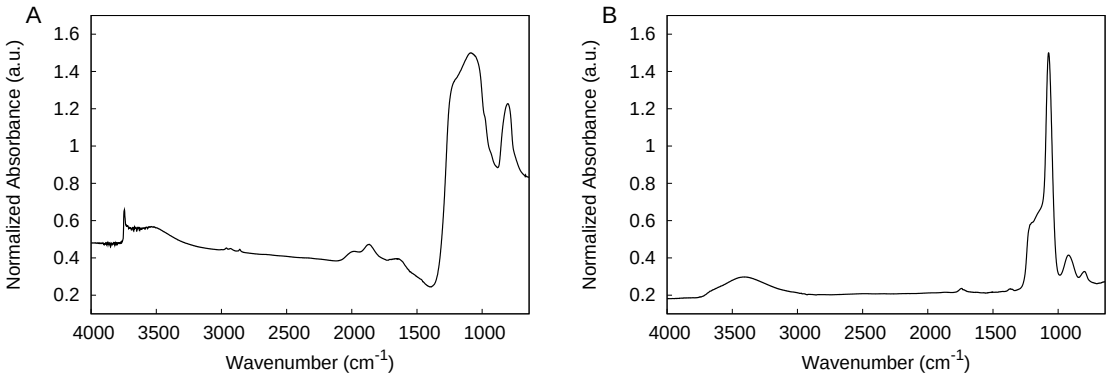

Figure 5.2: FTIR absorbance spectra of A) a conventional silica film prepared by the thin film technique, and B) a vapor deposited thin silica film. Note the narrow width of the peak centered at $\sim$1050 cm^{-1} compared to the broad width of the silica film prepared by the traditional thin film technique (spectrum A).

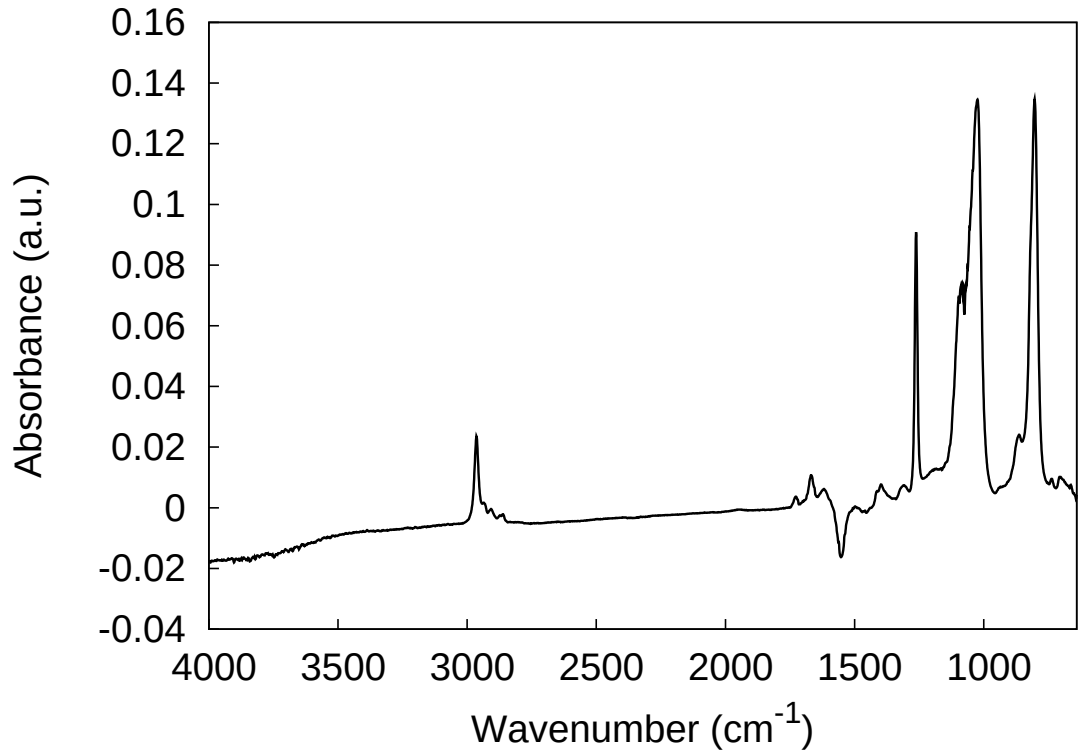

Figure 5.3: *In situ* ATR-FTIR difference spectrum of DDMS on a vapor-deposited silica film.

DDMS vapors to form the surface bound species. Tripp and Hair report that DDMS reacts with surface silanols, as indicated by a clear negative adsorption peak at 3747 cm^{-1}, but the spectrum in figure 5.3 displays no similar feature.

Sample preparation techniques reported by Tripp and Hair include heating the silica surfaces to 450°C *in situ*. Such a treatment results in a surface consisting mostly of a single type of silanol group, as evidenced by a strong sharp peak at 3747 cm^{-1}. Thus, during a chemisorption event at a surface like that prepared by Tripp and Hair, a precursor molecule is presented with essentially one type of surface group to react with, making a surface reaction easy to detect. On the other hand, exposing the vapor deposited silica films to elevated temperatures does not produce a single type of surface silanol group, but results in the elimination of surface silanol groups through the formation of siloxane bonds [54], making pretreatment in this manner unfavorable. As evidenced by the broad peak in the high energy region of the spectrum, the vapor deposited silica films possess many different types of silanol groups that may potentially react with a precursor molecule. Thus, changes occurring in this region of the spectrum during a chemisorption event may be very difficult to detect. Although there is some negative absorption in the high energy region in figure 5.3 which could be attributed to reaction, the resolution is not sufficient to conclude this.

Another difference between the spectrum in figure 5.3 and the previous work is the presence of a negative peak at 1550 cm^{-1}. The assignment of this peak is unclear at this time, but it is believed that the peak may be due to changes in Si-O overtone and combination modes of the silica film, caused by the deposition of the DDMS layer. Amorphous silica materials are known to display Si-O overtone and combination modes in the region of the spectrum from 2000–1300 cm^{-1} [51]. Absorptions near 1550 cm^{-1} can also be caused, primarily, by N-H stretching vibrations from various amine compounds [57], and also by carboxylic acids and pyrimidines. However, there are no such compounds present in these experiments, and given the relatively large magnitude of the peak at 1550 cm^{-1}, which is almost the same magnitude of the C-H stretching peak at 2960 cm^{-1}, it is believed that its

presence is a consequence of the presence of the DDMS layer on the silica film, and not due to trace contamination.

5.4 Conclusions

A vapor deposited thin silica film is investigated as a novel substrate for *in situ* surface studies on silica using infrared spectroscopy. Infrared spectra of silica films prepared by this method compare favorably with spectra collected by the conventional thin film technique. Furthermore, the uniformity of the thin vapor deposited silica film on the supporting infrared window reduces the likelihood of portions of the film falling off during an experiment, an improvement over the traditional thin film method.

Spectra of DDMS chemisorbed on the silica layer obtained by this method compare favorably with published literature data, except for the absence of a clear negative absorption peak, indicating which surface species have participated in the chemisorption reaction. The absence of this peak is not surprising, however, given the different surface pre-treatment conditions and the previously demonstrated differences in surface chemistry between the vapor deposited silica films and conventionally prepared silica materials. In cases where it is desirable to know information about the surface bound species and not necessarily know how they react with a surface, this method is more than sufficient. This method also has merit given that it is the only experimental technique put forth so far that can be used to study the vapor deposited silica films as they exist on surfaces, and it can also be used to investigate reactions on the newly formed, pristine silica layers, *in situ*. This is important because previous studies have demonstrated that these films can be successfully deposited on various surfaces, which could potentially enable the application of organosilane-based surface modification chemistries to non-conventional surfaces.

Chapter 6

Formation of Alkyl-organosilane SAMs on the Silica Layer: A Comparison to Monolayers formed on Native Silicon Oxide

6.1 Introduction

Due to their small size and small requirement for sample and reagent volumes, bio-microelectromechanical systems (bio-MEMS) and microfluidic devices are being increasingly researched for assays, characterization, and sensing of biomolecules and organisms [20]. Presently, devices capable of recording from, sensing, stimulating, and delivering to biological systems are being developed [21]. Although technology in this area is developing rapidly at the laboratory scale, commercialization of these technologies has been hindered by the inability of such devices to interact with biological systems in a non-immunogenic and stable manner [21]. Non-specific protein adsorption and cell adhesion, two processes that contribute to the phenomena known as biofouling, have proven especially problematic [22, 23]. As a result, much research has been aimed at improving the biocompatibility of such devices, and surface modification with molecular films formed from organosilane precursors has emerged as a promising approach.

Molecular layers formed from organosilane agents have broad applications in a wide variety of areas [8–12, 25, 26], and their facile deposition to silicon and glass substrates makes this class of precursors ideally suited to applications involving bio-MEMS and microfluidic devices, which are frequently made from silicon and glass. Surface modification by organosilane precursors has been shown to alleviate non-specific protein adsorption on surfaces [13–16] and in micro-channels [17–20], to affect electroosmotic flow [24], and to alleviate cell adhesion in microchannels [19, 20]. In light of these considerations, surface

modification by organosilane precursors is potentially an enabling technology for the commercialization of bio-MEMS and microfluidic devices.

However, a plaguing problem of molecular films produced from organosilane precursors is poor stability. Several studies have been conducted to determine the stability of various organosilane monolayers deposited on silicon oxide surfaces, and their results are briefly summarized here. While these films are stable in dry environments for long periods of time [15,21], their stability is severely compromised in aqueous conditions. Vandenberg and coworkers reported that incompletely cured films formed from 3-aminopropyltriethoxysilane were almost completely removed if submerged in water for 24 hours [8]. Furthermore, Haller showed that substantial attack on films formed from 3-aminopropyltrimethoxysilane occurred if they were submerged for longer than just a few minutes in water, and it was also determined that the film loss was hydrolitic in nature [11]. The thickness of films formed from vinyltrichlorosilane is reduced by almost 38% in physiological conditions [21], and the poor immersion stability of alkylsilane monolayers on titanium dioxide and zirconim dioxide has also been reported [58]. Polyethylene glycol [15, 16] and polyethylene oxide [14,19,59], which are materials well-known to reduce non-specific protein adsorption, have been deposited via organosilane chemistry and have been proven to inhibit non-specific protein adsorption. However, it has also been reported that the stability of these films is compromised in aqueous environments [15].

Although films based on organosilane chemistry present many advantages in terms of their well-understood deposition chemistries, their facile deposition to silicon and glass substrates, and their ready availability with a wide variety of pendant group chemistries, their relatively poor aqueous stability is a notable drawback. Since bio-MEMS and microfluidic devices inherently involve aqueous systems, in order for surface modification by organosilane precursors to be a viable technique to enable their commercialization, more work must be done to address and improve the aqueous stability of these molecular films.

Previously, contact angle data has demonstrated that a specially prepared silica seed layer can improve the thermal and aqueous immersion stability of molecular layers formed

from heptadecafluoro-1,1,2,2-tetrahydrodecyltrichlorosilane (FOTS) on titanium nitride and aluminum substrates [36]. It is postulated that the seed layer provides an increased number of hydroxyl sites on the surface relative to surfaces without seed layer treatment, resulting in an increased density of available surface reaction sites. In fact, XPS data indicate that FOTS films deposited on seed layer surfaces exhibit approximately a 15% higher ratio of total fluorine to total silicon peaks as opposed to FOTS monolayers deposited on glass, indicating an increase in the density of the monolayer coating in terms of molecular coverage [36]. These data suggest that films deposited on the silica seed layer have the opportunity to form a greater number of surface bonds than those deposited on untreated surfaces, which results in a more stable monolayer.

Organosilane surface modification chemistry relies on the presence of reactive surface hydroxyl groups which condense with hydroxyl groups on the precursor molecules, forming a covalently attached molecular film. Since the seed layer is believed to produce a surface which is rich in reactive hydroxyl groups, it is not surprising that its presence improves the stability of organosilane molecular layers on surfaces that are usually not amenable to organosilane chemistry (surfaces with few hydroxyl groups), as has been shown in the previous work [36]. The present work seeks to address the ability of the same seed layer to improve the thermal and aqueous immersion stability of various alkylsilanes on the silicon oxide surface, which is well known to be decorated with reactive surface hydroxyl groups and is therefore amenable, in its natural state, to organosilane surface modification chemistry.

In this work, trifunctional chloro- and methoxy- alkyl silanes with varying alkyl chain lengths are deposited onto normal silicon oxide surfaces and onto silicon oxide surfaces that had been treated with the seed layer material. Ellipsometry, contact angle analysis, and atomic force microscopy (AFM) are used to analyze the coated surfaces both before and after thermal exposure and aqueous immersion. Furthermore, those films formed from alkylmethoxysilanes are subjected to two different post-deposition curing methods to determine if either method offers any advantages over the other.

6.2 Experimental

6.2.1 Materials

Silicon wafers, p-type, with (100) orientation were obtained from University Wafer (Boston, MA). Octadecyltrichlorosilane, octyltrichlorosilane, octadecyltrimethoxysilane, octyltrimethoxysilane, and tetrachlorosilane were obtained from Gelest, Inc. (Morrisville, PA). Concentrated hydrofluoric acid (HF, 49%), acetone, isopropanol, and Optima grade hexanes (0.01% water) were obtained from Fisher Scientific (Fair Lawn, NJ). Propylamine (98%) was obtained from Acros Organics (NJ, USA). Deionized water (18 MΩ-cm) was obtained from a Millipore filtration system.

The naming convention adopted for the organosilane precursors utilized in this study is as follows: the pendant group is specified first by indicating the number of carbons, and the head group is indicated second by indicating its chemistry, either TCS for trichlorosilane, or TMS for trimethoxysilane. Thus, C18-TMS represents octadecyltrimethoxysilane. Throughout this paper, the experimental precursors will be referred to by this naming convention.

6.2.2 Wafer preparation and cleaning

Silicon samples are prepared by cutting the silicon wafers into 8mm × 8mm squares with a dicing saw. The silicon samples are sonicated in acetone for ten minutes and then again in isopropanol for ten minutes and then dried under a stream of nitrogen. Samples are etched for ten minutes in concentrated HF to remove the native oxide layer, rinsed in copious amounts of deionized water, and then dried under a stream of nitrogen. Samples are then loaded into a custom-built vacuum deposition system, which is described in section 4.1. After introducing the samples into the vacuum system, the system is evacuated to a pressure of less than 2.6 Pa. Oxygen gas is then allowed to flow through the system, and an oxygen background is established by multiple pump-purge cycles with oxygen gas. Then, the oxygen pressure is allowed to stabilize around 33.3 Pa, at which point the chamber is

isolated from the pump. An RF plasma is struck at 15 W forward power, and the samples are exposed to the plasma for five minutes. This treatment grows an oxide layer about 2 nm thick on the silicon surface. The samples are removed from the vacuum deposition system and etched again for ten minutes in concentrated HF, rinsed in copious amounts of deionized water, and dried under a stream of nitrogen. An additional oxygen plasma treatment is employed to re-grow an oxide layer. Treating the samples by this method "peels off" the uppermost layers of the crystal surface, revealing a clean, flat surface. This iterative cleaning method is repeated until inspection by contact angle and AFM indicate that a clean (contact angle $< 5°$), flat (RMS roughness $\sim$0.2 nm) surface has been obtained, but usually two iterations suffice.

6.2.3 Silica layer deposition

Deionized water and tetrachlorosilane are loaded into clean glass vials, and then connected to the vapor delivery system. The precursors are degassed by employing multiple freeze-pump-thaw cycles with liquid nitrogen. For vapor coating, freshly cleaned silicon samples are loaded into the vacuum deposition system. The system is evacuated until the pressure is less than 2.6 Pa, and then the samples are treated with an oxygen plasma by the method described in section 6.2.2 for substrate surface conditioning [36]. After the plasma pre-treatment, the chamber is again evacuated to a pressure less than 2.6 Pa, and then water vapor is admitted into the chamber, which is then isolated from the pump. Once the water vapor pressure is stabilized around 600 Pa, 267 Pa of tetrachlorosilane is admitted into the chamber, and the reaction is allowed to proceed for ten minutes. Since the reaction between these two precursors is rapid, it is important that the tetrachlorosilane is dosed quickly in order to minimize dosing errors. Therefore, in this study, the tetrachlorosilane dose time is thirty seconds or less.

6.2.4 Precursor deposition

Prior to coating, freshly cleaned silicon samples are treated with an oxygen plasma by the method described in section 6.2.2. Samples coated with silica seed layer are used immediately after their preparation. The samples are coated with the various organosilane precursors by the methods described below. In order to minimize experimental variables, clean silicon samples and seed layer samples are coated simultaneously from a single coating solution. It is also important to note that all glassware used is pre-coated with the appropriate precursor to eliminate competitive adsorption with the walls of the glassware.

For chlorosilanes, one drop of the precursor is added to 40 mL of Optima grade hexanes in a glass beaker and mixed gently by pipetting the solution in and out of a pasteur pipette. Freshly cleaned silicon samples and freshly prepared seed layer samples are then placed into the beaker, and the beaker is covered tightly with parafilm. The coating process is allowed to proceed until the contact angle indicates that a monolayer has formed, which is usually ∼100 minutes. Then the samples are removed, rinsed in two stages of neat hexanes, and then sonicated in hexanes for two minutes to remove any physisorbed precursor. The samples are then dried under a stream of nitrogen.

For methoxysilanes, a method reported by Follstaedt *et al.* is employed with slight modification [14]. Briefly, 0.85 mL of the precursor is added to 40 mL of Optima grade hexanes in a glass beaker and mixed gently by pipetting the solution in and out of a pasteur pipette. Then, 0.1 mL of propylamine is added as a catalyst, and the solution is gently mixed again. Freshly cleaned silicon samples and freshly prepared seed layer samples are then placed into the beaker, and the beaker is covered tightly with parafilm. The coating process is allowed to proceed for four hours. The samples are removed, rinsed in two stages of neat hexanes, and then sonicated in hexanes for two minutes to remove any physisorbed precursor. The samples are then dried under a stream of nitrogen. Annealing of these films is completed by one of two methods. In the first method, henceforth referred to as thermal annealing, the samples are placed on a temperature controlled aluminum block at 115°C for twenty minutes. The aluminum block has a hole drilled in it in which a

cartridge heater has been inserted. A thermocouple is mounted on the surface of the block for temperature feedback, and the temperature is controlled to within $\pm 1^{\circ}$C. In the second method, henceforth referred to as chamber annealing, the samples are placed into a glass chamber which is evacuated to a pressure less than 2.6 Pa. Then water vapor is admitted into the chamber until a pressure corresponding to $\sim$50% relative humidity is obtained. Samples remain in the chamber for 24 hours.

6.2.5 Surface analysis and characterization

Atomic Force Microscopy

Atomic force microscope (AFM) images are collected in air (21°C, $\sim$40% relative humidity) on a commercial AFM (Pacific Nanotechnology Nano-R AFM, Pacific Nanotechnology, Santa Clara, CA) in non-contact mode using silicon AFM tips with resonant frequencies in the range of 150-210 kHz and force constants in the range of 4.5-14 N/m (MikroMasch, Wilsonville, OR). Images are collected at a scan rate of 0.5 Hz.

Ellipsometry

Ellipsometric measurements are conducted on a nulling type ellipsometer (Rudolph AutoEL III, Rudolph Research, Fairfield NJ) equipped with a He–Ne laser ($\lambda = 632.8$ nm) at a 70° angle of incidence relative to the surface normal. Herein, reported values for film thicknesses are the averages from a set of sixteen measurements, four different positions measured on four different samples.

For films near the cycle thickness for the particular substrate-film combination under investigation (extremely thin films fall into this category), simultaneous determination of both the film thickness and refractive index is difficult, given that the measured parameters, the angles Δ and Ψ, are very insensitive to changes in refractive index in these regimes. For this reason, an accepted value for the refractive index of silicon oxide, $n = 1.46$, is used in this investigation for measurements of silicon dioxide produced from oxygen plasma and seed layer treatment. The refractive index of the silicon surface is set at $n = 3.858 + 0.018i$.

For ellipsometric measurement of the organic films on silicon oxide, a single film model with a refractive index of $n = 1.45$ has been proposed [60] and is used in this work. Briefly, the thickness of the initial oxide layer is measured using a refractive index of $n = 1.46$. After the organic film is deposited, the total thickness is measured using a refractive index of $n = 1.45$. The thickness of the organic layer is the difference between these two measurements.

Because the initial silicon oxide film thickness is determined at a refractive index of $n = 1.46$ and the composite organic on silicon oxide film thickness is determined at a refractive index of $n = 1.45$, it is necessary to ensure that the difference in refractive index between these measurements does not cause a significant difference in the reported thickness of the initial silicon oxide layer. A silicon oxide sample is measured by specifying the refractive index as $n = 1.46$, and the angles Δ and Ψ and the calculated thickness are recorded. Then the same values for Δ and Ψ are used to determine thickness based on a refractive index of $n = 1.45$. The discrepancy between the two calculated thicknesses is only 0.2 Å, which is an order of magnitude less than the instrument error (± 2 Å). Therefore, valid conclusions about the organic layer thickness can be drawn from comparing these data, and in this paper, the values reported for the thickness of the organosilane layers are the difference between these two measurements.

Contact Angle Analysis

Water contact angle measurements are obtained by the sessile drop method on a Ramé-Hart model 200 automated goniometer (Ramé-Hart, Inc. Mountain Lakes, NJ) using DROPimage Standard software. Herein, reported values are the averages for four measurements, one measurement made on four different samples. Measurement error for this technique is $\pm 2°$.

6.2.6 Thermal and aqueous immersion stability assessment

Thermal stability is assessed by exposing a coated sample to a specified temperature for five minutes in room air. A separate sample is used for each temperature. For this purpose,

the aluminum heating block described in section 6.2.4 is used. After heating, samples are allowed to cool to room temperature, and then they are characterized with ellipsometry and contact angle analysis after each temperature. Furthermore, AFM is used to analyze samples that have suffered significant damage from thermal exposure, as indicated by ellipsometry and contact angle data.

Aqueous immersion stability is assessed by placing a single coated silicon sample into a closed glass vial with 10 mL of deionized water, and the contact angle and thickness are monitored over the course of two weeks in order to determine the evolution of these data over time. Throughout the experiment, samples are refrigerated at 4°C to minimize the risk of bacterial contamination and biofilm growth, since these phenomena can nullify the experimental data being collected.

6.3 Results and Discussion

A two-dimensional AFM scan of a clean silicon sample after the pre-deposition oxygen plasma treatment can be seen in figure 6.1A. The cleaning procedure detailed in section 6.2.2 produces a clean, flat silicon oxide surface, as evidenced in the figure. AFM was also used to characterize the surface of the silica seed layer. The procedure described in section 6.2.3 produces a thin, rough, silica-like surface which is very rich in reactive sites for further surface modification by organosilane chemistries [36]. In this work, typical seed layer surfaces are approximately 10-20 nm thick with RMS roughness values of 1-2 nm. An atomic force micrograph of a typical silica seed layer can be seen in figure 6.1B.

After monolayer deposition and annealing, samples are characterized with ellipsometry, contact angle analysis, and AFM. Data for films deposited on the clean silicon oxide surface and for films deposited on the silica seed layer surface are given in table 6.1. Due to the non-uniform nature of the seed layer surface, the standard deviation of a data set of multiple ellipsometric measurements of seed layer thicknesses is on the order of 1-2 nanometers. Such a large standard deviation for the seed layer thickness makes it impossible to determine statistically meaningful thicknesses for the films deposited onto the seed layer surface, since

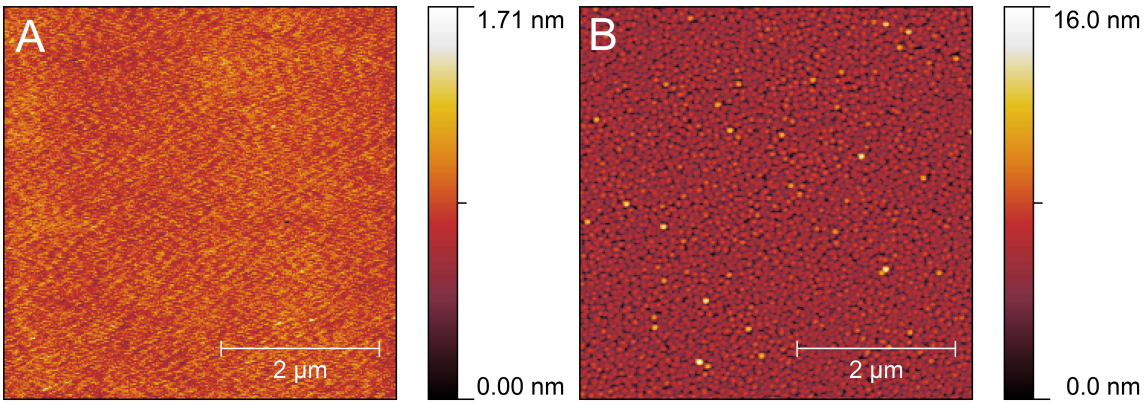

Figure 6.1: Two-dimensional AFM scans of A) a clean silicon surface, RMS roughness is 0.14 nm, and B) a typical seed layer surface, RMS roughness is 1.49 nm. Note the difference in the z-scale of the two images.

	Silicon Oxide			Silica Layer	
	CA	Thickness (Å)	RMS (nm)	CA	RMS (nm)
C18-TCS	109°	24.6	0.25	110°	2.03
C8-TCS	103°	15.0	0.25	109°	1.94
Thermal C18-TMS	109°	21.1	0.36	111°	1.97
Thermal C8-TMS	104°	12.0	0.23	105°	1.53
Chamber C18-TMS	110°	21.0	0.90	109°	2.62
Chamber C8-TMS	105°	12.1	1.87	107°	3.32

Table 6.1: Contact angle (CA), thickness, and RMS roughness (RMS) for deposited films.

precursors used in this study form films with thicknesses of roughly two nanometers or less. For films deposited on the clean silicon oxide surface, data for chlorosilane films and thermally-annealed methoxysilane films are in close agreement with published literature values for monomolecular layers of these precursors [61]. Surfaces that are subjected to chamber annealing, however, typically have higher than normal RMS roughness values.

Results from thermal stability experiments for coatings on clean silicon oxide and on seed layer samples can be seen in figure 6.2. As is evidenced in the figure, the alkyl monolayers studied here exhibit similar thermal stability behavior, regardless of alkyl chain length or binding chemistry. Contact angle and thickness data show that the films exhibit no significant change with temperature exposures up to 200°C. However, at a temperature of 225°C, both contact angle and thickness for all films begin decreasing, indicating that film stability has been compromised. As the exposure temperature reaches 275°C, extensive film damage is evident, as film thicknesses have decreased by 30-50%, and contact angles have decreased by 20-65%. For all films, both contact angle and thickness decrease and then appear to begin to level off as the temperature continues to increase. For instance, the C8 monolayers (monolayer thicknesses of 14 ± 2 Å) have thicknesses of 6 ± 2 Å at 275°C, and they maintain this thickness up to 350°C. Furthermore, even at temperatures of 350°C, none of the samples are again completely hydrophilic (contact angle $< 5°$), indicating the continued presence of hydrocarbon material on the surfaces. These phenomena taken together with the fact that both the eight-carbon and eighteen-carbon precursor films exhibit similar thermal decomposition behavior support a degradation mechanism in which fragments of the alkyl chains of the precursor molecules are removed from the surface, instead of a mechanism of whole molecule desorption. Based on the volatility of these precursors at atmospheric pressure, if whole molecule desorption had taken place, the eighteen-carbon monolayers would have been expected to exhibit a much higher thermal stability than the eight-carbon monolayers, but this is not the case.

The atomic force micrographs shown in figure 6.3 also indicate film damage. After thermal exposure, the surfaces are covered with many small particles in contrast to a uniform

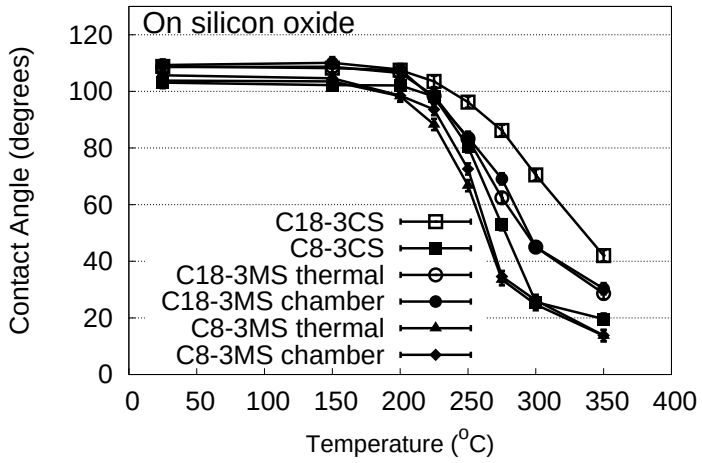

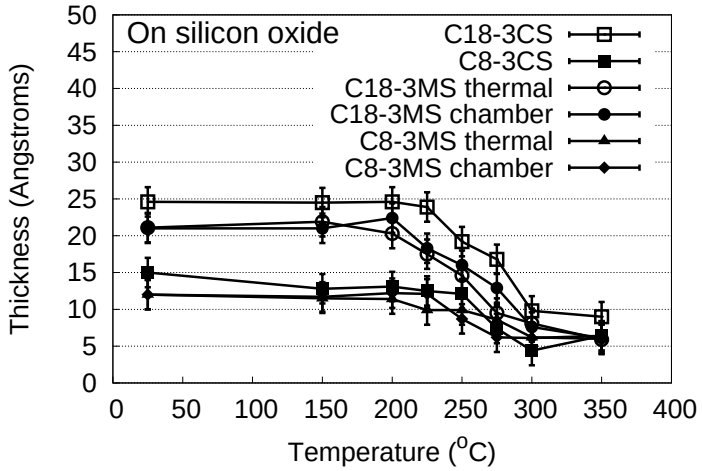

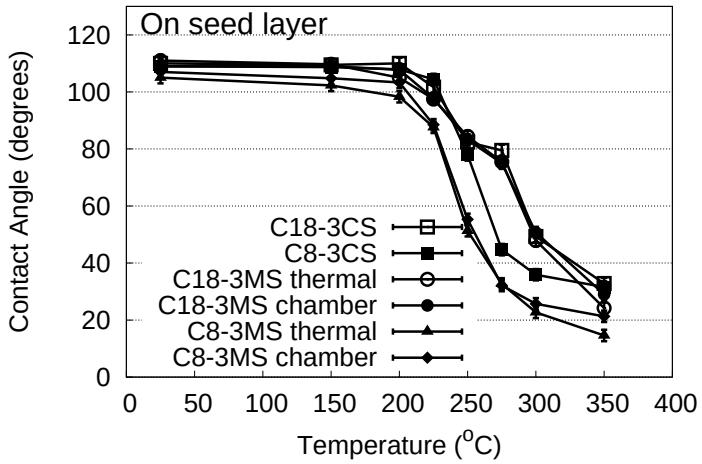

Figure 6.2: Contact angle and thickness versus temperature for films deposited onto silicon oxide and on the silica layer.

coating. RMS roughness data for the films before and after thermal exposure can be seen in table 6.3. In most cases, RMS roughness values have increased, although chamber-annealed methoxysilane coatings do not follow this trend.

Similar thermal stability experiments for C18-TCS monolayers on silicon dioxide surfaces have been reported by Herrmann *et al.* [62] and Ashurst [4], and are in good agreement with the results obtained for C18-TCS monolayers in the present work. The contact angle of C18-TCS monolayers is consistently found to be stable to temperatures up to 200°C, after which point the contact angle begins to decline sharply. Since the films under study in this work have been verified to be monolayer in nature by comparing the contact angle and thickness data to accepted literature values, and since the thermal stability results of C18-TCS monolayers agree with previous literature data, it is believed that the thermal stability data for other precursors studied in this work are valid.

Figure 6.2 illustrates the similarity of contact angle versus temperature data for films deposited on the silica seed layer and clean silicon oxide surfaces. All films are stable up to 200°C, and at higher temperatures, film instability is indicated by decreasing contact angles, regardless of the presence of the seed layer. Based on these data, it can be concluded that the seed layer has not improved the thermal stability of these films on silicon oxide surfaces. In the previous work [36], FOTS monolayers were deposited on to untreated and seed-treated TiN and Al substrates, and these samples were subjected to a single elevated temperature (250°C) for various times. Based on the observation that the contact angle remained unchanged for the seed-treated substrates while it declined substantially for untreated substrates, the authors concluded that the presence of the seed layer enhanced the thermal stability of FOTS monolayers on these substrates. However, a direct comparison of the conclusions of this work to the previous work cannot be made since different experimental techniques were employed to determine thermal stability.

Results from aqueous immersion experiments on clean silicon oxide and seed layer surfaces can be seen in figure 6.4. It is important to note that the thickness reported for the seed layer samples includes the thickness of the seed layer and the thickness of

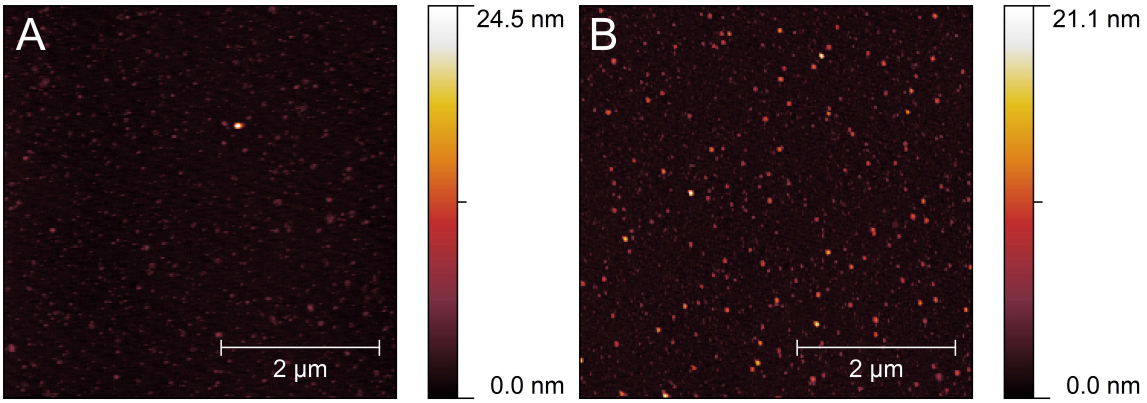

Figure 6.3: Atomic force micrographs of A) C18-TCS (RMS roughness is 0.62 nm) and B) C8-TMS chamber (RMS roughness is 1.05) samples after five minutes of exposure at 275°C. The presence of particles on the surface indicates film damage.

	Silicon Oxide			Silica Layer		
	Initial	Thermal	Immersion	Initial	Thermal	Immersion
C18-TCS	0.25	0.62	2.09	2.03	2.97	3.40
C8-TCS	0.25	0.35	2.33	1.94	3.07	4.67
Thermal C18-TMS	0.36	0.3	0.82	1.97	4.88	3.50
Thermal C8-TMS	0.23	0.74	6.81	1.53	1.63	3.72
Chamber C18-TMS	0.90	0.92	0.68	2.62	2.48	2.61
Chamber C8-TMS	1.87	1.05	3.84	3.32	1.25	3.53

Table 6.2: RMS roughness values (nm) before and after thermal exposure at 275°C for five minutes and aqueous immersion for fourteen days.

the organosilane film. Due to the high standard deviation of the seed layer thickness, calculation of statistically meaningful thicknesses for the organosilane films on the seed layer is not possible. However, in the aqueous immersion experiments, since the concern is tracking the evolution of contact angle and thickness data of a single sample over time, the ellipsometric data is meaningful for this purpose.

For films on clean silicon oxide surfaces, after aqueous immersion there is an initial sharp decline in contact angle followed by a period where the contact angle remains relatively constant, and this behavior is mimicked for films deposited onto the silica seed layer. Contact angles change between 1% and 8% on clean silicon oxide surfaces, and between 1% and 7% on silica layer surfaces over the course of the aquesous immersion experiment, indicating that the presence of the silica layer has not made a significant contribution to improving aqueous immersion stability.

Based on contact angle data alone, one may be inclined to think that the films exhibit fairly good aqueous immersion stability, especially given that contact angles only decrease 10% or less throughout the course of the aqueous immersion experiments. On the contrary, the ellipsometric data provides aditional valuable information about the film performance. It is important to note that the initial sharp decrease in contact angle that nearly all films exhibit corresponds to a sharp increase in thickness as determined by ellipsometry. On clean silicon oxide surfaces, this thickness change is a 16-70% increase over the starting thickness of the organosilane film. The decreasing contact angles and increasing thickness taken together indicate that the films are becoming less ordered. Given the magnitude of the film thickness increase, it is likely that the films are becoming damaged, resulting in the formation of particulate matter on the surfaces, probably through desorption and polymerization of the precursor molecules. This hypothesis is confirmed by examination of the surfaces by AFM, which reveals the presence of particulate matter on the surface after aqueous immersion experiments. AFM micrographs of some of the surfaces can be seen in figure 6.5, and RMS roughness data (table 6.3) show that most samples exhibit drastic increases in RMS roughness values after aqueous immersion.

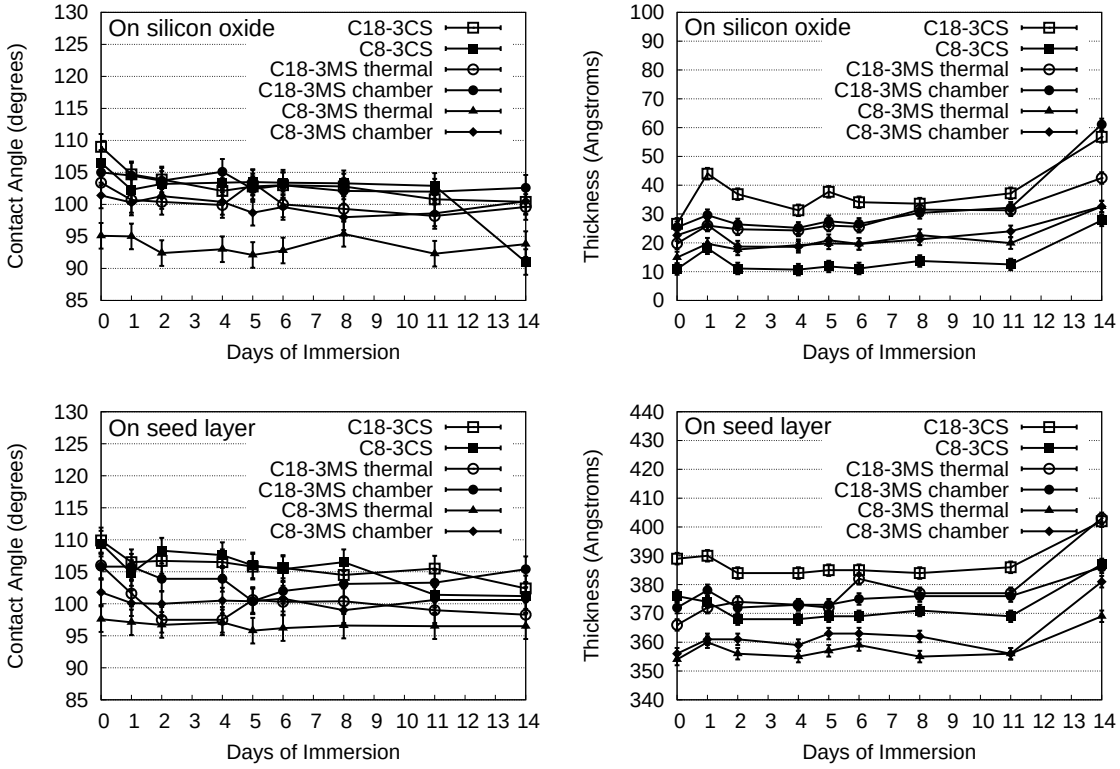

Figure 6.4: Contact angle and thickness data for the precursor films on silicon oxide (top) and on the silica layer (bottom) as a function of aqueous immersion time.

The fact that ellipsometric data provides such insightful information on film stability performance in immersion experiments is an important result. As an example, Parker [63] monitored only the contact angle of various monolayers on silicon oxide surfaces in a five-week immersion experiment. In that study, a relatively stable contact angle over the course of the five week period was observed for a C18-TCS monolayer immersed in water. On the other hand, a perfluorinated monolayer exhibited a drastic decrease in contact angle over the course of the same immersion experiment. When commenting on the immersion stability of these films, Parker pointed out that the perfluorinated monolayer film was very unstable in aqueous environments, but no comments were made regarding instability of the C18-TCS monolayer. The conclusion that the C18-TCS monolayer was relatively stable in aqueous immersion experiments could have only been drawn from its relatively stable contact angle. However, the contact angle behavior for the C18-TCS monolayer observed in the present work is very similar to what was observed by Parker, and without ellipsometric data, inaccurate conclusions about the relatively good stability of the C18-TCS monolayer may have also been drawn.

Considering the thermal stability and immersion stability results together, the broad conclusion that can be drawn from this work is that the presence of the silica seed layer on silicon oxide materials does not improve stability of alkylsilane monolayers. The notion that the silica seed layer allows for the formation of monolayers that are more dense in terms of molecular coverage has been established previously [36], but the present work demonstrates that increased monolayer density does not necessarily translate into improved stability, as might be expected. Therefore, future work on improving the stability of monolayers formed from these types of precursors on silicon oxide surfaces should be focused on intelligent design of the precursor molecules, and not on surface pretreatments that are aimed at increasing monolayer density.

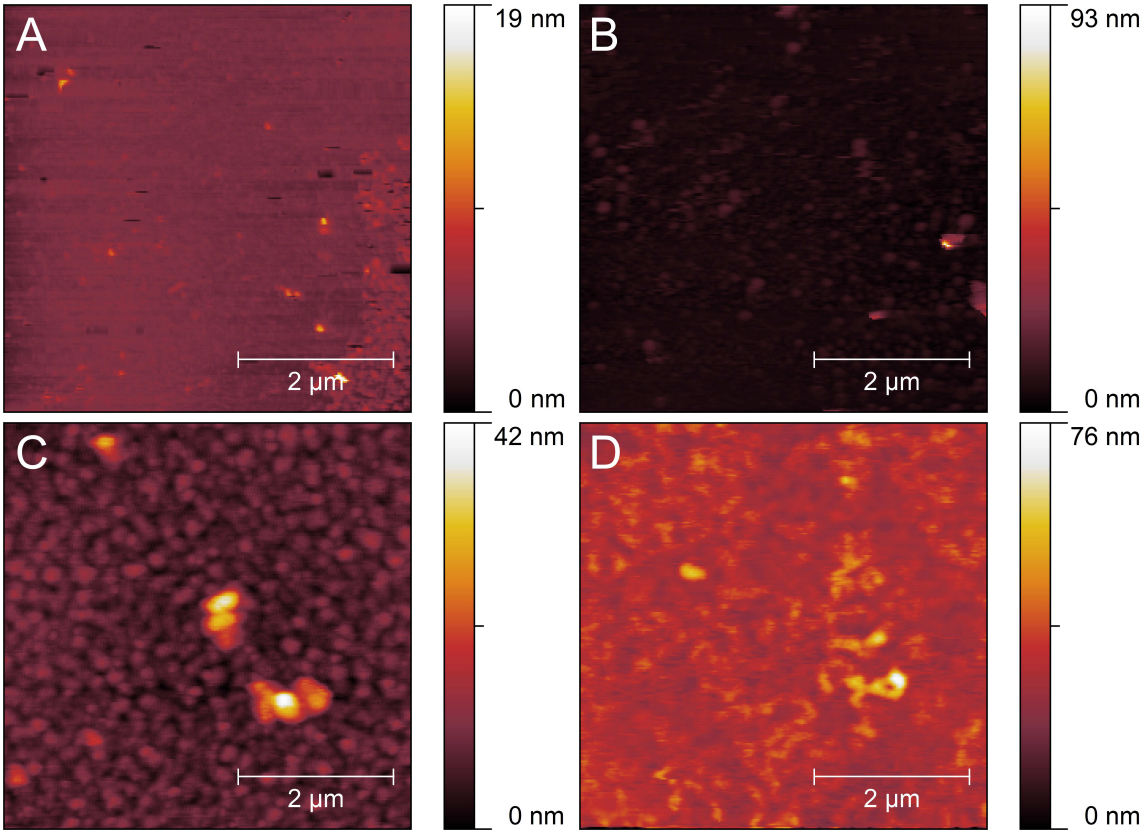

Figure 6.5: AFM micrographs of A) C18-TMS chamber, B) C8-TCS, C) C18-TCS seed, and D) C8-TCS seed after aqueous immersion for fourteen days. The presence of particles and large aggregates on the surfaces indicates that the monolayer nature of the surfaces has been compromised.

6.4 Conclusions

Molecular films of trifunctional chloro- and methoxy- alkyl silanes have been deposited onto normal silicon oxide surfaces and silicon oxide surfaces that had been treated with a silica seed layer material. For films formed from methoxysilane-based precursor materials, the thermal annealing method produces higher quality films as evidenced by lower RMS roughness values and contact angles and thicknesses that are in agreement with published literature values.

This work has shown that the thermal and aqueous immersion stability of alkylsilane monolayers on the silicon oxide surface is not improved by the presence of the silica seed layer. This result is not necessarily in disagreement with the previous work, as the ability of the seed layer to improve stability for films on the silicon oxide surface was not studied previously. Although it has been demonstrated that the presence of the silica seed layer results in films that are more dense in terms of molecular coverage than films deposited on untreated substrates, the increased film density does not necessarily result in improved stability. Therefore, future efforts to improve the thermal and aqueous immersion stability of organosilane films on silicon oxide surfaces should focus on intelligent design of the precursor pendant group rather than on surface pretreatments.

Finally, when measuring immersion stability, the need for collecting film thickness data in addition to contact angle data throughout the course of immersion experiments has been demonstrated. Contact angle data alone cannot provide a complete description of the transient nature of the surface during immersion experiments, and faulty conclusions regarding film stability may be drawn in the absence of ellipsometric data.

Chapter 7

The Vapor-Deposited Thin Silica Film: Morphological and Spectral Characterization

7.1 Introduction

Surface modification is a useful technique to change the surface properties of a material without significantly affecting its bulk properties. It has been employed in reducing friction and stiction in MEMS devices [2–5], in altering surface wettability [6], in tethering biomolecules [7–11] and inorganic nanoparticles [12] to surfaces, and in reducing non-specific protein adsorption on surfaces [13–16] and in micro-channels [17–20]. Organosilane condensation reactions are frequently employed in surface modification strategies, and have in fact been utilized in each of the aforementioned applications. But the chemistry involved in tethering these molecules to a surface requires a favorable concentration of reactive surface hydroxyl groups, thus preventing their application to many materials of technological relevance, such as many polymers and plastics. One might imagine converting a polymer or plastic surface to a surface amenable to organosilane surface modification through the application of an intermediate layer that is rich in reactive hydroxyl groups. However, traditional methods for depositing oxide layers such as silica require operating temperatures in excess of 300°C [34]. This high temperature requirement limits the application of such processes to thermally stable materials, and precludes their application to many polymers and plastics.

In order to leverage the demonstrated success of organosilane surface modification reactions and extend them to other technologically relevant surfaces, a low-temperature method for depositing silica is desirable. The vapor-phase hydrolysis of silicon tetrachloride has been demonstrated to result in the deposition of silica layers at room temperature [35].

It has also been shown that molecular films of alkyl -chloro and -methoxy silanes can be deposited from the liquid [53] and vapor [64] phase onto silica layers formed from this process, and that the resulting films exhibit thermal and aqueous immersion stabilities that are similar to films deposited onto the native oxide of a silicon surface [53]. This is an encouraging result in that it suggests that silica layers formed in this manner are conducive to modification by traditional organosilane chemistries, resulting in molecular films with properties as good as those for films deposited on conventionally prepared silica surfaces. Furthermore, additional data suggest that these silica layers can also be deposited onto some polymers and plastics, affording the ability to extend organosilane surface modification reactions to non-conventional surfaces.

Much analytical work has been devoted to gaining a better understanding of conventional silica surfaces and the role of their surface chemistry in condensation reactions. However, there has been little if any work devoted to characterizing and understanding the silica surfaces formed from the vapor phase hydrolysis of tetrachlorosilane, a necessary undertaking if these films are to be leveraged in new applications. This work seeks to address this shortcoming by investigating the thickness, morphology, and infrared spectral characteristics of silica layers deposited from the vapor phase hydrolysis of tetrachlorosilane. Ellipsometry and atomic force microscopy are utilized to characterize how the thickness and RMS roughness of the vapor deposited silica films change with varying precursor pressures. Each silica surface produced is also examined with attenuated total reflection Fourier transform infrared spectroscopy (ATR-FTIR) to determine its spectral characteristics. Isotopic exchange and dehydration studies are conducted to characterize the region of the spectrum containing information on the surface silanol groups, which are well-known to participate in condensation reactions, and results from these experiments are compared to results obtained for conventionally prepared silica materials.

7.2 Experimental

7.2.1 Materials

Silicon wafers, p-type, with (100) orientation were obtained from University Wafer (Boston, MA). Tetrachlorosilane was obtained from Gelest, Inc. (Morrisville, PA). Concentrated hydrofluoric acid (49%), acetone, and isopropanol were obtained from Fisher Scientific (Fair Lawn, NJ). Deionized water (18 MΩ-cm) was obtained from a Millipore filtration system. Deuterium oxide (100 atomic % D) was obtained from Acros Organics (New Jersey, USA).

7.2.2 Silicon sample preparation

Silicon samples are prepared by an identical method as described in section 6.2.2. This method of cleaning results in silicon surfaces with contact angles of $< 5°$), and RMS roughness values of $\sim$0.2 nm.

7.2.3 Fourier transform infrared spectroscopy

Fourier transform infrared spectra are collected with a Perkin Elmer Spectrum 2000 spectrometer (Perkin Elmer, Waltham, MA) equipped with a DTGS detector. All spectra are recorded at room temperature at 4 cm^{-1} resolution with 100 co-added scans. The IR-transparent material employed is zinc selenide. Two different custom-built infrared chambers, an attenuated total reflection chamber and a transmission chamber, are employed in this work, and are shown in figures 4.6 and 4.7.

7.2.4 Silica deposition

A modified vapor deposition system described elsewhere [64] was utilized in this work, and a schematic is shown in figure 4.3. DI water and tetrachlorosilane are loaded into clean glass vials, and then connected to the vapor delivery system, where they are de-gassed with multiple freeze-pump-thaw cycles with liquid nitrogen. Clean silicon samples are introduced

into the attenuated total reflection chamber, which is evacuated to base pressure before a background spectrum is collected. Then the precursor vapors are admitted into the chamber where they are allowed to react for ten minutes. The system is then evacuated for five minutes, and the infrared spectrum is collected. Detailed experimental procedures are available elsewhere [64]. Then the chamber is opened to the atmosphere, and the silicon samples are removed for further analysis, *ex situ*.

7.2.5 Surface analysis and characterization

Atomic force microscopy

Atomic force microscope images are collected in air (21°C, ∼40% RH) on a commercial AFM (Pacific Nanotechnology Nano-R AFM, Pacific Nanotechnology, Santa Clara, CA) in non-contact mode using silicon AFM tips with resonant frequencies in the range of 150–210 kHz and force constants in the range of 4.5–14 N/m (MikroMasch, Wilsonville, OR). Images are collected at a scan rate of 1 Hz. The manufacturer's software is used to determine the RMS roughness value. Herein, reported values for RMS roughness are the average of two different measurements made on two different samples.

Ellipsometry

After samples are cleaned according to procedures outlined in section 6.2.2, the initial oxide thickness is measured. After silica vapor deposition, the thickness of the oxide layer is again measured, and the difference between these two values is recorded as the thickness of the vapor deposited silica layer. Reported values for film thickness are the average values from a set of eight measurements, four different positions measured on two different samples. For PMMA films on silicon substrates, thickness and refractive index are determined simultaneously.

Contact angle analysis

Water contact angle measurements are obtained by the sessile drop method on a Ramé-Hart model 200 automated goniometer (Ramé-Hart, Inc. Mountain Lakes, NJ) using DROPimage Standard software. Measurement error for this technique is $\pm 2^{\circ}$.

7.3 Results and Discussion

7.3.1 Thickness, RMS roughness, and morphological characterization

Design Expert software from Stat–Ease, Inc. (Minneapolis, MN), is used to investigate the vapor-phase deposition of silica from a design of experiments approach, and a graphical representation of the design space is shown in figure 7.1. The pressures of water and tetrachlorosilane vapors are varied from 0–20 torr, and the measured responses include film thickness and RMS roughness. It is important to point out that experimental design points along the x=0 and y=0 axes are physically meaningless, since there can be no film deposition without both reactants. Hence, these experiments are not conducted, and responses recorded for these design points are zero film thickness and an RMS roughness of 0.2nm, which is the RMS roughness of a silicon sample after cleaning and oxidation.

The measured responses are recorded in the Design Expert software, which calculates the best fit regression models based on analysis of variance techniques. For the thickness data, a model of the form $\log(\text{thickness} + m)$ is chosen, and for the RMS roughness data, a model of the form $1/\sqrt{\text{RMS roughness}}$ is chosen. Plots of the models of film thickness and RMS roughness across the experimental design space can be seen in figure 7.2. Not surprisingly, films become thicker and rougher as the pressures of the precursor gases are increased. Interestingly, it was discovered that by varying the relative amounts of the precursor gases, four distinct film morphologies (referred to as Type I–IV films in this article) can be obtained. Representative atomic force micrographs, with the corresponding thicknesses and RMS roughness values, of each of the four types are available in figure 7.3. Type I and type II surfaces both appear to be comprised of individual particles, but they

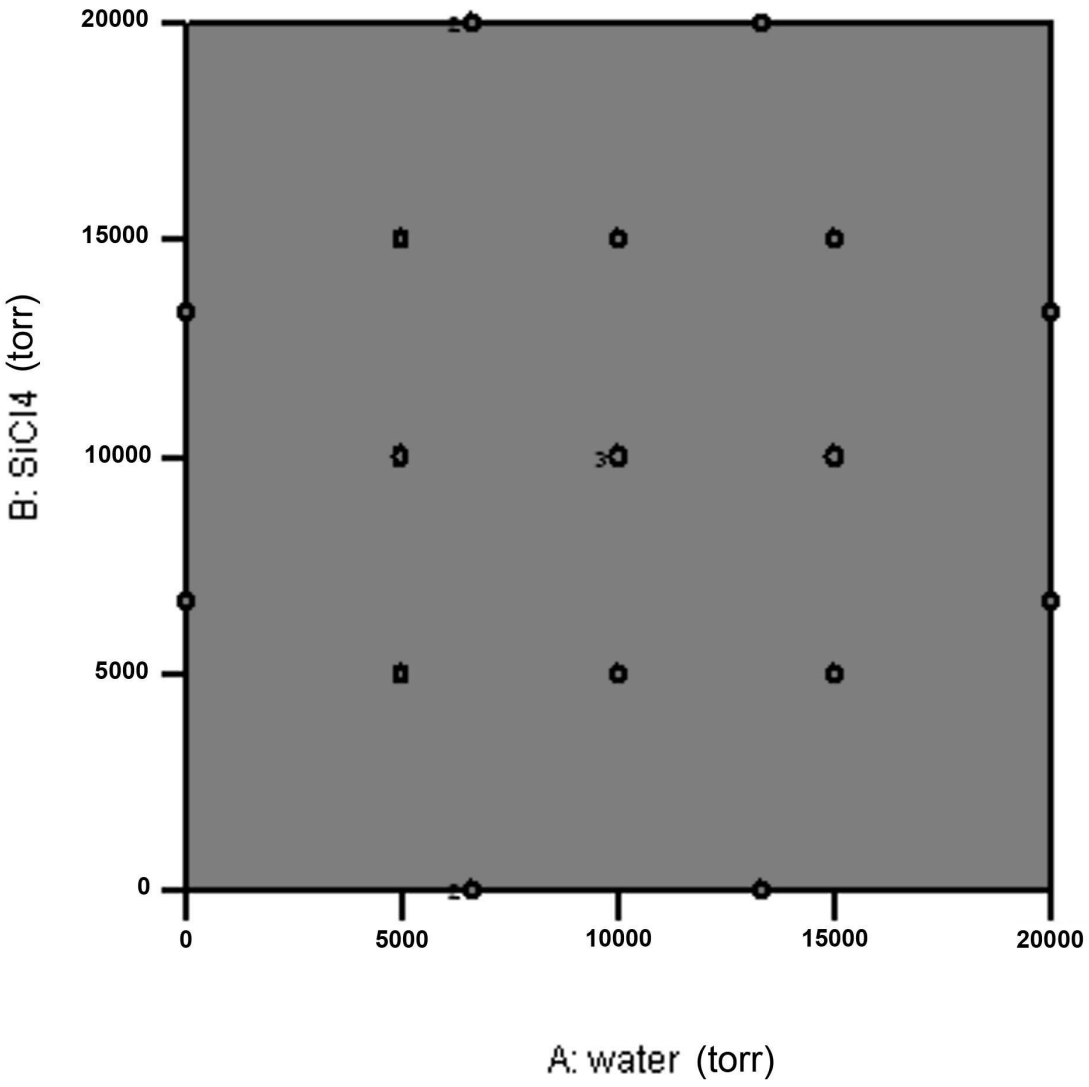

Figure 7.1: Graphical representation of the experimental design for the vapor deposition of silica thin films from the vapor phase hydrolysis of tetrachlorosilane.

differ in the density of particles on the surface; type I surfaces have low surface density, and type II surfaces have high surface density. Type III surfaces have a crenulated film structure, and the RMS roughness value is high compared to other films produced. Type IV surfaces share characteristics with type II and type III surfaces in that some individual particles are present, but there is also some mimicking of the crenulated structure prevalent in type III surfaces. However, the RMS roughness values of type IV surfaces are comparable with those of type II surfaces. It is evident from figure 7.3 that film morphology varies drastically with the relative pressures of the precursor gases. Surfaces with a few individual particles can be obtained (Type I), as well as surfaces with near complete coverage and high RMS roughness values (Type III).

The Roman numerals included on the plot in figure 7.2B show which type of surface morphology is obtained at each experimental point. Type I surfaces are limited to the portion of the design space where tetrachlorosilane is present in low quantities and at a lower pressure than water. Type III surfaces dominate the upper right quadrant of the design space, and type II and type IV surfaces, which are very similar in structure, occupy the region in between. Of the four surface types, type I surfaces are the least desirable for surface modification strategies due to their low surface density.

7.3.2 Spectroscopic characterization

FTIR spectra of the silica films produced by the different deposition experiments are very similar in appearance, and the spectrum shown in figure 5.2B is a representative example. Major peaks present include a broad feature centered at 3400 cm^{-1}, a strong, sharp peak at 1070 cm^{-1}, with a shoulder at 1220 cm^{-1}, and small peaks at 920 cm^{-1} and 810 cm^{-1}. Assignment of the various peaks has been reviewed elsewhere [51, 55]. The broad feature at 3400 cm^{-1} has been previously assigned to O-H stretching vibrations of hydrogen bonded surface silanols and physisorbed water, and the peaks at 1070 cm^{-1} and 810 cm^{-1} are due to various Si-O-Si network modes. The shoulder present at 1220 cm^{-1} is also common to amorphous silica materials [56]. The peak at 920 cm^{-1} has not been

previously assigned, but a tentative assignment is made to an Si-OH bending mode or to Si-O stretching in a silanol group (to be discussed later).

It is well known that the hydroxyl groups present on the silica surface are responsible for its surface chemistry, so it seems necessary to investigate the broad adsorption at 3400 cm^{-1} further. In order to further characterize the broad peak at 3400 cm^{-1}, isotopic exchange experiments are performed. A silica layer is deposited, and the spectrum collected as in previous experiments. The sample remains under dynamic vacuum overnight at room temperature to further remove any physisorbed water. The sample is next exposed to the vapors of D_2O five times over the course of 30 minutes [56], evacuated to base pressure, and the spectrum collected. Spectra obtained throughout the course of this experiment can be seen in figure 7.4. The spectrum of the silica layer collected after deposition exhibits the broad feature at 3410 cm^{-1}, which diminishes slightly in intensity after prolonged evacuation at room temperature. After exposure to the vapors of D_2O, the data clearly show that the broad peak centered at 3410 cm^{-1} is removed, and a new broad peak centered at 2530 cm^{-1} appears. Considering the O-H group on the silica surface as a simple harmonic oscillator, after H/D exchange, one would expect a decrease in its vibrational frequency by a factor of 1.37, and the experimental shift observed (1.35) is in good agreement with the predicted value, and is the same value obtained by other researchers [56]. These findings are evidence that H-D exchange has taken place on the surface of the silica material.

Further characterization of the broad peak at 3400 cm^{-1} is aided by dehydration experiments. An excellent analysis of the dehydration behavior of amorphous silica materials has been conducted by McDonald [55], and the findings are summarized in table 7.1. Important observations from this work are that the vibrational frequency of a surface silanol decreases with increasing strength of a hydrogen bonding interaction, and that sharp absorption peaks indicate that all groups have similar environments, while broad peaks indicate a distribution of geometric arrangements and chemical environments.

To conduct the dehydration experiments, the small, interior ZnSe window depicted in figure 4.6 is loaded into the ATR chamber, and several silica layers are deposited by the

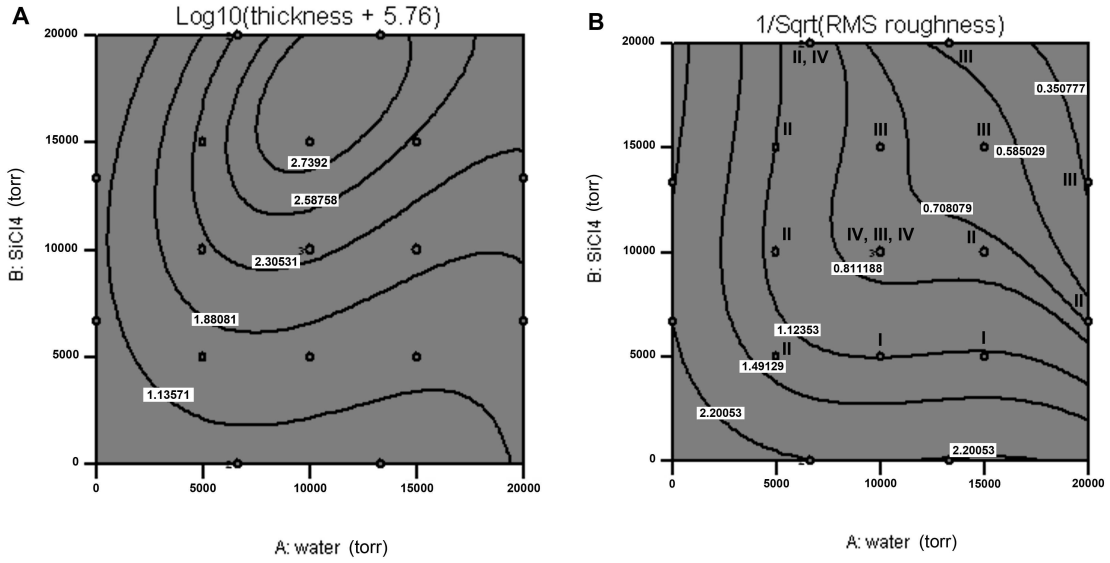

Figure 7.2: Graphical representations of best-fit models of (A) thickness and (B) RMS roughness across the experimental design space. Roman numerals on (B) indicate which type surface is obtained at each experimental point. The contour lines represent calculated values of best fits to regression models of the thickness and RMS roughness, respectively (see text for details).

Frequency (cm^{-1})	Assignment
3750	Isolated SiOH groups.
3740	Very weakly hydrogen bonded SiOH groups which condense at high temperatures.
3660–3680	Weakly hydrogen bonded SiOH groups and adsorbed water molecules.
3500	Moderately strongly hydrogen bonded SiOH groups. Water hydrogen bonded to SiOH groups and to other water molecules.
3400	Water molecules hydrogen bonded to each other and to SiOH groups.
2800–3400	Strongly hydrogen bonded SiOH groups and adsorbed water molecules.

Table 7.1: Peak assignments for various SiOH frequencies, adapted from ref. [55].

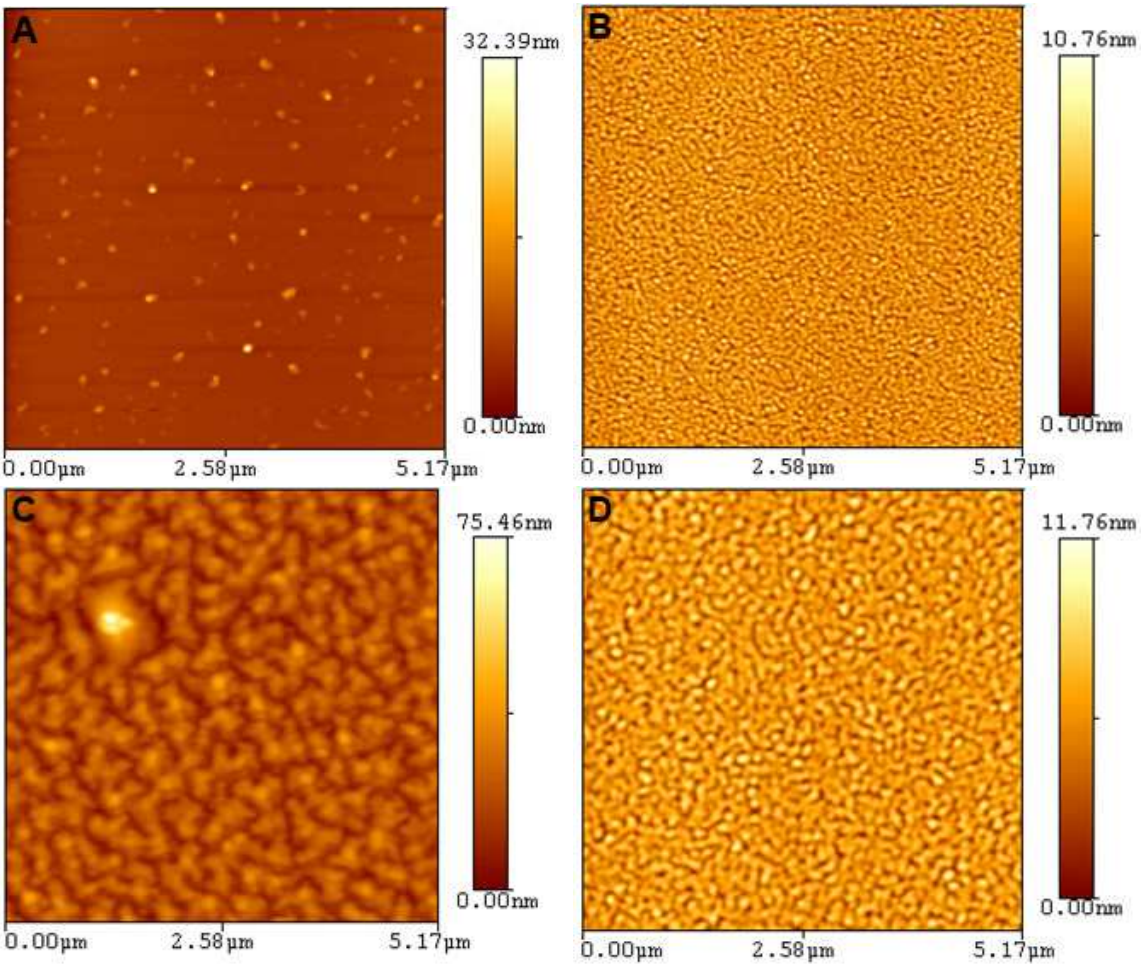

Figure 7.3: Atomic force micrographs of the four different surface morphologies. A) Type I surface, thickness = 2.2 nm, RMS roughness = 1.1 nm. B) Type II surface, thickness = 17 nm, RMS roughness = 1.5 nm. C) Type III surface, thickness = 18 nm, RMS roughness = 6.6 nm. D) Type IV surface, thickness = 22 nm, RMS roughness = 1.5 nm.

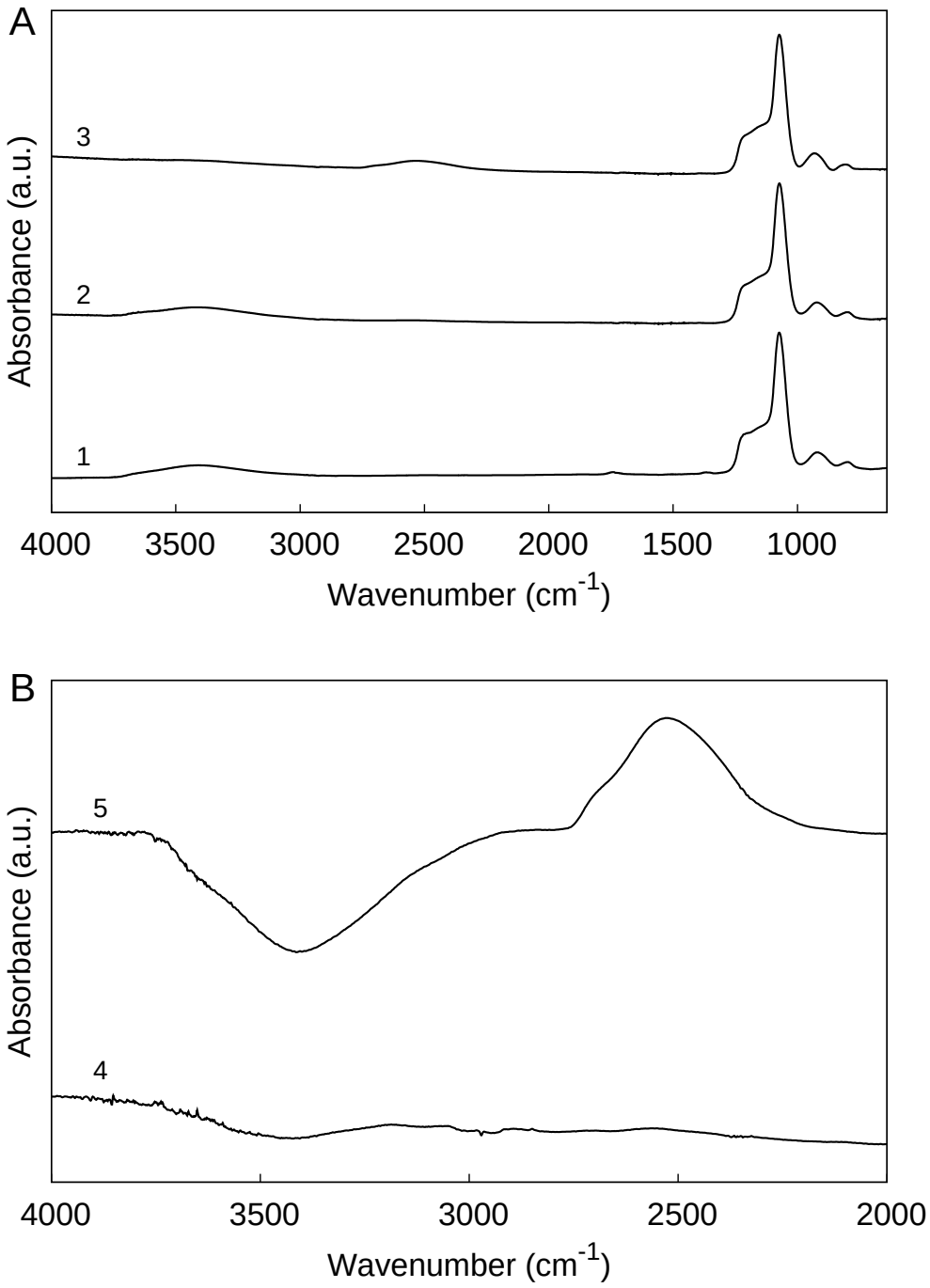

Figure 7.4: A) Experimental spectra obtained during the isotopic exchange experiment. Spectrum 1 is obtained after deposition, spectrum 2 after evacuating overnight at room temperature, and spectrum 3 after the isotopic exchange. B) Difference spectra from A: Spectrum 4 is the difference between 2 and 1, and spectrum 5 is the difference between 3 and 2.

technique described in section 7.2.4. The small window is removed from the ATR chamber and placed in the transmission chamber, which is then evacuated, and a room temperature spectrum is collected. The sample is exposed to an elevated temperature of 100–400°C, in 100°C increments, for 30 minutes, and then allowed to cool slowly to room temperature, where another spectrum is collected. This procedure is repeated for each temperature, so that the same sample is exposed to increasing temperatures. The sample remains under dynamic vacuum throughout the entire experiment. Two noticeable changes to the infrared spectrum of the silica film occur as it is exposed to increasing temperature (figure 7.5A). There is a dimunition of the broad feature at 3400 cm^{-1}, and the strong, sharp peak at 1070 cm^{-1} becomes wider. The difference spectra (figure 7.5B) offer a more detailed view of these behavior. In the high frequency region of the spectrum (3200–3700 cm^{-1}), it is the lowest energy species that are removed first as the exposure temperature is increased, as evidenced by negative absorbance peaks on the low energy side of this region. Furthermore, as the species in the high energy region of the spectrum disappear, there is a concomitant increase in absorbance near 1020–1030 cm^{-1}, which is near the Si-O-Si frequencies.

The physical process proposed to explain the observed changes in the infrared spectra in figure 7.5 is the bridge bonding of adjacent surface silanols. This process involves the reaction of two adjacent surface silanols to produce an Si-O-Si bond, with the elimination of a water molecule. Previously reported data for conventional silica materials (table 7.1) show that O-H stretching from surface silanols and from water molecules contributes to absorbance in the region of the spectrum from 2800–3700 cm^{-1}. However, the dehydration behavior indicated in figure 7.5B do not support the loss of physically adsorbed water molecules from the surface. The data clearly demonstrate that the lowest energy surface species (i.e., the most strongly hydrogen bonded surface species) are removed at lower temperatures. This is the exact opposite behavior of what would be expected in the case of removing physically adsorbed water molecules from the surface. It is proposed that surface silanols in closest proximity to each other, which are expected to display the strongest hydrogen bonding interaction (and therefore, the lowest energy), bridge bond at lower

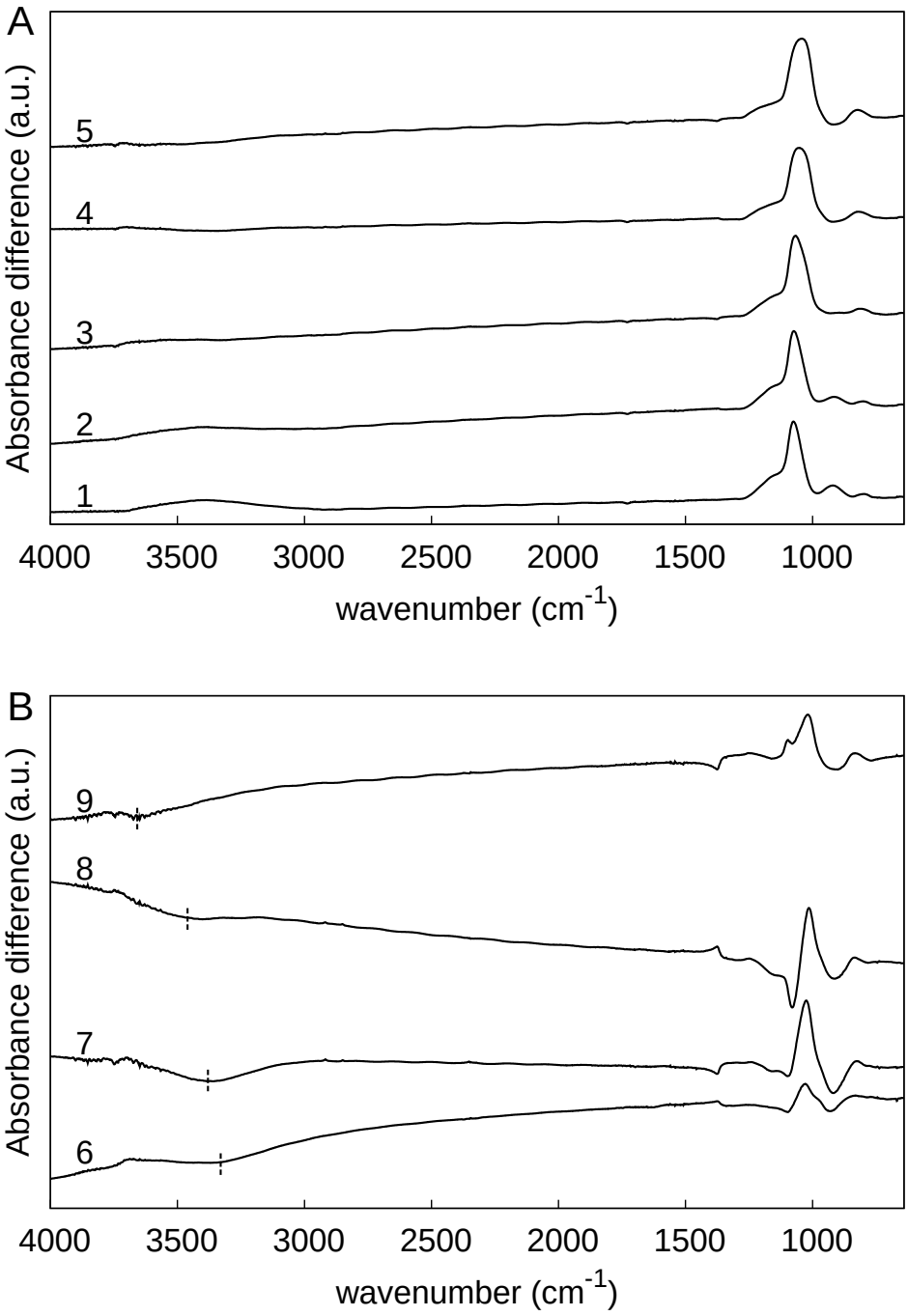

Figure 7.5: A) The spectra of a silica film at room temperature(1), and after exposure to: 100°C(2), 200°C(3), 300°C(4), and 400°C(5), for 30 minutes. All spectra are collected at room temperature. B) Difference spectra from A. Spectrum 6 is 2-1, spectrum 7 is 3-2, spectrum 8 is 4-3, and spectrum 9 is 5-4. Small dashed lines are placed to indicate the position of the minimum in negative absorbance features.

temperatures. Furthermore, the appearance of new spectral features in the region of 1020–1030 cm^{-1}, which are attributed to absorbances from new Si-O-Si bonds, offers further evidence for the bridge bonding hypothesis.

Considering the isotopic exchange and the dehydration experimental data, it is proposed that the broad feature centered around 3400 cm^{-1} is due entirely to surface silanol groups which are present in a distribution of geometrical arrangements and chemical environments. Also, the peak at 920 cm^{-1} may be tentatively assigned to the Si-OH bending mode or to Si-O stretching in a silanol group. Since this peak also diminishes during the dehydration experiments, and since it is close to the range reported for surface silanol absorption modes [56, 65], this assignment can be made with a fair amount of confidence.

The dehydration characteristics demonstrated for the silica films exhibit several notable differences from the characteristics reported for conventional silica materials. It has already been noted that the silica films produced in this work differ from conventional silica materials in that they possess no free surface silanol groups, even after prolonged evacuation. Extending this point even further, the silica films produced in this work produce no freely vibrating surface silanol groups after evacuation at elevated temperatures, as noted by the absence of a peak at 3750 cm^{-1} in figure 7.5. It has been reported previously [55, 66] that upon heating a silica surface, favorably situated surface silanol groups will participate in condensation reactions, forming Si-O-Si linkages while eliminating a water molecule. This results in an increase in the absorption intensity of free surface silanol groups at 3750 cm^{-1}. The increasing absorption intensity arises from silanol groups which are no longer perturbed by surrounding neighbors that have bridge bonded, but this behavior is not noted in the present work. Furthermore, the bridge bonding reaction is not expected until higher temperatures have been reached. McDonald reports that bridge bonding of adjacent silanol groups occurs at temperatures in excess of 300°C [55], while Young reports that this phenomena occurs at temperatures above 170°C [67]. However, in the present work, bridge bonding of surface silanol groups has occurred at temperatures as low as 100°C.

Although it cannot be verified at this point, it is hypothesized that the difference in behavior in the high energy region of the spectrum is due to an increased surface density of silanol groups as compared to conventional silica surfaces. This could explain why the silica films produced in this work do not display absorbances due to free surface silanol groups after prolonged evacuation and after thermal exposure. It is possible that surface silanol groups are present in such high surface density that even after bridge bonding occurs, the remaining groups are still in close enough proximity to continue to interact, although more weakly. In fact, the infrared spectra in figure 7.5B demonstrate a very small positive peak developing at $\sim$3700 cm^{-1} along with the peak developing at 1020–1030 cm^{-1}. The relative intensities of these two peaks shows that the majority of the surface silanols that are consumed produce Si-O-Si bonds (through bridge bonding), but a small fraction of these silanol groups are converted to silanols of higher energy, which are less perturbed.

Even though the vapor deposited silica layers possess no free surface silanols, it has been demonstrated previously that they are amenable to surface modification by organosilane chemistries [53]. Surface modification reactions by organosilicon precursors are generally described to proceed by a mechanism loosely depicted in figure 1.2, which abounds in literature on this topic. That the vapor deposited silica films, which possess no observable free surface silanol groups, do support the attachment of organosilicon molecules suggests that the generally accepted view of the chemistry at silica surfaces may be oversimplified. In the case of surface modification by organosilicon compounds, this seems to be of no effect since the vapor deposited silica films support the formation of monolayers with properties very similar or identical to those formed on silicon surfaces [53]. However, it also has been demonstrated that free silanols and hydrogen bound silanols do in some cases exhibit different surface chemistry [66], so it may be important to consider these differences for some applications. An example where this consideration is important is discussed in the next section.

7.4 Chlorination of Silica Layer Surfaces and Subsequent Reaction with Heterobifunctional Molecules

It is desired to characterize the chemical reactivity of the silica layer surface by exposing it to the vapors of anhydrous silicon tetrachloride, which has been demonstrated to result in the chlorination of fumed silica surfaces [51]. Chlorinated surface may be reacted with molecules with either alcohol functionality [68] or amine functionality [69], resulting in the formation of covalent Si-O or Si-N linkages, respectively.

In this work, heterobifunctional linkers are molecules that possess both alcohol and amine functionality, and therefore can react with chlorinated silica surfaces by more than one mechanism. Based on diatomic bond energy considerations, the Si-O (800 kJ/mol) linkage is more energetically favorable for formation than an Si-N (470 kJ/mol), but both are more favorable than Si-Cl (406 kJ/mol). In this sense, it is believed that heterobifunctional linkers will react with chlorinated silica surfaces preferentially by formation of an Si-O linkage, with the amine end preferentially oriented away from the surface. However, it is unclear to what extent the -OH hetero-end will be preferred for surface reaction over the -NH2 end.

Previous work with surface chlorination of fumed silica surfaces by silicon tetrachloride reports that both monofunctionally and difunctionally adsorbed species are formed on the surface [51]. Upon adsorption, a new peak at 610 $cm^{-1}$is evident, and is assigned as an Si-Cl stretching mode. The chlorination of the silica layer surface by exposure to the vapors of anhydrous silicon tetrachloride is proposed to proceed by the following reaction, where $*$ denotes a surface bound species:

$$*n\mathrm{OH} + \mathrm{SiCl_4} \rightarrow *\mathrm{O_nSiCl_{(4-n)}} + n\mathrm{HCl} \tag{7.1}$$

Initial attempts at surface chlorination of the silica layer proceeded as follows. A silica layer was deposited onto an ATR crystal, and then was dehydrated at 170°C under vacuum in order to create an anhydrous surface. Then a large excess of anhydrous silicon

tetrachloride (10 torr) was admitted into the chamber, and the chamber was allowed to cool to room temperature. After 1 hour, the chamber was evacuated, and the resulting spectrum was collected. The difference spectrum of the silica layer after chlorination relative to the silica layer before chlorination is displayed in figure 7.6, and there are a few very important pieces of information that can be learned from this figure.

First, the spectrum shows that a significant amount of new silica layer material has been formed, even though anhydrous silicon tetrachloride was admitted into the chamber. Since silica layer formation requires the hydrolysis of silicon tetrachloride, this means that even after dehydration at 170°C, there is still a significant amount of water present in the vapor deposition system (not necessarily adsorbed on the silica layer surface, but more likely on the walls of the glass chamber). Second, surface chlorination has taken place, as evidenced by a positive peak at $\sim$610 $cm^{-1}$and a small negative peak at $\sim$3670 cm^{-1}. However, even after a large excess of silicon tetrachloride was added and given one hour to react, the surface chlorination is largely incomplete. This conclusion is based on comparing the absorbance intensity of the surface Si-OH stretching peak ($\sim$3670 cm^{-1}) before and after chlorination, and the absorption intensity of the broad peak at 3400 cm^{-1}. Largely incomplete surface chlorination is a result that is in contrast with similar experiments on fumed silica where nearly 80% of surface silanols are removed by reaction with silicon tetrachloride in 30 min [51].

The presence of the broad peak at $\sim$3400 cm^{-1} may be assigned to Si-OH stretching, as discussed in section 7.3.2. Its existence even after prolonged exposure to a large excess of anhydrous silicon tetrachloride, which scavenges trace water, and the existence of surface Si-Cl species, supported by the presence of the peak at 610 cm^{-1}, are further evidence that support the assignment of this peak to Si-OH stretching due to strongly hydrogen-bonded surface silanols, and not to water. If this peak were due to water, it most likely would have not survived in the presence of anhydrous silicon tetrachloride, which reacts violently with water, and the surface Si-Cl species also would not exist, since these species would be quickly consumed by the remaining surface bound water. Therefore, it is clear that

after exposure to anhydrous silicon tetrachloride, the silica layer surface maintains a large quantity of strongly associated (through hydrogen bonding) silanol groups that coexist with surface Si-Cl species. Based on this observations, it seems likely that surface chlorination by silicon tetrachloride is more favorable with free surface silanols (or at least weakly associated silanols) than with the kind of surface silanols that are present in abundance on the silica layer surface. This is an important result in that it provides additional support for the statements made at the end of section 7.3.2 regarding the need for considerations between different kinds of surface silanol groups.

After developing and validating the aforementioned surface chlorination process, the next step required to meet the objective of this study was to investigate the deposition of 3-amino-1-propanol, which is a commercially available heterobifunctional molecule. It was found that this molecule is sufficiently volatile to be amenable to vapor-phase processing (vapor pressure is $\sim$100 mtorr at 40°C). The chlorinated silica layer surface was exposed three times to the vapors of 3-amino-1-propanol for 30 seconds at room temperature. This deposition resulted in the formation of a surface species resembling an amine hydrohalide (see figure 7.7). It was found, however, that this surface species is weakly associated since it can be removed from the surface by heating to 50°C under vacuum (see figure 7.7).

With this knowledge, subsequent deposition of 3-amino-1-propanol was done at a temperature of 70°C. Experiment showed that this was a sufficiently high temperature to avoid the formation of the amine hydrohalide, but sufficiently low to allow the precursor molecule to interact with the surface. A typical spectrum of the surface bound 3-amino-1-propanol molecule can be seen in figure 7.8. The most important features in this figure are the peak at 1236 $cm^{-1}$and the absence of any peaks corresponding to primary amines. Bergerson and co-workers have investigated the assembly of amine-terminated organic molecules on the chlorinated Si(100) surface, and they have assigned a peak at 1220 cm^{-1}as the C-N stretch of a tertiary amine, which in this case is an amine that is bonded to the surface by two Si-N linkages (spectra collected at room temperature). In the present work, there is a peak located at 1236 cm^{-1} (spectra collected at 70°C), and a similar assignment is

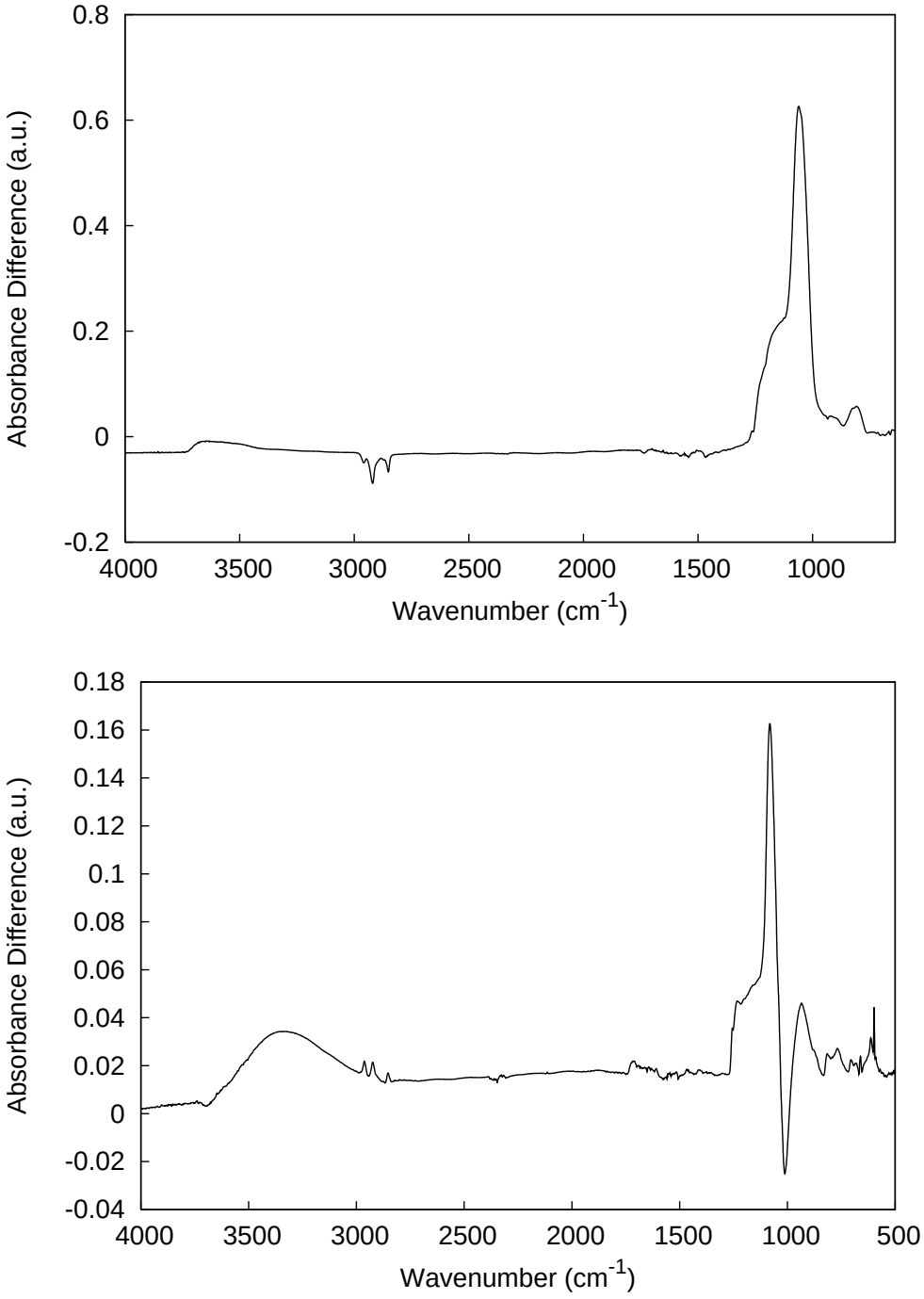

Figure 7.6: An ATR-FTIR spectrum of a silica layer after dehydration at 170°C (top), and (bottom) an ATR-FTIR difference spectrum of the same silica layer after exposure to the vapors of anhydrous silicon tetrachloride for one hour.

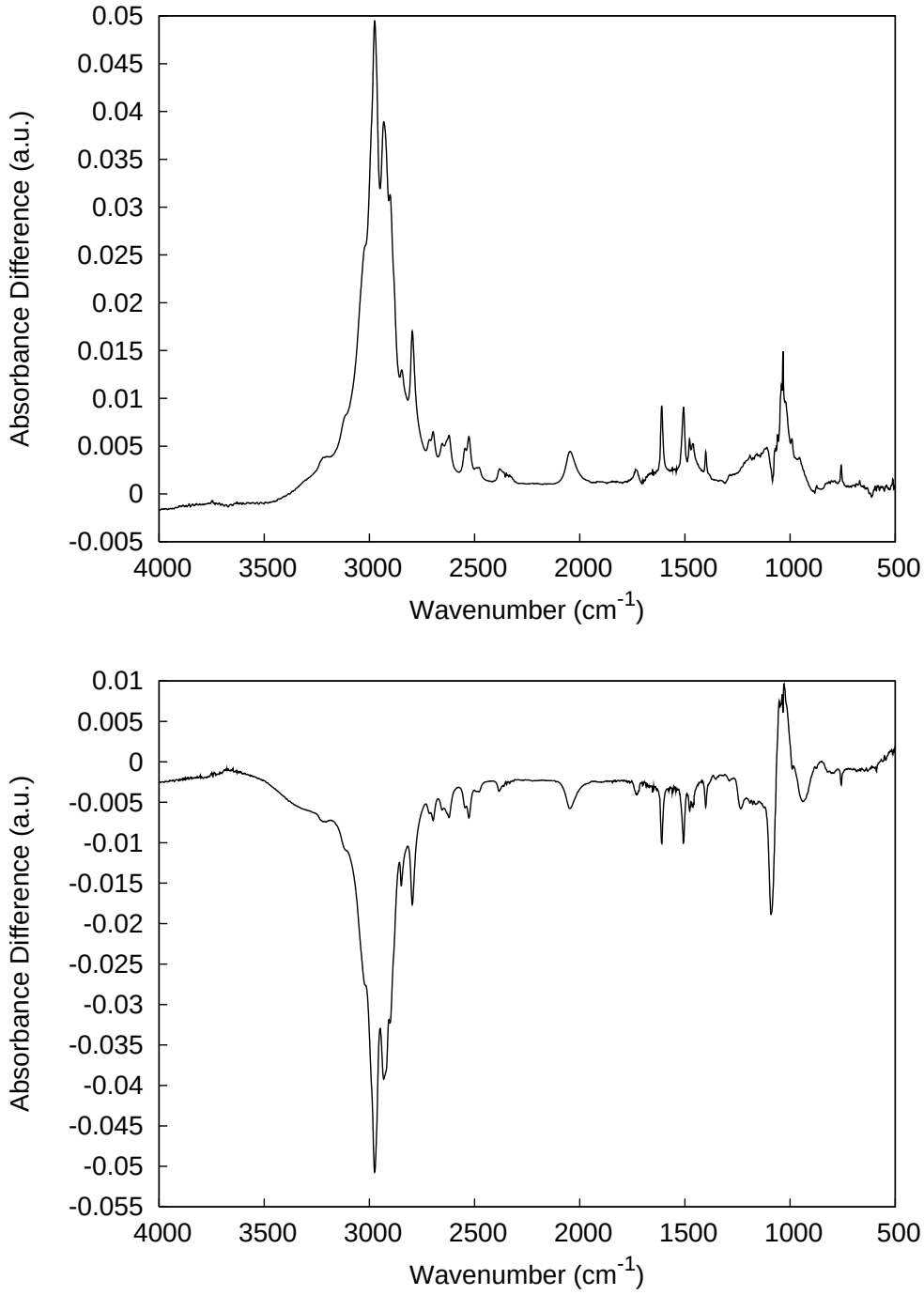

Figure 7.7: An ATR-FTIR difference spectrum of a chlorinated seed layer after exposure to the vapors of 3-amino-1-propanol at room temperature (top), and (bottom) an ATR-FTIR difference spectrum (relative to the top spectrum after heating to 50°C.

made. The slight difference in the position of this peak could be accounted for in the different temperatures the spectra were collected at. The peak at 1236 $cm^{-1}$is present when propylamine is deposited on the seed layer surface, but it is not present when 1-propanol is deposited. These findings further support the assignment of the peak at 1236 cm^{-1} as a C-N stretch of a tertiary nitrogen binded to the surface through two Si-N linkages.

Though diatomic bond angle considerations tell us that the Si-O surface linkage should be more favorable over the Si-N linkage, it seems that for 3-amino-1-propanol, the molecule has preferentially adsorbed by the amine end, and there is no primary amine remaining on the surface. This is contradictory to what was expected to occur, and it is believed that hydrogen-bonding of the precursor molecule to the seed layer surface is to blame. We have already shown that there is incomplete chlorination of the seed layer surface and that a large quantity of unconsumed surface silanols remain. It is believed that these surface silanols interact with the amine end of 3-amino-1-propanol more strongly than they do the the alcohol end, thereby preferentially holding the amine end of the precursor molecule in contact with the surface for a longer period of time. This results in the amine end of the molecule reacting to a greater extent with surface Si-Cl groups than the alcohol end.

Evidence to support this hypothesis comes from observations of the research team during the course of this work. It was noted that anytime a precursor molecule that contained an amine group was introduced into the chamber, the time it took to evacuate the chamber to its base pressure was much longer than for precursor molecules that did not contain amine groups. For instance, both propylamine and 1-propanol were investigated in this work. These are very similar molecules, the only difference being the substitution of an amine group in one molecule for an alcohol in the other. At 50°C, 1-propanol has a vapor pressure of 0.12 bar, and propylamine has a vapor pressure of 1.06 bar (vapor pressure information calculated from Antoine equation constants obtained from NIST Webbook [70]). Thus, propylamine has an order of magnitude higher vapor pressure at 50°C, yet it takes much longer to evacuate propylamine from the vapor deposition system than it takes to

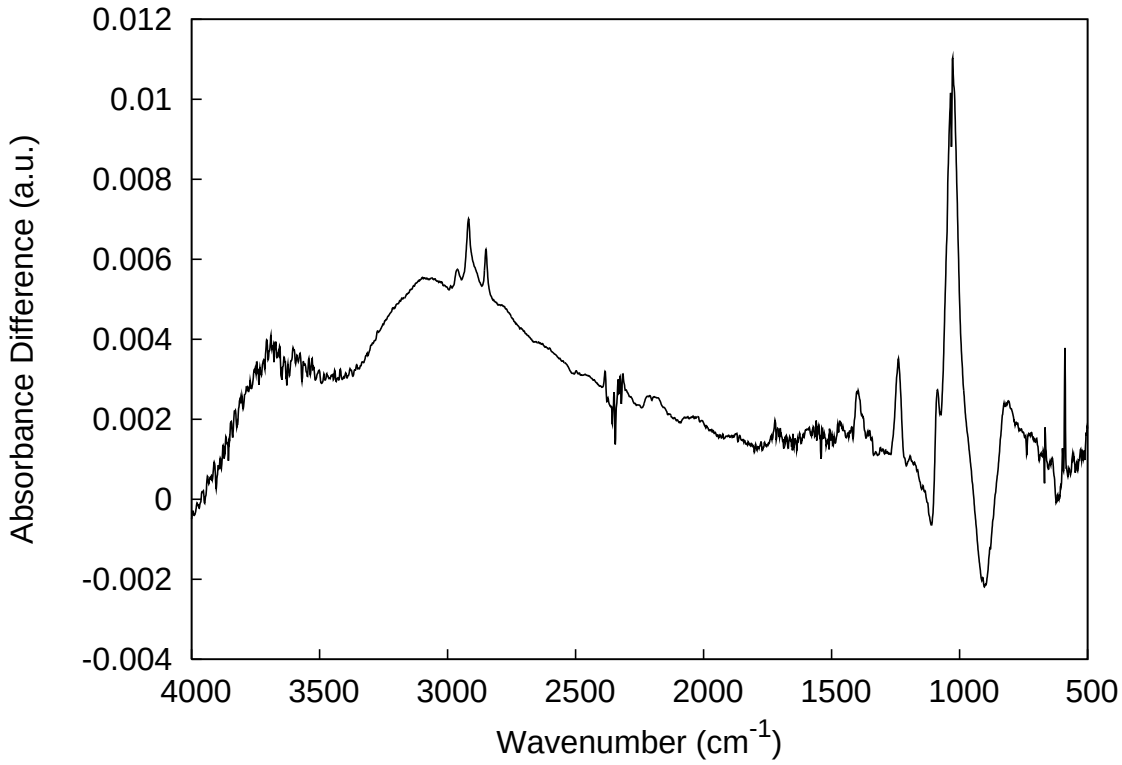

Figure 7.8: ATR-FTIR difference spectrum of a chlorinated seed layer after exposure to the vapors of 3-amino-1-propanol at 70°C.

evacuate 1-propanol. We believe this is evidence of a stronger hydrogen bond between propylamine and the system under investigation.

This work demonstrates fundamental differences between the surface chemistry of conventionally prepared silica materials and the surface chemistry of the vapor deposited silica layer. It has been shown that chlorination of the fumed silica surface by exposure to the vapors of silicon tetrachloride results in the removal of nearly 80% of surface silanol groups [51]. However, chlorination of the vapor deposited silica layer by anhydrous silicon tetrachloride is largely incomplete, as indicated by the remainder of a large quantity of strongly associated silanol groups. Furthermore, the presence of the remaining silanol groups can result in unwanted hydrogen bonding with precursor molecules, especially those containing amine groups.

7.5 Conclusions

Thin silica films deposited by a vapor-phase reaction of water and tetrachlorosilane have been characterized in terms of thickness, RMS roughness, and spectral characteristics. Thickness and RMS roughness of the films vary across the experimental space in an understandable way. Interestingly, four different film morphologies are obtained by varying the relative pressures of the precursor gases.

FTIR spectra of the thin silica films have many commonalities with conventional silica materials. Absorption peaks due to SiOH and Si-O-Si vibrational modes are present and readily identified. Isotopic exchange with D_2O and dehydration experiments are employed to further characterize the high energy region of the spectrum, and it is concluded that the broad feature centered at 3400 cm^{-1} is due to surface silanol groups present in a distribution of geometric arrangements and chemical environments, and is not due to remaining physisorbed water. The fact that the vapor deposited silica films do not display a peak due to freely vibrating surface silanols after heat treatment is in contrast with conventionally prepared silica materials, and a potential explanation for this difference is offered on the basis of an increased surface density of silanol groups. Although the thin silica films

prepared in the manner described here do not exhibit a peak corresponding to a freely vibrating surface silanol, these films have been shown to be amenable to surface modification by organosilane chemistry.

Finally, surface chlorination by exposure to anhydrous silicon tetrachloride is largely incomplete, a result that is also in contrast with similar experiments on conventionally prepared silica materials. Apparently, strongly associated surface silanols may not participate in reactions that they may otherwise be expected to participate in, based on past experimental results obtained on conventionally prepared silica materials.

Chapter 8

Deposition on Model Polymer Surfaces

8.1 Background and Introduction

As the bio-MEMS and microfluidics fields continue to evolve, a shift from silicon and glass-based devices to polymeric devices is being observed. Initially, microfluidics devices were fabricated by leveraging the rich knowledge of silicon micromachining and bulk micromachining, but due to the high costs of fabrication in silicon and glass, these devices were too expensive for commercial application. Polymers have become the preferred materials in these industries, due to their lower cost, ease of device fabrication by various processes, varied and favorable material properties, and, in some cases, pre-existing regulatory agency approvals [28]. To date, several polymers, including polydimethylsiloxane (PDMS), poly(ethylene terephthalate) (PET), poly(methyl methacrylate) (PMMA), and polystyrene, have been adopted for microfluidics applications.

Due to the large surface area to volume ratios commonly encountered in microfluidics devices, the ability to tune the surface chemistry is highly desirable, and therefore robust, stable, and versatile surface coatings are highly sought after [29]. According to deMello, "a primary issue that will in part define the eventual success of polymer substrates [for microfluidics devices] is the development of well-defined surface chemistries that can be used to enhance or eliminate reagent adsorption onto microchannel surfaces, vary electroosmotic flow and allow incorporation of other functional elements such as detectors. [28]" Organosilane surface modification chemistry, with its wide variety of pendant group chemistries and established success in various surface modification applications, could be leveraged to address this pressing technological need. However, many technologically important polymers,

like PDMS, lack sufficient reactive surface groups, making surface modification strategies, especially those involving organosilane precursors, difficult at best.

Although many polymer surfaces are relatively inert, the need for controlling surface chemistry in microfluidics and bio-MEMS applications has necessitated the development of surface modification protocols for these surfaces. For polyesters (PET, PMMA), aminolysis has been demonstrated for the introduction of amine groups on polymer surfaces [30], which can then be used for protein immobilization, but degradation of polyester surfaces during the aminolysis reaction is an undesirable side effect. It has been shown that less degradation results when multifunctional amines are used, but the degradation is not eliminated [30]. Additionally, the utility of this method is limited given that only amine-terminated surfaces can be generated. Polystyrene and polybutadiene surfaces have been modified by UV-assisted surface modification in the presence of trialkylsilanes. In this method, UV light is used to generate highly reactive alkylsilyl radical species, which react with olefins and aromatic rings with high rate constants [39]. A limitation of the technique is that it has not been demonstrated with a large variety of precursor species, but has only been demonstrated with alkylsilanes. Furthermore, the method has only been demonstrated to work on surfaces that contain double bonds or aromatic rings, which would preclude its application to other materials of interest, such as PDMS.

For PDMS, the most commonly employed procedure for altering the surface chemistry is modification by exposure to energy sources, such as oxygen plasmas, ultraviolet light, and corona discharges [18]. It has been shown that oxidation of PDMS surfaces by these energy sources converts the methyl siloxane surface to an SiO_x silica-like layer, which is estimated to be 3 to 10 nm thick [43, 44]. The silica-like layer behaves similarly to other silica materials, and is therefore amenable to silanization by organosilicon compounds, as has been demonstrated [18, 45]. Besides exposure to energy sources, several other methods including exposure to surfactants and lipids [18,46], polyelectrolyte multilayers [47,48], and proteins [33] have been demonstrated.

One common shortcoming of each of the previously discussed techniques is a lack of long-term coating stability. PDMS exhibits an interesting and challenging property, which has been termed "hydrophobic recovery." In short, even after modifying PDMS surfaces by the previously discussed methods, the original, hydrophobic surface properties of PDMS are recovered over time [29]. It is generally agreed that the recovery of the original properties of PDMS is due to migration of free PDMS chains from the bulk phase to the surface [18]. In fact, it has been shown that after oxygen plasma treatment, cracks estimated at between 0.3-0.5 μm deep form in the PDMS surface, which is deep enough to penetrate through the silica-like layer into the bulk phase [43, 49]. It is suspected that the presence of these cracks may aid the process of hydrophobic recovery by providing a path for migration of free PDMS chains from the bulk phase to the surface.

As an alternative strategy to enable surface modification/functionalization of inert polymer surfaces, one might imagine imparting reactivity to these surfaces through the application of an intermediate layer that is rich in reactive groups. An ideal intermediate layer should possess several important characteristics, including easy deposition to a variety of chemically different surfaces, good adherence to the target substrate and stability in aqueous environments, and it should possess sufficient reactive groups to be readily modified by standard surface modification chemistries. Such a technique could open the door for leveraging the proven success of organosilane precursors for surface modification of polymers and plastics, which could potentially lead to major breakthroughs in the fields of bio-MEMS and microfluidics.

We have previously investigated the deposition process and characterized the surface chemistry of thin silica films formed by the room temperature, vapor phase hydrolysis of tetrachlorosilane [54]. We have also demonstrated that these films support organosilane surface modification chemistries using conventional solvent techniques, resulting in monolayers with thermal and aqueous immersion stability properties indistinguishable from those deposited on native silicon oxide surfaces [53]. In this paper, we investigate the deposition of the silica layer on several model polymeric substrates, including PMMA, polystyrene,

and PDMS. These polymers are chosen because they represent a variety of substrate chemistries, and they are commonly employed in microfluidics applications [28]. Deposition of silica onto the various surfaces is characterized by attenuated total reflection infrared spectroscopy (ATR-FTIR), contact angle goniometry, ellipsometry, and atomic force microscopy (AFM). The stability of the silica layer in aqueous environments is assessed by monitoring the layer thickness as a function of aqueous immersion time. In order to demonstrate the utility of this approach, the functionalization of the silica-modified polymeric surfaces by several organosilane precursors is shown. Finally, since this silica deposition process results in a crosslinked silica network on the surface, we investigate whether the presence of the silica layer slows the hydrophobic recovery mechanism on PDMS surfaces.

8.2 Experimental

8.2.1 Materials

Silicon wafers, p-type, with (100) orientation were obtained from Ultrasil Corporation (Hayward, CA). Deionized water (18 MΩ-cm) was obtained from a Millipore filtration system. Tetrachlorosilane and octadecyltrichlorosilane (OTS) were obtained from Gelest, Inc. (Morrisville, PA). Commercial grade polystyrene containers were obtained from Ernest F. Fullam, Inc. (Clifton Park, NY). 950 PMMA A3, a poly(methyl methacrylate) (PMMA) suspension, was obtained from Micro Chem (Newton, MA). Elastomer compound RTV615 (PDMS) was obtained from Momentive Performance Materials (Wilton, CT). Toluene (ACS grade) and hexane (Optima grade) were obtained from Fisher Scientific (Fair Lawn, NJ). All reagents obtained were used as received.

8.2.2 Polymer film deposition

All polymer films are produced by spin coating processes. Identical spin coating recipes are employed to coat both silicon wafers and zinc selenide (ZnSe) ATR crystals for each polymer spin coating solution. ATR crystals are briefly treated with a mild radio frequency

(RF, 13.56 MHz) oxygen plasma (5W, 250 mtorr, 2 minutes) to clean and prepare the surfaces before spin coating. Silicon wafers and ZnSe ATR crystals are spun at 1700 rpm for 45 seconds on a spin-coater. After spin coating, the PMMA films are soft-baked for 30 minutes at 170°C. The films are allowed to cool slowly to room temperature before further analysis.

For polystyrene films a method similar to one reported on by Stange *et al.* is employed, with slight modification [71]. A spin-coating solution of 1.5%(weight/weight) polystyrene in toluene is prepared by dissolving 1.3 g of commercial grade polystyrene in 100 mL of toluene. After the polystyrene is completely dissolved, the solution is filtered through a 0.5 μm filter to ensure that it is free of particles. Spin coating on silicon wafers and ZnSe ATR crystals is carried out at 2500 rpm for 30 seconds. After spin-coating, the polystyrene films are baked at 75°C for 4 hours. The films are allowed to cool slowly to room temperature before further analysis.

For PDMS samples, parts A and B of the RTV615 elastomer compound are mixed together in a 10:1 (A:B) ratio, by mass, for three minutes. The mixture is de-gassed by slowly placing it under vacuum until no more bubbles are visible. This mixture is then cured at 100°C overnight to make bulk PDMS samples. For PDMS films, 0.683 g of the PDMS mixture (after degassing, before curing) is weighed out and added to 40 mL hexane to make a spin coating solution. The solution is filtered through a 0.5 μm filter to ensure that it is free of particles. Spin coating on silicon wafers and ZnSe ATR crystals is carried out at 2500 rpm for 30 seconds. After spin-coating, the PDMS films are cured in an oven at 100°C overnight. The films are allowed to cool slowly to room temperature before further analysis. PDMS spin-coating solutions are used on the same day they are prepared.

In each case, experimental samples are cut from polymer coated silicon wafers with a diamond scribe. The approximate sample size is 8mm $\times$ 8mm.

8.2.3 Silica layer deposition

The deposition of silica layers from the room temperature, vapor phase hydrolysis of tetrachlorosilane has been described in detail elsewhere [54, 64]. A custom built vapor deposition system with *in situ* ATR-FTIR capabilities is employed for depositing the silica films onto polymer-coated ATR crystals and onto polymer-coated silicon substrates, simultaneously. Schematics of the attenuated total reflection chamber and the vapor deposition system are available in Figures 4.6 and 4.3, respectively. Immediately prior to deposition, the polymer surfaces are activated with a brief, RF oxygen plasma (10W, 250 mTorr, 30 sec). The oxygen plasma is employed to promote good adhesion between the polymer surface and the silica film, but it is not required to achieve silica deposition [54]. In this work, each silica deposition process is accomplished by dosing 20 Torr each of tetrachlorosilane and DI water into the deposition chamber, and the reaction is allowed to proceed for 10 minutes. Further process details are described elsewhere [64].

8.2.4 Organosilane functionalization

In our laboratory, the standard relative humidity is approximately 30%, which is too low for OTS deposition. In order to provide sufficient relative humidity to enable OTS hydrolysis, the following protocol is followed. One drop of OTS is added to 40 mL hexane and mixed gently by pipetting. The coating solution is placed on top of a cloth, and a drop of water is allowed to wet the cloth next to the coating solution. Then a larger beaker is turned upside down over the coating solution, taking care to ensure that the water drop is contained underneath the larger beaker with the coating solution. As the cloth dries, water vapor is able to enter the coating solution by diffusion from the vapor phase. Hydrolysis is allowed to proceed in this manner for 45 minutes, and then samples are added to the coating solution, which is then re-covered by the larger beaker. Samples remain in the coating solution for an additional 45 minutes, and then they are rinsed in three stages of neat hexane and dried under a stream of dry nitrogen.

8.2.5 Immersion stability assessment

In order to assess the aqueous immersion stability of the silica layer on the polymer surfaces, silica coated polymer films (on silicon substrates) are placed in glass scintillation vials and immersed in 10 mL of DI water (approximately 1.5 inches deep), and the thickness of the silica layer is monitored over time. As a control, bare polymer films without silica coatings are also included in the experiment to ensure that water immersion does not negatively impact the polymer substrates. For PMMA and polystyrene surfaces, the thickness of the bare polymer film and the thickness of the silica layer on the coated samples are determined by ellipsometry immediately before beginning the experiment. For PDMS, AFM is used to determine the initial thickness of the bare polymer film and the thickness of the silica layer on the coated surface by imaging across a scratch placed in each of the films. Coated and bare PMMA and polystyrene surfaces are observed intermittently over the course of a 9 day immersion experiment, and PDMS samples are observed by AFM at the conclusion of the experiment.

8.2.6 Monitoring hydrophobic recovery on PDMS surfaces

Kim *et al.* have studied the rate of hydrophobic recovery for plasma oxidized PDMS surfaces in a variety of different storage conditions, and it was found that the rate of hydrophobic recovery is fastest when samples are stored in air, and slowest when samples are stored under water [72]. In this study, plasma oxidized and silica-coated PDMS surfaces are prepared and stored in air and under water, and their contact angles recorded over time in order to monitor the rate of hydrophobic recovery. Four PDMS-coated silicon substrates are introduced to the vacuum chamber, and they are treated for 30 seconds with an oxygen plasma at a pressure of 300 mtorr and a forward power of 10W. Then vacuum is broken, and two of the samples are removed. The two remaining samples are returned to vacuum, and a silica layer is deposited by the previously described method. After the required processing is completed, the initial contact angles of each surface are recorded before the experiment begins. One each of the plasma treated and silica coated PDMS surfaces are covered and

stored in laboratory air, and the other samples are immersed in 10 mL of DI water. The contact angle is monitored over time, and samples stored under water are blown dry under a stream of nitrogen before measuring the contact angle.

8.2.7 Surface analysis and characterization

Ellipsometry

Ellipsometric measurements are conducted on a nulling type ellipsometer (Rudolph AutoEL III, Rudolph Research, Fairfield, NJ) equipped with a He–Ne laser ($\lambda = 632.8$ nm) at a 70° angle of incidence relative to the surface normal. The thickness and refractive index of polymer films on silicon wafers are determined simultaneously, and reported values are the averages of 16 measurements, 4 measurements of different locations on 4 different substrates. For silica films deposited on polymers, a two layer model is specified, utilizing polymer film thickness and refractive index values determined for unmodified polymeric films. An accepted value for the refractive index of silicon oxide, $n = 1.46$, is used in this investigation for measurements of silica produced from vapor deposition. The refractive index of the silicon substrate is set at $n = 3.858 + 0.018i$. Reported error values represent 95% confidence limits.

AFM

Atomic force microscope images are collected in air (21°C, ∼40% RH) on a commercial AFM (Nano-R AFM, Pacific Nanotechnology, Santa Clara, CA) in non-contact mode using silicon AFM tips with resonant frequencies in the range of 150–210 kHz and force constants in the range of 4.5–14 N/m (MikroMasch, Wilsonville, OR). Images are collected at a scan rate of 0.5–1 Hz. Gwyddion, a free, public AFM image analysis software, is used to determine the RMS roughness value. Thicknesses of PDMS films and of silica films on PDMS films are determined by imaging over a scratch in the film. The change in height from the flat region of the film to the flat silicon substrate (determined by image analysis software) indicates the total film thickness. The silica thickness is determined by

subtracting the thickness of an unmodified PDMS film from the thickness of a layered silica-PDMS film. Reported error values are 95% confidence limits, which are determined from statistical analysis of data taken from a representative linescan across the surface.

ATR-FTIR

Infrared spectra are collected at room temperature, with 4 cm^{-1} resolution, with 100 co-added scans using an MCT detector. A Perkin-Elmer HATR accessory, which has a fixed incidence angle of 45°, is utilized for ATR-FTIR measurements. In each case, ZnSe ATR crystals are used, yielding a spectral range of 4000–640 cm^{-1}. It is important to note that, in order to probe species on the surface of the polymer films, the polymer film thickness must be less than the depth of penetration of the evanescent wave that is generated as a consequence of total internal reflection. Background spectra of clean ZnSe ATR crystals are collected before they are coated with polymer films. In order to collect background spectra, clean ZnSe ATR crystals are installed to the ATR chamber (after oxygen plasma pre-treatment, described in section 8.2.2), which is then evacuated to base pressure (∼3 mTorr) before the background is collected. After collection of background spectra, the ATR crystals are then promptly coated with the appropriate polymer films by the previously described methods. To collect spectra of the polymer films, the polymer-coated crystals are reinstalled to the ATR chamber after curing, and they returned to vacuum before the spectra are collected. Additional spectra are collected after oxygen plasma pre-treatment and after silica deposition.

Contact angle goniometry

Water contact angle measurements are obtained by the sessile drop method on a Ramé-Hart model 200 goniometer (Ramé-Hart, Inc. Mountain Lakes, NJ) using DROPimage Standard software. Measurement error for this technique is ±2°.

8.3 Results and Discussion

Spin coating of the various polymer solutions results in smooth, continuous polymer films on the surfaces of silicon wafers and on ZnSe ATR crystals, as indicated by visual inspection and analytical techniques. The resulting films are analyzed by AFM, ellipsometry, and contact angle goniometry, and the data are presented in Table 8.1. PMMA films have a thickness of 130 ± 0.2 nm and a refractive index of 1.484, which is in excellent agreement with the manufacturer's specification of 1.488. The resulting penetration depth of the evanescent wave for a PMMA film on a ZnSe ATR crystal varies from 483 nm to 3.02 μm over the 4000-640 cm^{-1} range. Polystyrene films have a thickness of 92 ± 1 nm and a refractive index of 1.583, which is in excellent agreement with prior published data [73]. The resulting penetration depth of the evanescent wave for a polystyrene film on a ZnSe ATR crystal varies from 651 nm to 4.07 μm over the 4000-640 cm^{-1} range. Ellipsometric analysis of PDMS films on silicon fails due to a lensing effect of the incident beam. Although AFM shows that PDMS films are smooth on the micron scale (see the inset in Figure 8.2C, and the RMS value in Table 8.1), it is possible that curing of PDMS films, which results in additional cross-linking, causes stresses in the film. As these stresses relax, they may result in more long-range non-uniformity in the film thickness which is not captured by AFM, or they may result in localized delamination of the film from the underlying silicon substrate. Since ellipsometric analysis of the PDMS film thickness fails, the thickness of the PDMS film is determined by AFM by imaging a scratched region of the film. According to this analysis, the PDMS film thickness is 252 ± 1 nm. Given a value of 1.41 for the refractive index of PDMS films [74, 75], the resulting penetration depth of the evanescent wave for a PDMS film on a ZnSe ATR crystal varies from 421 nm to 2.63 μm over the 4000-640 cm^{-1} range. In each case, the polymer film thickness is significantly less than the penetration depth of the resulting evanescent wave at all wavelengths under investigation, meaning that ATR-FTIR can be effectively used to probe the polymer surface over the entire wavelength range under consideration.

Infrared spectra of the polymer films on the surface of ZnSe ATR crystals are shown in Figure 8.1. Signature peaks present in the infrared spectrum of the PMMA film include absorptions in the 3000–2850 cm^{-1} range, characteristic of methyl and methylene C-H stretching vibrations, a strong peak at 1728 cm^{-1}, characteristic of carbonyl stretching, peaks in the 1500–1300 cm^{-1} range, characteristic of C-H bending vibrations, and peaks in the 1270–1050 cm^{-1} range, characteristic of C-O stretching vibrations [76]. Signature peaks present in the spectrum of the PDMS film include absorptions at 2960 cm^{-1}, characteristic of methyl C-H stretching, strong peaks at 1260 cm^{-1} and 800 cm^{-1}, characteristic of Si-CH_3 stretching and bending, respectively, and strong peaks at 1078 cm^{-1} and 1018 cm^{-1}, characteristic of Si-O-Si network modes [77]. Signature peaks present in the spectrum of the polystyrene film include absorptions near 3025 cm^{-1} and 2920 cm^{-1}, characteristic of aromatic and methylene C-H stretching, respectively, a characteristic aromatic ring vibration near 1600 cm^{-1}, absorptions near 1493 cm^{-1} and 1450 cm^{-1}, characteristic of C-H bending, and absorptions at 754 cm^{-1} and 700 cm^{-1}, which correspond to deformation modes in the phenyl ring [78, 79]. In each case, the infrared spectra confirm the presence of the respective polymers on the surface of the ZnSe ATR crystals.

Since the polymer films are activated by a brief oxygen plasma, it is necessary to determine the effect that the oxygen plasma pretreatment has on the polymer films. The infrared spectra of the polymer films are collected after oxygen plasma treatment, and the difference spectra, which indicate what changes have taken place as a result of oxygen plasma treatment, are calculated. The difference spectra also are shown in Figure 8.1. After exposure to an oxygen plasma, the spectrum of PMMA exhibits negative peaks near most major absorptions that are present in the neat PMMA film. Plasma treatment does not result in any new peaks in the PMMA spectrum, except for a small, broad peak centered around 1020 cm^{-1}, which could correspond to new C-O stretching modes. Based on the spectral data, it can be concluded that, for the most part, oxygen plasma treatment of PMMA surfaces does not chemically transform the surface in any appreciable way, but merely etches away the film.

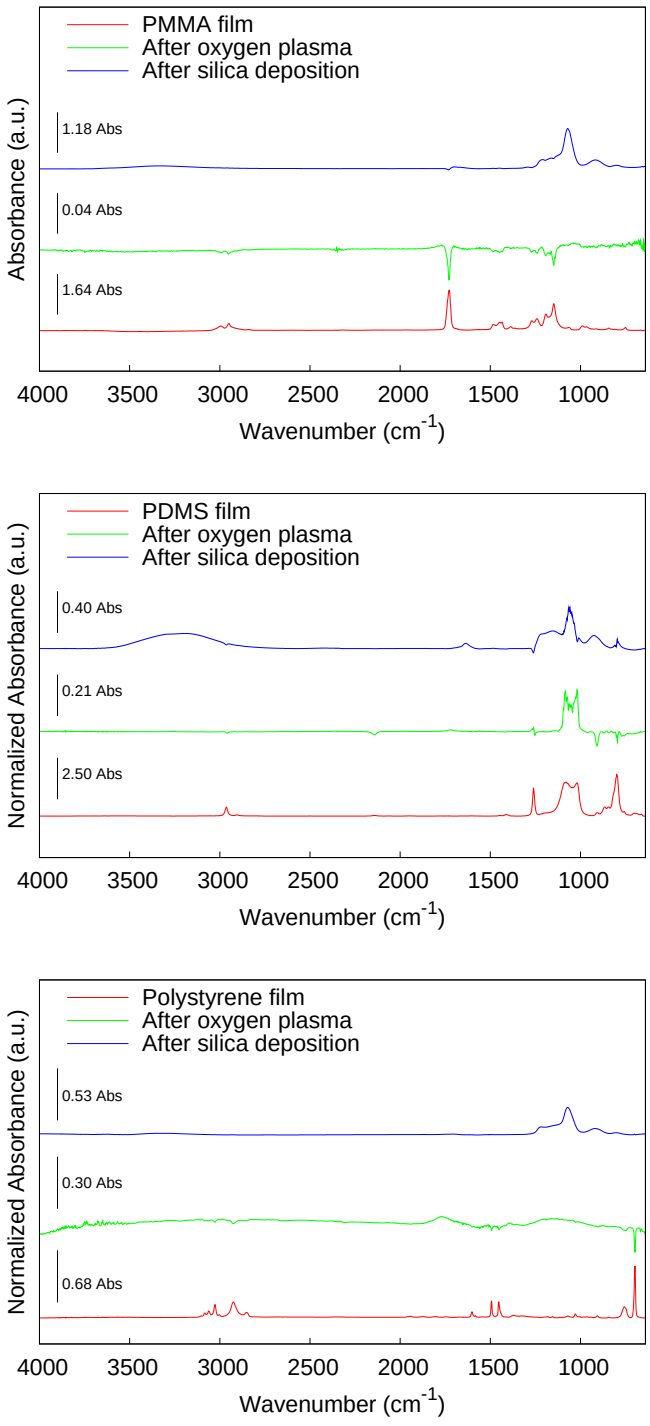

Figure 8.1: Infrared spectra collected throughout the course of the experiments on the different polymer surfaces. Spectra labeled as "after oxygen plasma" and "after silica deposition" are difference spectra calculated from spectra taken before and after the respective treatments.

The most notable changes in the PDMS film after exposure to oxygen plasma are the increase in intensity of two peaks at 1083 cm^{-1} and 1019 cm^{-1}, which are in the typical range of Si-O-Si absorptions present in PDMS samples. The assignment of these modes to Si-O-Si stretching is further confirmed by the fact that exposure to oxygen plasmas has been shown to result in the transformation of PDMS surfaces into a silica-like network [43, 44].

After oxygen plasma exposure, polystyrene films exhibit loss of C-H stretching from both aliphatic and aromatic hydrogens, as evidenced by negative peaks at 3025 cm^{-1} and 2920 cm^{-1}. The most notable features in the spectrum are a sharp negative peaks at 700 cm^{-1} and 754 cm^{-1}, which corresponds to loss of phenyl ring functionality, two broad positive peaks centered at 1757 cm^{-1} and 1147 cm^{-1}, and some small, sharp positive peaks in the range of 3600-3800 cm^{-1}. The new positive absorptions fall in regions of the spectrum where alcohols and esters typically absorb, although carbonyl stretching usually gives rise to strong, sharp absorptions, which is not the case here. Given the extremely reactive and aggressive oxidating nature of oxygen plasma, it is conceivable that some of the phenyl rings on the surface have been broken apart, resulting in the addition of both alcohols and esters. Because of the extreme reactivity of oxygen plasma, it is entirely possible that a large variety of different alcohol and ester species are present on the surface, which could account for some peak broadening.

In addition to spectral analysis, the water contact angles and RMS roughness values of PMMA, polystyrene, and PDMS films on silicon substrates are monitored before and after exposure to oxygen plasma. These data are shown in Table 8.1. Oxygen plasma increases the hydrophilicity of each of the films, as indicated by a decrease in the water contact angle. Polystyrene and PDMS films are extremely hydrophilic after oxygen plasma treatment, with contact angles near 5°. The sharp decline in contact angle on these films can be understood by considering the chemical transformations that have taken place on these surfaces, as indicated by infrared data. The contact angle of the PMMA film after oxygen plasma treatment does not decrease as sharply, but falls to only 43°. Even after exposure to more aggressive plasmas (higher power/pressure), the water contact angle of the PMMA

film remains around 45°, until the film is completely removed (data not shown). In light of the infrared data that indicates that oxygen plasma treatment of the PMMA film does not result in the creation of new chemical species at the surface, but results primarily in etching of the PMMA, this result is not completely surprising. Oxygen plasma treatment has no effect on the film topographies of polystyrene and PMMA films, as indicated by unchanged RMS roughness values. The PDMS film topography remains largely unchanged, but it does exhibit a slight decrease in RMS roughness as a result of oxygen plasma treatment. Upon exposure to more aggressive oxygen plasmas, some cracking of the PDMS film was noted, consistent with literature reports [18, 49].

After oxygen plasma treatment, exposure of the films to the vapors of tetrachlorosilane and water results in the deposition of a thin silica film on the surface of the polymer films. The presence of this film is confirmed visually, given that the color of the film changes due to changes in the composite film thickness and refractive index, and it is also confirmed by ATR-FTIR, ellipsometry, contact angle analysis, and by AFM. Ellipsometric and contact angle data are also presented in Table 8.1. After silica deposition, all surfaces are hydrophilic, as indicated by low water contact angles. Even the PMMA surface, of which the contact angle could not be decreased to less than 45° by prolonged oxygen plasma treatment, is fully hydrophilic after silica deposition. Of the three materials, the PDMS surface has the highest contact angle after silica deposition, which may be explained by the fact that it also has the highest RMS roughness value. Atomic force micrographs of the polymer surfaces after silica deposition are shown in Figure 8.2. The appearance of the surfaces are consistent with previously reported AFM data for silica layers deposited on silicon oxide surfaces [54]. The infrared spectra of the silica films present on the polymer surfaces are also available in Figure 8.1. In each case, the characteristics of the silica layer spectrum are consistent with previously reported infrared data, and peak assignments for the infrared spectrum of the silica layer have been described in detail elsewhere [54]. Each of the analytical techniques employed confirm the presence of the silica layer on the polymer surfaces.

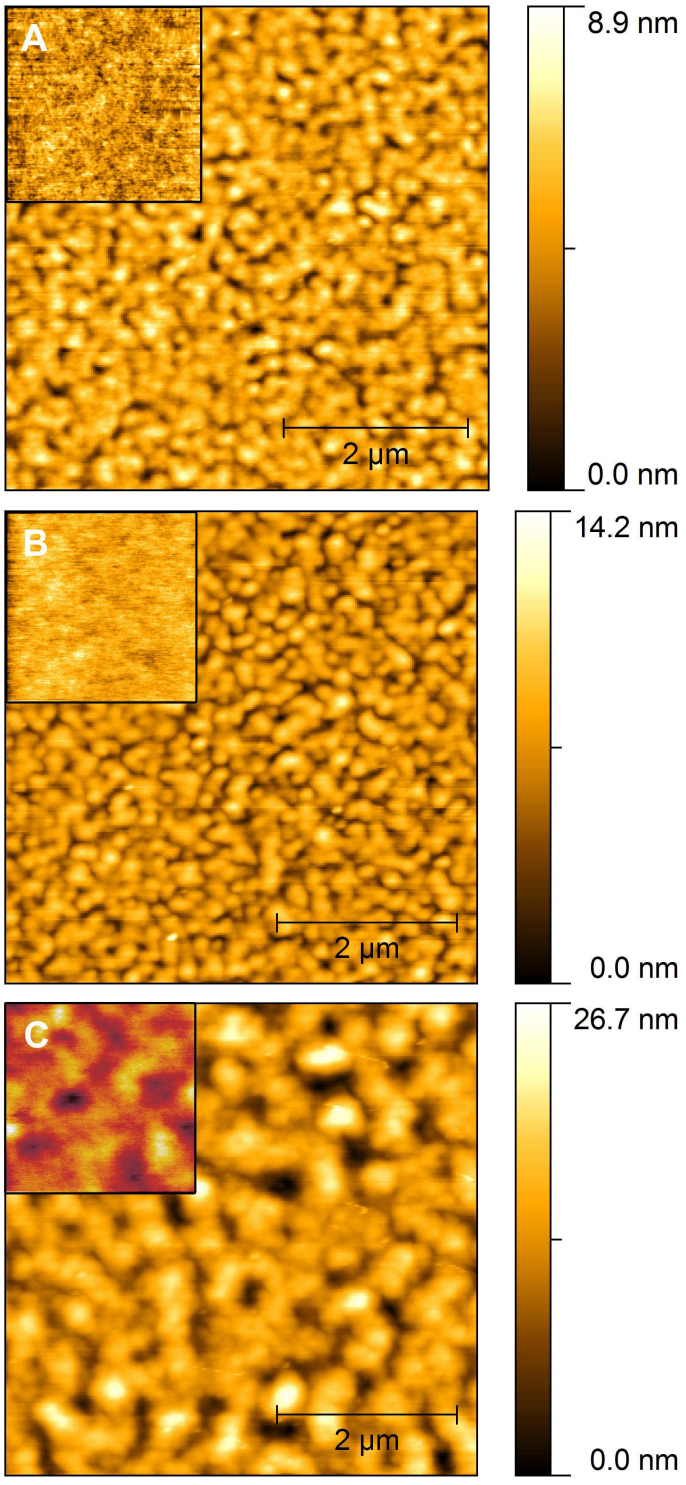

Figure 8.2: AFM micrographs of the polymer surfaces after silica deposition. A) is PMMA, B) is polystyrene, and C) is PDMS. The inset in the upper left corner of each image is an AFM micrograph of the polymer surface before silica deposition.

The immersion stability of silica films on polymer surfaces is assessed by monitoring the thickness of the silica film as a function of aqueous immersion time, and the data are presented in Table 8.2. It is important to note that after one day of immersion, a significant portion of the silica film on PMMA is removed, which is apparent by visual inspection. This is likely due to weak adhesion of the silica layer to the PMMA surface, which can be understood in light of the infrared data previously discussed. Adherent portions of the silica film on PMMA are monitored by ellipsometry throughout the course of the experiment. Silica films on polystyrene and PDMS surfaces appear unchanged over the course of the experiment. The data show that PMMA and polystyrene films are not adversely affected by aqueous immersion, as indicated by their unchanged thicknesses. Furthermore, the data indicate that silica films are stable in aqueous immersion conditions. Although a portion of the silica film on PMMA is removed during the experiment, this is a result of poor adhesion to the PMMA surface, and not a result of poor stability of the silica layer itself, evidenced by the unchanged thickness of the adherent portion of the film. AFM data on PDMS surfaces indicate a slight decrease in the thickness of the PDMS control sample as well as a decrease in thickness of the silica layer on PDMS. A decrease in thickness of the PDMS layer is unexpected, given that the swelling coefficient of PDMS samples immersed in DI water is 1.0 [80]. It is important to note, however, that thickness data obtained from AFM micrographs are highly dependent on leveling procedures, which makes it difficult to reach any concrete conclusions about the change in thickness of the silica film on PDMS surfaces.

AFM micrographs of the silica films on the polymer surfaces after aqueous immersion do show that the silica film does remain intact on the polymer surfaces. These micrographs are shown in Figure 8.3. The appearance of the silica layer on PMMA and polystyrene remains largely unchanged, although the RMS roughness value of the silica layer on polystyrene does increase from 1.59 nm to 4.58 nm. The appearance of the silica layer on the PDMS surface changes drastically after aqueous immersion. The film now has a densified, grainy

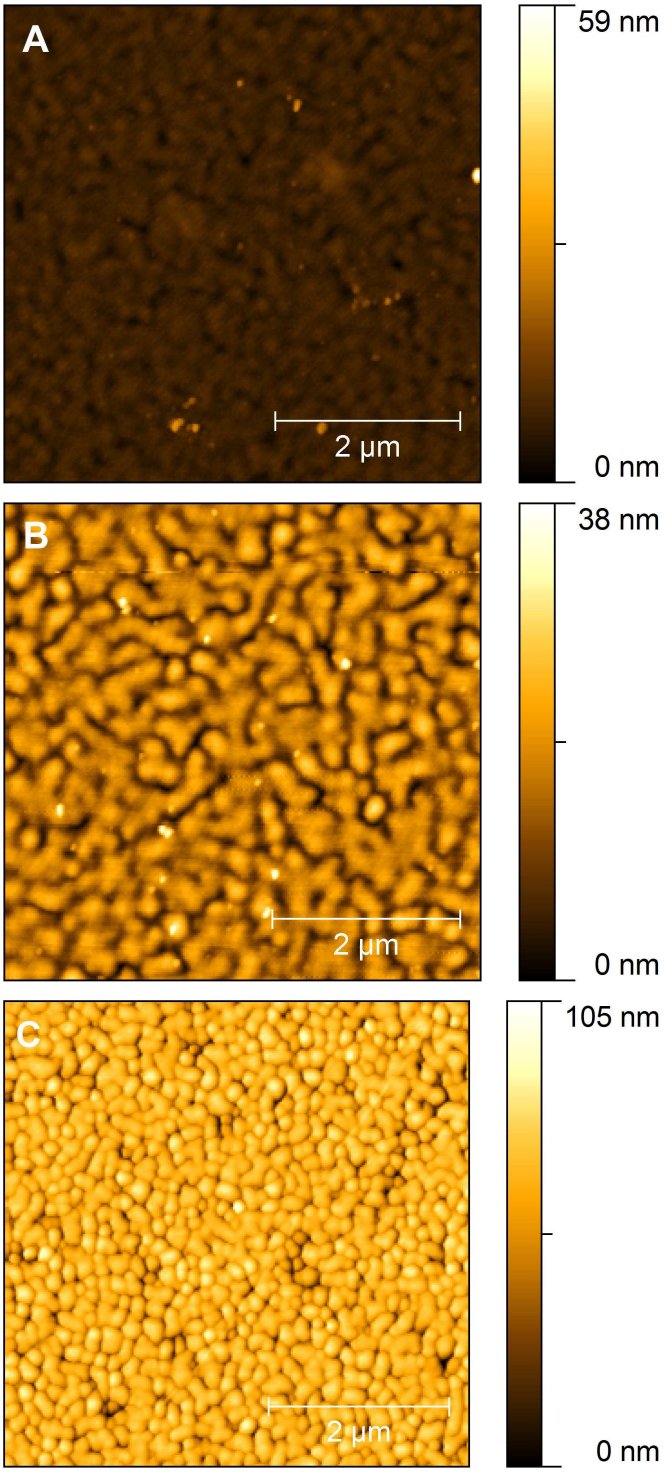

Figure 8.3: AFM micrographs of the silica films on A) PMMA (RMS roughness = 1.74 nm), B) polystyrene (RMS roughness = 4.58 nm), and C) PDMS (RMS roughness = 11.9 nm) surfaces.

appearance, and the RMS roughness value has increased from 3.75 nm to 11.9 nm. Interestingly, the grainy appearance now visible is also slightly visible in the AFM micrograph of the silica film on PDMS after deposition (see Figure 8.2C), but it is buried underneath the taller, irregular surface features. It is possible that the silica layer on PDMS is comprised of a tightly adherent, dense silica network, which is buried underneath a more loosely packed silica material, the latter of which is removed during aqueous immersion experiments. The final thickness of the silica layer on the PDMS surface after aqueous immersion is almost identical to the thickness of the silica layer on PMMA and polystyrene surfaces.

Functionalization of silica coated polymer surfaces by organosilane precursors is demonstrated by deposition of OTS, a conventional and popular organosilane precursor. A clean silicon surface is also coated for comparison to published data. OTS is deposited by the method described in section 8.2.4, and the films are probed by water contact angle goniometry. Data are shown in Table 8.3. For OTS deposited onto a native silicon oxide surface, a contact angle of 107°is obtained. This value is in very good agreement with published contact angle values for OTS deposition (109°from ref. [81]). For bare polymer surfaces, contact angles remain unchanged after OTS functionalization (see Table 8.1), indicating that no monolayer deposition has taken place. For silica coated polymers, contact angles after OTS functionalization are very similar to the contact angle of an OTS monolayer on native silicon oxide. The contact angle data indicate that the formation of OTS films on the silica coated polymer surfaces has been enabled by the presence of the silica layer on these surfaces.

The results of the hydrophobic recovery experiment are shown in Figure 8.4. In agreement with the previous study by Kim *et al.*, the hydrophobic recovery process for PDMS samples stored under water is slower than for samples stored in air. For samples stored in air, the contact angle of silica coated PDMS surfaces initially increases faster than for plasma oxidized PDMS surfaces, which may indicate a faster rate of hydrophobic recovery. However, this trend eventually reverses, and the rate of hydrophobic recovery becomes faster for plasma oxidized PDMS surfaces. It is well documented that samples stored in

Polymer	Curing		Oxygen plasma		Silica deposition		
	CA	RMS	CA	RMS	CA	RMS	Thickness (nm)
PMMA	63°	0.28	43°	0.28	4°	1.11	59 ± 4
Polystyrene	87°	0.25	6°	0.25	5°	1.59	51 ± 2
PDMS	115°	0.72	5°	0.40	13°	3.75	106 ± 20

Table 8.1: Contact angle (CA) and RMS roughness values (nm) for polymer films after curing, after oxygen plasma treatment, and after silica deposition.

Sample	Thickness	
	Before Immersion	After Immersion
PMMA	129	130
S-PMMA	51	47
PS	92	95
S-PS	48	45
PDMS	252	230
S-PDMS	106	58

Table 8.2: Thickness data for various thin films before and after aqueous immersion.

Surface	Contact Angles	
	OTS	As prepared
Silicon oxide	107°	4°
PMMA	65°	63°
S-PMMA	110°	4°
PS	87°	87°
S-PS	109°	5°
PDMS	115°	115°
S-PDMS	115°	13°

Table 8.3: Contact angles of various surfaces after modification by organosilane precursors. Contact angles of the "as prepared" films (before OTS modification) are shown for comparison. Standard measurement error is ±2°. In each case, the designation of the letter 'S' preceding the polymer name indicates a silica coated polymer surface. (For example, S-PMMA designates silica coated PMMA).

laboratory air can become contaminated by adventitious hydrocarbon material, and it is not clear whether the increase in contact angle observed on these surfaces is due to hydrocarbon contaminant or to partial recovery of the hydrophobic properties of the PDMS surface. For samples stored under water, contamination by adventitious hydrocarbon is not a concern. In this case, the presence of the silica layer has slowed the rate of hydrophobic recovery, as indicated by lower contact angles over time versus plasma oxidized PDMS surfaces. It is possible that the presence of a highly crosslinked silica network on the PDMS surface serves as a barrier to slow the diffusion of low molecular weight PDMS segments from the bulk phase to the surface, which is the proposed mechanism for the hydrophobic recovery phenomenon.

8.4 Conclusions

This chapter describes a method of depositing a silica film to polymer surfaces of various chemical functionality. PMMA, polystyrene, and PDMS surfaces, three materials which are commonly employed in microfluidics applications, are investigated. Deposition of the silica film is confirmed on thin polymer films by ellipsometry, contact angle goniometry, AFM, and ATR-FTIR, and results are in good agreement with previous studies on native silicon oxide.

Aqueous immersion experiments show that the silica film itself has excellent stability in immersion applications, but that good adhesion between the silica film and the polymer surface is required to maintain the film integrity during aqueous immersion. For polystyrene and PDMS surfaces, plasma pretreatment results in chemical transformation of the surfaces, which results in improved film adhesion relative to PMMA surfaces, where plasma pretreatment simply etches away surface material.

Organosilane functionalization of silica coated polymers is demonstrated with deposition of OTS, and the contact angles obtained are close to those obtained on native silicon oxide and are in excellent agreement with published values. Furthermore, control experiments on uncoated polymer surfaces indicate that monolayer formation does not take place,

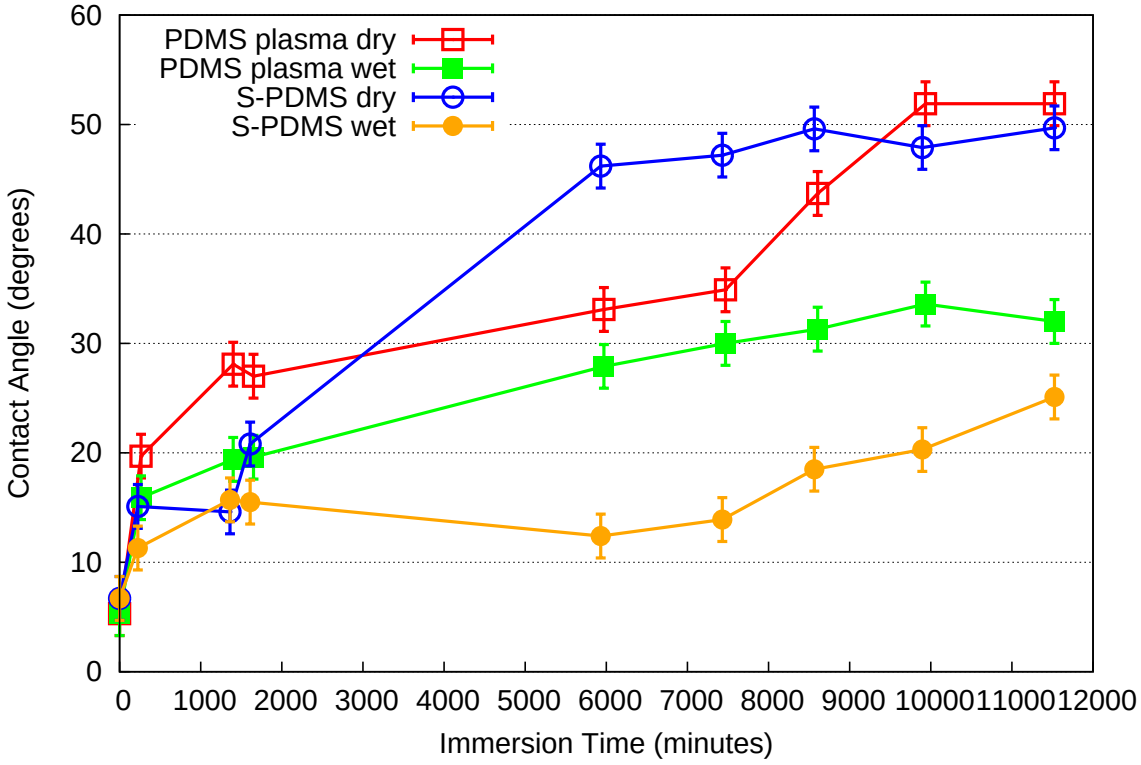

Figure 8.4: Contact angle versus time for plasma oxidized and silica-coated PDMS films stored in air and under DI water. The designation of the letter 'S' in the label indicates a silica coated PDMS surface.

and that it is the presence of the silica layer on the polymer surfaces which enables organosilane functionalization. These results demonstrate the potential of this method, which lies in its ability to impart reactivity to inert surfaces, rendering them receptive to standard organosilane-based coating chemistries. Future experiments will be focused on processing on sealed microfluidic devices, where vapor based coating strategies have demonstrated advantages over liquid phase coating strategies. Finally, when stored under water, the presence of the silica layer on PDMS surfaces slows the hydrophobic recovery mechanism relative to plasma oxidized PDMS surfaces.

Chapter 9

Interfacial Water Structure and the Implications for Interactions with Biological Systems

9.1 Introduction and Background

Due to their small size and small requirement for sample and reagent volumes, bio-microelectromechanical systems (bio-MEMS) and microfluidic devices are being increasingly researched for assays, characterization, and sensing of biomolecules and organisms [20]. Presently, devices capable of recording from, sensing, stimulating, and delivering to biological systems are being developed [21]. Although technology in this area is developing rapidly at the laboratory scale, commercialization of these technologies has been hindered by the inability of such devices to interact with biological systems in a non-immunogenic and stable manner [21]. Non-specific protein adsorption and cell adhesion, two processes that contribute to the phenomena known as biofouling, have proven especially problematic [22, 23].

Non-specific protein adsorption has been demonstrated to result in unwanted behavior and failure in bio-MEMS and microfluidics devices [22, 23]. Since one of the early steps in the biological response to a surface is protein adsorption, and since this step dictates further biological events, controlling this critical step can result in the ability to tune the long term biological response to a surface, which could dramatically increase device efficacy [82].

It has become increasingly apparent that interfacial water structure has profound implications for protein adsorption [82–85]. If a surface supports the formation of a tightly bound interfacial water layer, protein adsorption becomes energetically unfavorable since approaching protein molecules cannot displace strongly adsorbed water molecules. Through

molecular simulation studies on poly(ethylene glycol) (PEG) and OH-terminated monolayers, Zheng *et al.* have shown that the well-known protein resistant behavior of PEG self assembled monolayers is due *primarily* to repulsive forces that arise when protein molecules approach the surface [83]. It is also shown that these repulsive forces are a direct result of the presence of strongly hydrogen-bonded water molecules, and an increasing number of hydrogen bonds between the surface and adjacent water molecules results in an increased repulsive force acting on protein molecules. Experimental work performed in conjunction with these simulations also implicate a direct correlation between the resistance of oligo(ethylene glycol) (OEG) SAMs to protein adsorption and the amount of hydrogen bonds with water molecules [84].

Vogler has demonstrated that the origin of structured water layers lies with the ability of a surface to disrupt water self-association in favor of water-surface association [82, 85]. Evidence suggests that surface Lewis sites, regardless of their chemical nature [86], serve to disrupt water self-association, resulting in the formation of a collapsed, densified, almost "ice-like" interfacial water structure. In fact, the molecular simulations performed by Zheng *et al.* indicate that the water diffusivity at the OEG-SAMs interface (high degree of hydrogen bonding) is reduced by an order of magnitude compared to the one at the OH-SAMs interface (lesser degree of hydrogen bonding) [83], providing theoretical evidence for the existence of an "ice-like" water structure. Also, Alcantar *et al.* have shown that water plasma treatment of PECVD silica films results in an increased number of surface silanols (Lewis sites), and that surfaces receiving water plasma pretreatments absorb less protein than surfaces without plasma pretreatment, which implies an inverse relationship between the number of surface Lewis cites and the amount of protein adsorption [87, 88]. When considered together, these results suggest that the more Lewis sites a surface has available for forming strong hydrogen bonds with water molecules, the more effective it may be against protein adsorption.

Previously, we reported on the infrared spectral properties of a vapor deposited thin silica film [54]. According to our analysis, these films are perhaps more highly hydroxylated

than conventionally prepared silica materials. In fact, the vapor deposited silica films possess much higher relative proportions of absorptions due to silanol groups than do the films prepared by Alcantar and Israelachvili, even after the latter have been fully hydroxylated by water plasma treatment [87]. This conclusion is drawn from comparing the relative intensities of absorption peaks due to Si-O-Si stretching modes and silanol O-H stretching modes in representative spectra from both sources. It is for this reason that we found it appropriate to investigate and compare the structure of the interfacial water layer that exists on several model surfaces, including native silicon oxide, PEG-modified silicon oxide (which is a well-known, protein resistant surface), and the vapor deposited silica layer. Recently, we have also demonstrated the deposition of robust silica films onto a variety of polymer surfaces [89]. The results of protein adsorption studies on the surfaces characterized in the present study as well as on uncoated and silica coated polymer surfaces, which complement the present work, will be published elsewhere.

9.2 Experimental

9.2.1 Materials

Deionized water (18 MΩ-cm) was obtained from a Millipore filtration system. Tetrachlorosilane and methoxy(polyethyleneoxy)propyltrimethoxysilane (PEG-silane) were obtained from Gelest, Inc. (Morrisville, PA). Concentrated hydrofluoric acid (49%), acetone, and isopropanol were obtained from Fisher Scientific (Fair Lawn, NJ). Silicon ATR crystals (50x20x2 mm^3) were obtained from Spectral Systems (Hopewell Junction, NY). Silicon wafers, p-type, with (100) orientation were obtained from Ultrasil Corporation (Hayward, CA). All reagents obtained were used as received.

9.2.2 Surface Preparation and Treatment

Native silicon oxide

A silicon ATR crystal and pieces from a silicon wafer are first sonicated in acetone and isopropanol for 10 minutes each and then dried under a stream of nitrogen. Then the samples are cleaned by an iterative HF etch/oxygen plasma process, which is described in detail elsewhere [53, 54]. This iterative cleaning method is repeated until inspection by contact angle and AFM indicate that a clean (contact angle $< 5°$), flat (RMS roughness $\sim$0.2 nm) surface has been obtained (on samples cut from a silicon wafer), but usually two iterations suffice. After cleaning, the ATR crystal is fitted to the experimental apparatus (schematic available in Figure 4.6), which is then evacuated to base pressure. An additional oxygen plasma is struck in-situ (10W, 250 mtorr, 2 min.) in order to remove all traces of adsorbed organic contaminant.

PEG-modified silicon oxide

PEG functionalization is carried out in a glove bag under a moisture-free environment using oven-dried glassware. The coating solution is obtained by combining 40 mL of toluene, 0.25 mL of PEG-silane, and 0.1 mL of ethylenediamine as a catalyst, and mixing gently with a Pasteur pipette. Freshly cleaned silicon samples are added to the coating solution and are allowed to sit undisturbed for 4 hours. Then the samples are rinsed briefly in neat toluene, and then sonicated in neat toluene for 10 minutes. Samples are dried under a stream of nitrogen and annealed at 115°C for 1 hour in room air.

Silica layer treated silicon oxide

Silica layer processing is carried out in a custom built deposition system (see Figure 4.3) as previously described [54, 64]. A single silicon ATR crystal and multiple silicon samples can be processed on simultaneously. DI water and tetrachlorosilane are loaded into the vapor delivery section of the apparatus and degassed by multiple freeze-pump-thaw cycles

with liquid nitrogen. A pre-determined amount (monitored by pressure) of each precursor is admitted into separate expansion volumes in order to eliminate precursor contact before the deposition is started. After charging of the expansion volumes is completed, the system is evacuated and isolated from the pump, and the contents of the expansion volumes are allowed to expand into the chamber. The reaction is allowed to proceed for 10 minutes, after which the system is evacuated. In this study, silica films are deposited from 20 Torr each of tetrachlorosilane and water.

9.2.3 Surface Characterization

Ellipsometry

Ellipsometric measurements are conducted on a nulling type ellipsometer (Rudolph AutoEL III, Rudolph Research, Fairfield, NJ) equipped with a He–Ne laser ($\lambda = 632.8$ nm) at a 70° angle of incidence relative to the surface normal. An accepted value for the refractive index of silicon oxide, $n = 1.46$, is used in this investigation for measurements of silica produced from vapor deposition. Before surface treatment, the thickness of the native oxide is determined, and reported thickness values are in excess of the native oxide. For ellipsometric measurement of PEG films on silicon oxide, a single film model with a refractive index of $n = 1.45$ has been proposed for organic films and is used in this work [60]. Briefly, the thickness of the initial oxide layer is measured using a refractive index of $n = 1.46$. After the PEG film is deposited, the total thickness of the native oxide and the organic monolayer is measured using a single film model with a refractive index of $n = 1.45$. The thickness of the organic layer is the difference between these two measurements. The refractive index of the silicon substrate is set at $n = 3.858 + 0.018i$. Reported thickness values are the averages of 8 measurements, 4 measurements of different locations on 2 different substrates, and reported errors are 95% confidence limits.

Contact angle goniometry

Water contact angle measurements are obtained by the sessile drop method on a Ramé-Hart model 200 goniometer (Ramé-Hart, Inc. Mountain Lakes, NJ) using DROPimage Standard software. Measurement error for this technique is $\pm 2^{\circ}$.

ATR-FTIR Spectroscopy

Asay and Kim have described the evolution of structured water layers on silicon oxide surfaces as a function of relative humidity by using ATR-FTIR spectroscopy [90], and observed both ice-like and liquid water structures. The experimental techniques employed herein are an adaptation of the previously reported methods.

Infrared spectra are collected on a Perkin Elmer Spectrum 2000 infrared spectrometer with an MCT detector and an appropriately processed silicon ATR crystal (see section 9.2.2). In each case, the background spectrum is taken on an appropriately processed silicon ATR crystal at the system base pressure. The HATR accessory has a fixed 45° angle of incidence. The spectral range from 4000–1500 cm^{-1} is scanned at 4 cm^{-1} resolution, with each spectrum being comprised of 1024 co-added scans. Before data analysis, spectra are baseline corrected and smoothed with the vendor's software.

A schematic of the custom made vapor deposition system is shown in Figure 4.3. The deposition system is constructed around the infrared spectrometer, as depicted in Figure 4.8. Inside the sample compartment of the spectrometer, a glass chamber is sealed to the top of a custom-made aluminum plate with a viton o-ring. The aluminum plate sits on top of a Perkin Elmer HATR accessory. The chamber is connected to a rotary vane pump and to the vapor delivery section of the apparatus, resulting in exposure of the top surface of the ATR crystal to the controlled environment inside the glass chamber. The bottom side of the ATR crystal is kept under continuous nitrogen purge throughout the course of the experiment. The system pressure is monitored from 0.002–100 torr by MKS Baratron capacitance manometers. The relative humidity inside the chamber is varied by admitting controlled amounts of water vapor from the vapor delivery section of the apparatus to

the chamber. After introducing water vapor into the chamber, five minutes are allowed for the system pressure to equilibrate before a spectrum is collected. Relative humidity is calculated as the system pressure divided by the saturation pressure of water. The temperature inside the sample compartment of the spectrometer is monitored and remains constant at 25±0.5°C throughout the experiment. At 25°C, the saturation pressure of water is 23.69 Torr, from the Antoine equation.

9.2.4 Data Analysis

Asay and Kim have reported on the data analysis methods for studying the evolution of the adsorbed water layer structure on silicon through ATR-FTIR spectroscopy [90], and the same technique is employed in the present study. Briefly, the thickness of the adsorbed water layer is determined by comparing the intensity of the water O-H bending mode absorption located at 1635 cm^{-1} to the intensity of the same peak for a bulk liquid water sample on the same surface under study, which is limited by the depth of penetration of the evanescent wave. The thickness determined in this manner can be converted to the number of monolayers by dividing by the mean van der Waals diameter of water, which is 2.82Å. This method is acceptable given that the penetration depth of the evanescent wave into bulk liquid water can be calculated precisely, the position of the band is largely insensitive to adsorbed water layer structure, and the molar absorptivities of ice and liquid water estimated from multiple sources differ by less than 20% [90]. Water structure is determined by examination of the water O-H stretching region of the spectrum from 3700–2800 cm^{-1}. Two peaks centered near 3240 cm^{-1} and 3400 cm^{-1} correspond to ice-like and liquid water, respectively [90–92]. Deconvolution of this region of the spectrum into the two component peaks is accomplished by nonlinear regression techniques, and the relative amounts of ice-like and liquid water are determined by numerical integration of the component peaks.

9.3 Results and Discussion

The refractive index of silicon is nearly constant over the spectral range under study, and a value of 3.42 is used herein. For water, the refractive index at 1635 cm^{-1} is taken as 1.32 [93]. For PEG, a common value for the refractive index of organic monolayers of 1.45 is taken [60]. Consequently, the critical angles for total internal reflection for the systems under study are as follows: for silicon/water, 22.7°, for silicon/PEG, 25.1°, and for silicon/silica, 25.3°. Since the HATR accessory operates at a fixed angle of incidence of 45°, and the calculated critical angles are far less than 45°, dispersion effects can be neglected [94].

9.3.1 Native silicon oxide

The results of water adsorption onto the surface of a clean silicon ATR crystal are presented in Figure 9.1. The results presented are in good agreement with Asay and Kim's previously reported data, but there are some slight differences. Asay and Kim describe three distinct growth regions, which occur approximately from 0-20% RH, from 20–60% RH, and from 60-100% RH. The first region is dominated by the formation of an ice-like water structure, which continues to grow to about 20% RH, after which point the formation of ice-like water slows, and the adsorption of liquid water begins. In this region, the overall growth of the adsorbed water layer is slower than in the first and third regions. Above 60% RH, no further increase in the ice-like water structre is observed, but the growth is comletely dominated by adsorption of liquid water. At nearly 100% RH, they report an adsorbed water layer that is approximately 10 monolayers thick (about 7 monolayers at 92% RH).

Our data presented in Figure 9.1 also indicate three different growth regions which are characterized by different growth rates, as indicated by differing slopes of the liquid and ice-like isotherms. The first region is characterized by rapid growth of the adsorbed water layer up to about 20% RH. From about 20-40% RH, the growth of the water layer slows,

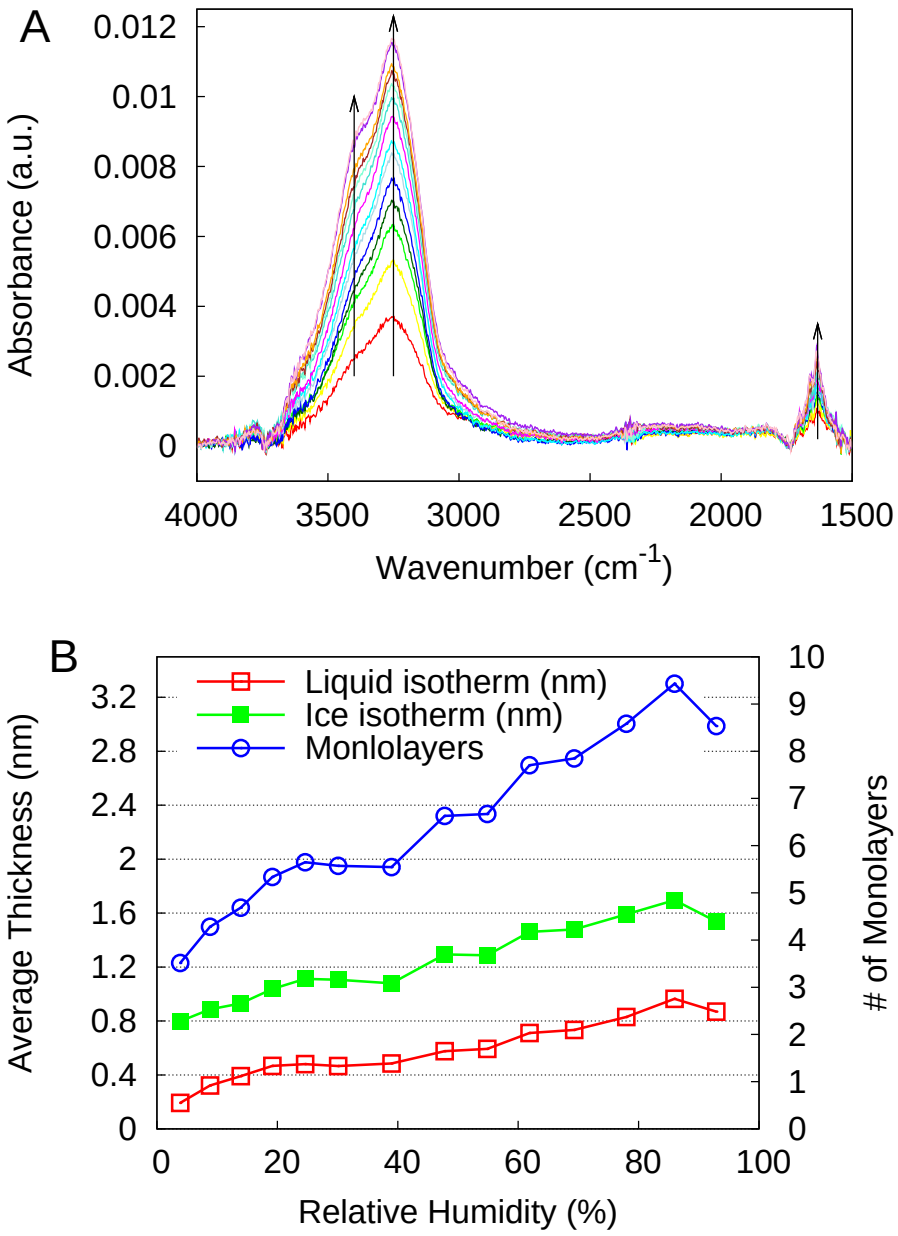

Figure 9.1: (A) ATR-FTIR spectra of adsorbed water on the surface of a clean silicon ATR crystal at increasing relative humidities. The peak positions of ice-like and liquid water are marked with dotted lines at 3250 cm^{-1} and 3400 cm^{-1}, respectively, and the position of the O-H bending mode is marked at 1635 cm^{-1}. Arrowheads denote the direction of increasing relative humidity. Spectra correspond to relative humidities of 3.9%, 8.8%, 13.9%, 19.2%, 24.6%, 30.1%, 39.0%, 47.8%, 54.9%, 61.9%, 69.3%, 78.0%, 86.0%, and 92.9%. B) Graphical representation of the structure and relative thickness of the adsorbed water layer as a function of relative humidity, as determined from infrared spectra.

as indicated by nearly horizontal slopes of the isotherms. Above 60% RH, the water layer again grows rapidly, in agreement with Asay and Kim's data. At high relative humidities, the water layer growth seems to saturate at around 9 monolayers of water, which is in good agreement with the value of 10 monolayers reported by Asay and Kim. The major differences between the present study and the previously reported data lie in the behavior of the ice-like and liquid water isotherms. It was previously reported that the growth of the adsorbed water layer is dominated completely by the formation of ice-like water, and that liquid water does not form until relative humidities of approximately 30% are encountered. Furthermore, Asay and Kim report that beyond 60% RH, the ice-like structure experiences no further growth, and the growth of the adsorbed water layer is completely dominated by adsorption of liquid water. In the present study, ice-like and liquid water isotherms grow together, and at nearly an equal rate, across all relative humidities studied.

It is possible that the differences in growth characteristics between the current study and Asay and Kim's earlier study can be explained by differing surface preparation procedures. In the earlier work, the surfaces of silicon ATR crystals are cleaned by UV/O_3 treatment, *ex situ*. In the present work, surfaces are cleaned by oxygen plasma *in situ*, immediately before beginning the experiment, which guarantees that the starting surface is free of any adsorbed hydrocarbon material. In the previous work, the surfaces can only be free of hydrocarbon material as long as no adventitious hydrocarbon materials adsorb on the surface after UV/O_3 treatment. Another possibility is that the *in situ* cleaning of the surface by oxygen plasma induces charge on the surface [95], which can affect the adsorbed water layer structure [96]. Despite the described differences, there is still relatively good agreement between the present study and the previous work, especially when considering the *total amount* of adsorbed water determined by each method.

9.3.2 PEG-modified silicon oxide

Modification of silicon surfaces by PEG-silane by the method outlined in section 9.2.2 results in the formation of a monolayer of PEG on the silicon surface. Ellipsometric analysis

of coated silicon substrates indicates that the PEG layer is 16.2 ±1.1 Å thick, the contact angle is 38.2°, and the RMS roughness is 0.25 nm. The thickness and contact angle values are in fairly close agreement with previously reported data for similar monolayers formed from the trichlorosilane analogue of the PEG-silane employed in the present work [97]. The low RMS roughness value is also indicative of monolayer formation.

The results of water adsorption onto the surface of a PEG-modified silicon ATR crystal are presented in Figure 9.2. In this case, again, there are three distinct regions of growth of water layer structure. The first region persists up to approximately 15% RH, and is characterized by rapid growth of both ice-like and liquid water structures. The second region exists approximately between 15% and 35% RH, and is characterized by a sharp decrease in the rate of adsorbed water layer growth. Furthermore, the growth of ice-like water slows significantly. The third region exists at relative humidities in excess of 35%RH, and it is characterized by rapid growth of the adsorbed water layer. Initially, the water layer growth in this region is comprised mostly of liquid water adsorption, and is also characterized by a slight decrease in the amount of ice-like adsorbed water. However, at relative humidities in excess of 60%, adsorption of water in an ice-like form is renewed, and continues throughout the experiment. At relative humidites in excess of 80%, a nearly exponential increase of the adsorbed water layer thickness is observed. At 85% RH, the amount of adsorbed water is equivalent to 24 monolayers, which is 2.5 times greater than the amount of adsorbed water on the surface of native silicon oxide at the same relative humidity. It also interesting to note that the behavior of the liquid and ice-like isotherms in this case agree closely with the behavior reported by Asay and Kim. This result gives credibility to the argument that the oxygen plasma pre-treatment, which was employed in the experiment on native silicon oxide but not on the PEG-modified silicon oxide, may have affected the adsorbed water layer structure on the silicon oxide surface.

There are also two peaks at 3743 cm^{-1} and 3853 cm^{-1} which display changing absorbances throughout the course of the experiment. There are few chemical species that have absorptions in this high energy region of the infrared spectrum, with the exception of

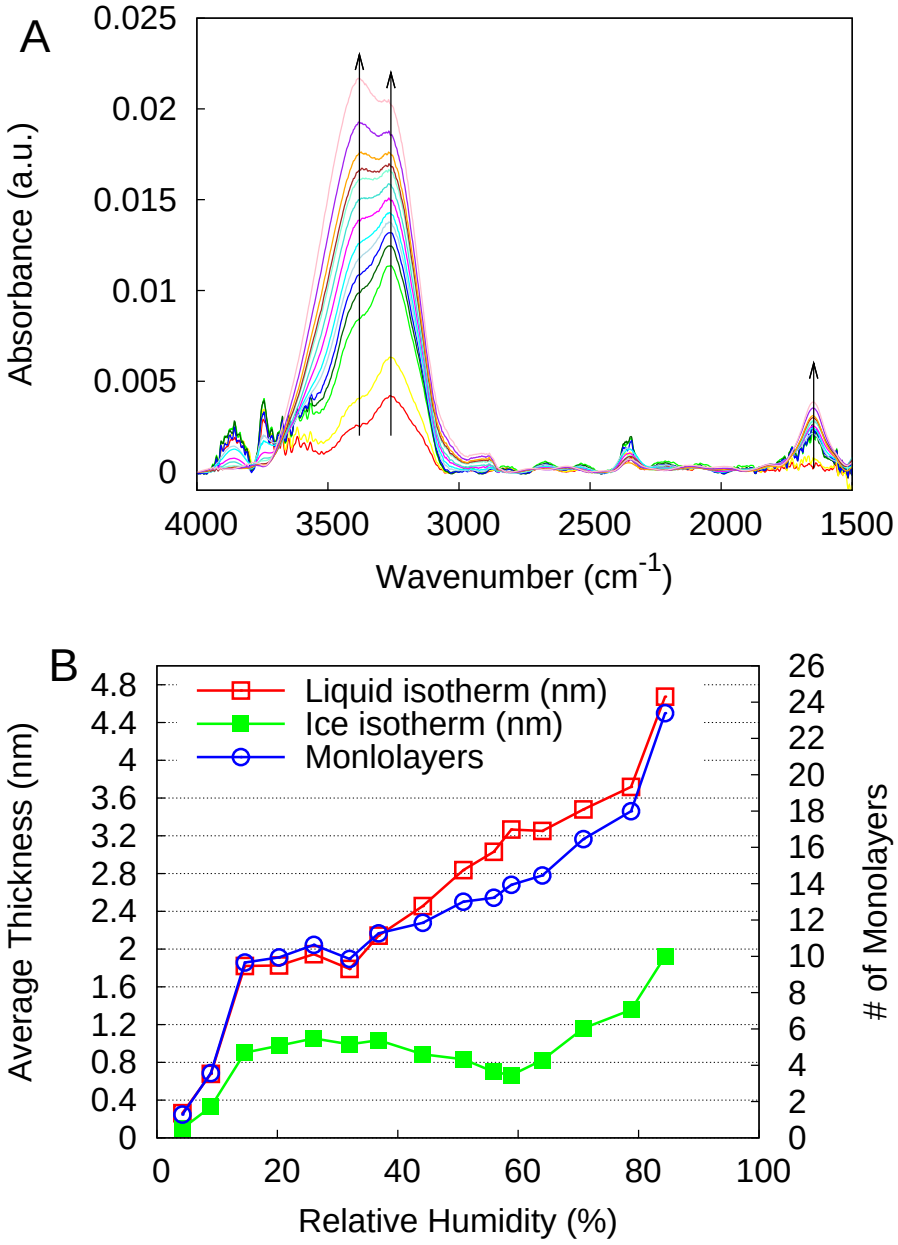

Figure 9.2: A) ATR-FTIR spectra of adsorbed water on the surface of a PEG-coated silicon ATR crystal at increasing relative humidities. The peak positions of ice-like and liquid water are marked with dotted lines 3260 cm^{-1} and 3380 cm^{-1}, respectively, and the position of the O-H bending mode is marked at 1635 cm^{-1}. Arrowheads denote the direction of increasing relative humidity. Spectra correspond to relative humidities of 4.2%, 9.0%, 14.6%, 20.3%, 26.1%, 32.0%, 36.8%, 44.2%, 50.9%, 56.0%, 58.9%, 64.0%, 70.8%, 78.8%, and 84.4%. B) Graphical representation of the structure and relative thickness of the adsorbed water layer as a function of relative humidity, as determined from infrared spectra.

alcohols and amines. In the previous work, Asay and Kim did note a small absorption at 3740 cm^{-1} and assigned this peak to stretching of a "free O-H," a hydroxyl group with no hydrogen bonds. The two peaks in question are likely related to a common chemical species given that their absorption values trend together throughout the course of the experiment. Given that there are no amine compounds present during the experiment, and the previous assignment of the absorption at 3740 cm^{-1} to O-H stretching, an assignment to O-H absorption modes is also made here. Regardless of the assignment of these two peaks, the spectral data clearly indicate that PEG-modified silicon surfaces are capable of supporting extensive adsorbed water layers, which is the key to their non-fouling properties [83, 84].

9.3.3 Silica layer treated silicon oxide

The vapor deposition of silica onto silicon results in the formation of a robust silica film that is 49.7±0.9 nm thick, as determined by ellipsometry on coated silicon substrates. An AFM micrograph of the silica film is shown in Figure 9.3. The RMS roughness value is 3.57 nm, which is consistent with previous results [54].

The results of water adsorption onto the surface of a silica-modified silicon ATR crystal are presented in Figure 9.4. The presence of the silica layer on the surface determines the depth of penetration of the evanescent wave, but the silica layer itself is considered impervious to liquid water. In order to determine the thickness of bulk water that the evanescent wave interacts with, the thickness of the silica layer is subtracted from the depth of penetration of the evanescent wave. For example, for the silicon/silica system, the depth of penetration is approximately 505 nm at a 45° angle of incidence. In this experiment, the silica layer is 49.7 nm thick. This means that the absorption measured for a bulk water sample on a silica film corresponds to 455.3 nm of water ($505 - 49.7$ nm). Even if the silica film is permeable to water, without considering any changes in refractive index of the silica layer, taking into account its thickness in this manner will result in *underestimation* of the thickness of the adsorbed water layer by this method.

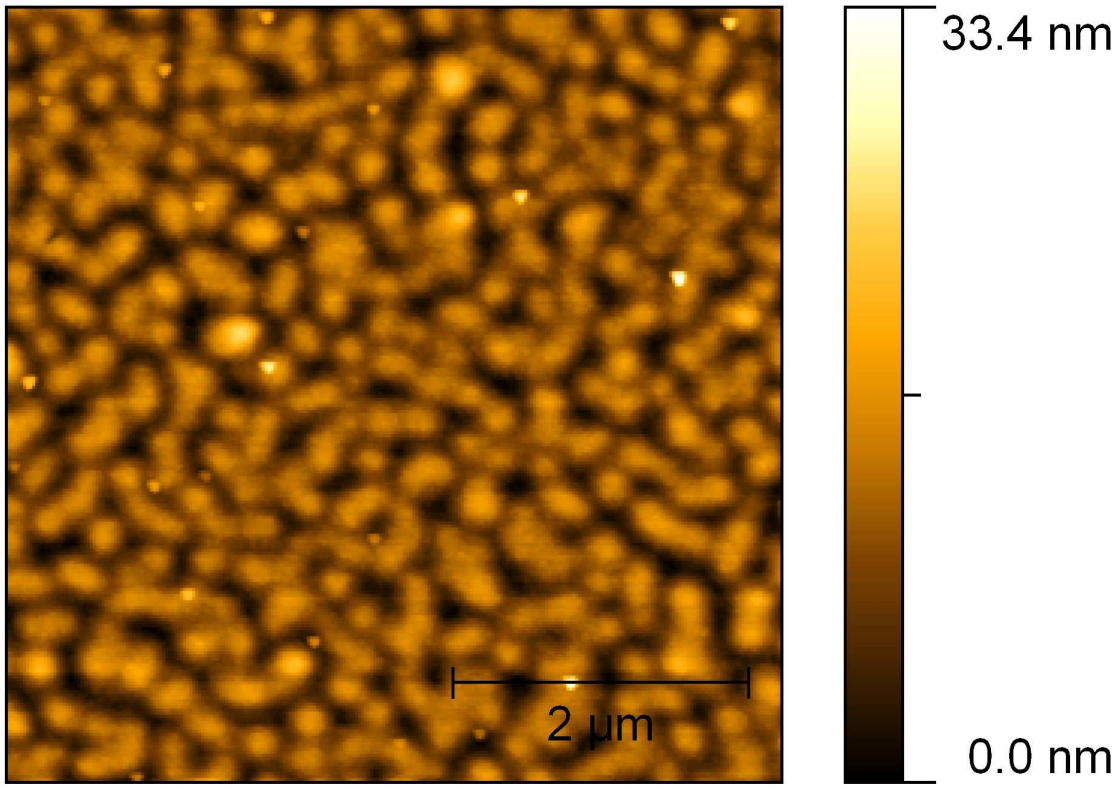

Figure 9.3: An atomic force micrograph of a silica film deposited on a silicon substrate.

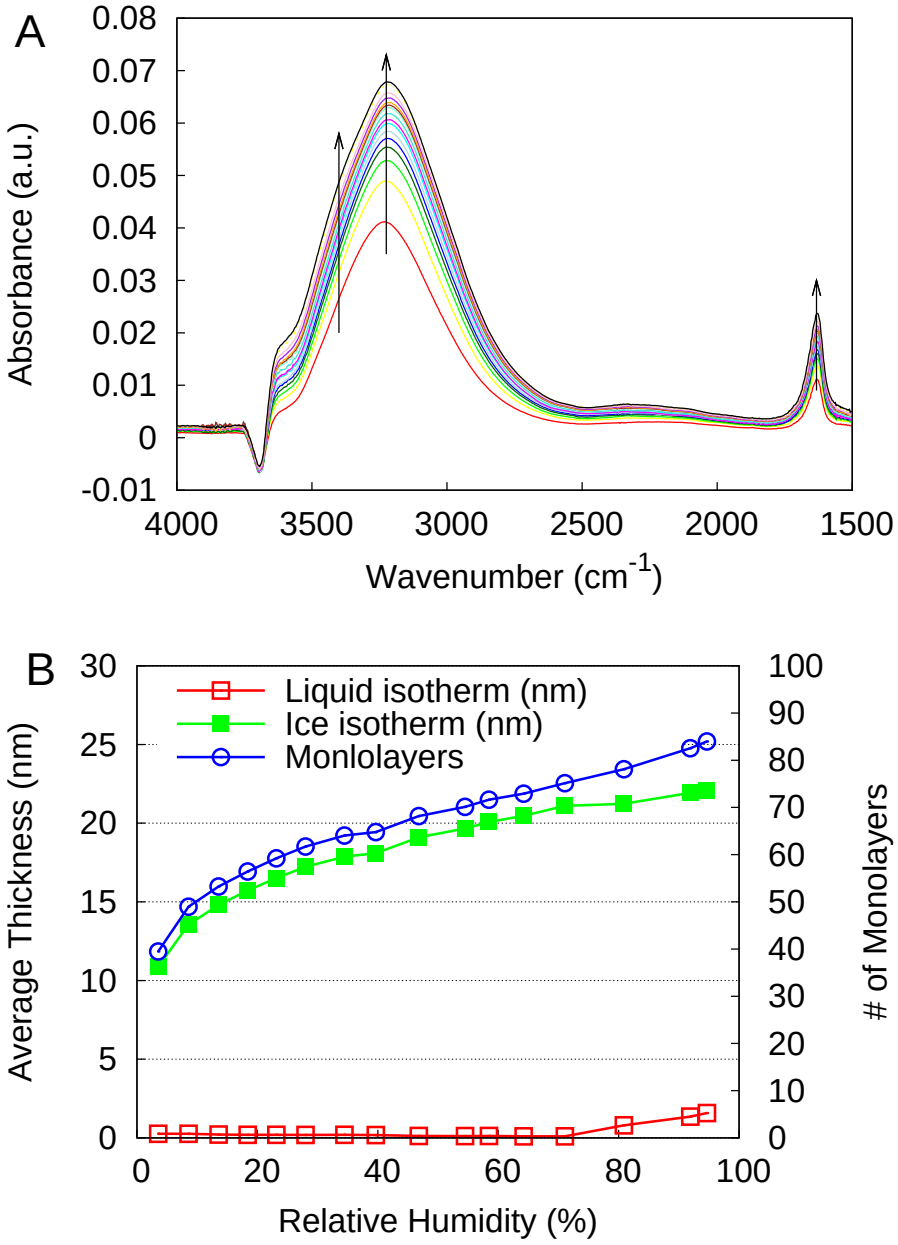

Figure 9.4: A) ATR-FTIR spectra of adsorbed water on the surface of a silica-coated silicon ATR crystal at increasing relative humidities. The peak positions of ice-like and liquid water are marked with dotted lines 3225 cm^{-1} and 3400 cm^{-1}, respectively, and the position of the O-H bending mode is marked at 1635 cm^{-1}. Arrowheads denote the direction of increasing relative humidity. Spectra correspond to relative humidities of 3.5%, 8.6%, 13.6%, 18.4%, 23.1%, 28.0%, 34.5%, 39.7%, 46.8%, 54.5%, 58.5%, 64.2%, 71.1%, 80.9%, 91.9%, and 94.7%. B) Graphical representation of the structure and relative thickness of the adsorbed water layer as a function of relative humidity, as determined from infrared spectra.

If we consider that the silica film is permeable by liquid water, and that the refractive index at the interface will be decreased due to the presence of water, which has a lower index than silica, the calculated penetration depth of the evanescent wave will be decreased, which will in turn decrease the calculated thickness of the adsorbed water layer. Let us consider, as a lower limit, a silica-water composite interface with a refractive index of 1.33 (pure water) and a penetration depth of 482 nm, which is most definitely an underestimate of the true depth of penetration. Carrying out the analysis in this manner results in thickness values for the adsorbed water layer that only differ from those reported in Figure 9.4 by 6%. In either case, determining the proper way to handle the presence of the silica film and its effect on the determination of the thicknes of a bulk water sample will only affect the determination of the *thickness* of the adsorbed water layer derived from the method. The relative *structure* of the adsorbed water layer (*i.e.* relative proportion of ice-like *vs.* liquid water) is not affected by the method of obtaining the bulk water thickness.

The data in Figure 9.4 show that the adsorbed water layer that exists on the silica-coated surface is dramatically different from that which exists on clean silicon oxide and on PEG-modified silicon oxide. First, the structure is dominated almost entirely by ice-like water. In fact, significant liquid water adsorption does not begin until relative humidities near 80% are encountered. Furthermore, the ice-like water structure has an absorption peak centered near 3225 cm^{-1}, which is 25 cm^{-1} lower than on clean silicon oxide and 35 cm^{-1} lower than on PEG-modified silicon oxide. This shift to lower energy indicates a stronger degree of hydrogen bonding with the silica-coated surface relative to the other surfaces studied. Near 90% RH, the amount of adsorbed water is equivalent to nearly 85 monolayers, which is nearly an order of magnitude greater than the amount of adsorbed water on the surface of native silicon oxide, and approximately 3.5 times greater than on the PEG-modified silicon surface, at similar relative humidities. Considering what is known about interfacial water structure and its relationship to protein resistance, the silica layer is an excellent candidate for a protein resistant surface given that it has an extensive adsorbed water layer (even more so than PEG) with a very high degree of strong hydrogen bonding.

9.4 Conclusions

ATR-FTIR is used to characterize the water structure that exists on clean silicon oxide, PEG-modified silicon oxide, and silica-coated silicon oxide surfaces. The data indicate that at high relative humidities, clean silicon oxide surfaces support an adsorbed water layer that is approximately 9 monolayers thick, which is in excellent agreement with previous data reported by other authors. It is possible that differences in the relative structure of the adsorbed water on clean silicon oxide surfaces relative to the previous study are due to surface charging effects resulting from exposure to oxygen plasma immediately prior to beginning adsorption studies. In fact, on PEG-modified surfaces, which receive no oxygen plasma treatment prior to adsorption studies, the behavior of liquid and ice-like adsorption isotherms match more closely with the previous results.

PEG-modified surfaces support the formation of a more extensive adsorbed water layer, the thickness of which is determined to be equivalent to 24 monolayers of water at 85% RH, which is 2.5 times greater than the amount of adsorbed water on the surface of native silicon oxide at the same relative humidity. This increase in water layer thickness can be understood by considering that PEG monolayers can support hydration at the surface as well as in the interior of the monolyer structure through hydrogen bonding with oxygen atoms that are in the molecular backbone.

Silica-coated surfaces support the most extensive water layer of all the surfaces studied, the thickness of which is determined to be equivalent to approximately 85 monolayers of adsorbed water. This is nearly an order of magnitude more water than is adsorbed on clean silicon surfaces, and approximately 3.5 times more water than is adsorbed on PEG-modified silicon surfaces at similar relative humidities. Furthermore, the structure of the adsorbed water layer is almost entirely ice-like, even up to relative humidities of 80%, and the degree of hydrogen bonding is stronger than on the other surfaces, as indicated by spectral data. Considering these results in light of the background information presented on the relationship between interfacial water structure and protein adsorption, it is expected

that silica coated surfaces will posess favorable protein resistant properties. The results of protein adsorption studies on the surfaces studied in the present work as well as on uncoated and silica-coated polymer substrates, will be presented elsewhere.

Chapter 10

Interaction with Biological Materials

10.1 Proteins

10.2 Background and Introduction

Recently, as scientists have investigated the application of conventional MEMS devices to biological systems, the exciting fields of bio-MEMS and microfluidics have emerged. Due to their small size, bio-MEMS and microfluidics devices offer the advantage of requiring only small sample and reagent volumes, in a potentially low-cost, integrated package. Although technology in this area is developing rapidly at the laboratory scale, commercialization of these technologies has been hindered by the inability of such devices to interact with biological systems in a non-immunogenic and stable manner [21]. In many cases, non-specific protein adsorption has been demonstrated to result in unwanted behavior and failure in bio-MEMS and microfluidics devices [22,23]. Since one of the early steps in the biological response to a surface is protein adsorption, controlling this critical step can result in the ability to tune the long term biological response to a surface, which could dramatically increase device efficacy [82].

It has become increasingly apparent that interfacial water structure has profound implications for protein adsorption. If a surface supports the formation of a tightly bound interfacial water layer, protein adsorption becomes energetically unfavorable since approaching protein molecules cannot displace strongly adsorbed water molecules. Many recent studies have hinted at the importance of the existence of a strongly hydrogen bonded interfacial water network when a protein resistant surface is desired [82–85, 96, 98]. Vogler explains that the origin of the formation of structured interfacial water layers lies with the ability of a surface to disrupt water self-association in favor of water-surface association [82, 85].

Evidence suggests that surface Lewis sites, regardless of their chemical nature [82, 85, 86], and when present in sufficient quantity, serve to disrupt water self-association, resulting in the formation of a collapsed, densified interfacial water structure. It is the existence of this strongly hydrogen bonded interfacial water network that is believed to be responsible for the protein resistant properties of some surfaces, including poly(ethylene glycol) (PEG) [83, 84, 96]. In fact, molecular dynamics simulations performed by Zheng *et al.* indicate that water diffusivity at an oligo(ethylene glycol) (OEG) SAM interface (high number of Lewis sites) is reduced by an order of magnitude compared to the one at an OH-SAM interface (low number of Lewis sites), providing theoretical evidence for the existence of a strongly hydrogen bonded water phase with reduced mobility at PEG interfaces [83].

Previously, we have reported on the deposition of highly hydroxylated silica layers from the room temperature, vapor phase hydrolysis of tetrachlorosilane [54]. Using ATR-FTIR spectroscopy, we have investigated and characterized the extent and structure of the adsorbed water layer that exists on the silica surface and compared it to that which exists on clean silicon oxide surfaces and on PEG-modified silicon surfaces, the latter of which are well-known, protein-resistant surfaces (manuscript in preparation). The results of that study reveal that the silica layer supports an extensive, very strongly hydrogen bonded adsorbed water layer. In fact, the silica layer adsorbs nearly an order of magnitude more water than clean silicon surfaces, and nearly 3.5 times more than PEG-modified surfaces. Furthermore, nearly all of the adsorbed water is in an ice-like form, even at relative humidities approaching saturation, and the strength of hydrogen bonding within the layer is stronger than on both clean silicon and PEG-modified surfaces [99]. We have also recently demonstrated that the same deposition process can be employed to deposit robust silica films on polymer substrates, such as poly-methylmethacrylate (PMMA) and polystyrene [89].

Given its ability to be easily deposited to a wide variety of materials, and the extent and structure of the adsorbed water layer it supports, we were motivated to study the ability of the silica layer to resist protein adsorption on a variety of surfaces. In this paper, we

report the results of complementary studies regarding the adsorption of fluorescently labeled proteins on a range of different surfaces, including clean silicon oxide, PEG-modified silicon oxide, silica-coated silicon oxide, poly-methylmethacrylate (PMMA), silica-coated PMMA, polystyrene, and silica-coated polystyrene.

10.3 Experimental

10.3.1 Materials

Silicon wafers, p-type, with (100) orientation were obtained from Ultrasil Corporation (Hayward, CA). Tetrachlorosilane was obtained from Gelest, Inc. (Morrisville, PA). Commercial grade polystyrene containers were obtained from Ernest F. Fullam, Inc. (Clifton Park, NY). 950 PMMA A3, a poly(methyl methacrylate) (PMMA) suspension, was obtained from Micro Chem (Newton, MA). Lysozyme (LYS) (from chicken egg white, L-6876) and fibrinogen (FIB) (F-8630) were purchased from Sigma-Aldrich (St. Louis, MO) and used without further purification. Bovine serum albumin (BSA) (BP1605, Biotech grade), sodium phosphate (mono and dibasic), sodium chloride, potassium chloride, toluene (ACS grade) and hexane (Optima grade) were purchased from Fisher Scientific (Fair Lawn, NJ). Alexafluor 568 carboxylic acid dye (succinimydyl ester functionalization) was purchased from Invitrogen Corporation(Carlsbad, CA). Deionized water (18 MΩ-cm) was obtained from a Millipore filtration system. Microcon centrifugal filter devices were purchased from Millipore Corporation (Bedford, MA). All chemicals were used as received unless otherwise noted.

10.3.2 Preparation of labeled protein conjugates

Sodium phosphate buffer solutions (0.1 M, pH=8.3) are prepared and passed through a 0.2 μm syringe filter to remove any crystals that may in turn affect the fluorescence. Protein solutions of 5mg/mL of BSA, FIB, and LYS, respectively, are then prepared in the sodium phosphate buffer solution. 1 mg of the AF 568 dye is dissolved in 100 μL anhydrous

DMSO and divided into 7.5 μL aliquots. To prepare conjugated proteins, each aliquot is added to 100 μL of the respective protein solutions, and the conjugation is allowed to proceed at room temperature for two hours. Additionally, the solutions are kept in the dark to prevent photobleaching of the dye. After conjugation, the unconjugated dye is separated from the protein conjugate using Microcon ultra-centrifugal filter devices with 3 kDa molecular weight cut off (MWCO) for the LYS conjugate and 30 kDa MWCO for BSA and FIB conjugates, respectively. The absorbance of the protein conjugates is measured at 280 nm and 578 nm, using a standard UV/Vis spectrophotometer (Ultraspec 2100 pro, Amersham Biosciences, Piscataway, NJ) to determine the degree of labeling. Conjugated proteins are stored at 4°C and used within one week of their preparation.

10.3.3 Preparation of surfaces

Clean silicon oxide

Pieces cut from a silicon wafer (8mm $\times$ 8mm) are first sonicated in acetone and isopropanol for 10 minutes each and then dried under a stream of nitrogen. Then the samples are cleaned by an iterative HF etch/oxygen plasma process, which is described in detail elsewhere [53, 54]. This iterative cleaning method is repeated until inspection by contact angle and AFM indicate that a clean (contact angle $< 5°$), flat (RMS roughness $\sim$0.2 nm) surface has been obtained, but usually two iterations suffice.

Polymer films

The polymer films are produced by spin coating processes. For PMMA films on silicon substrates, a silicon wafer is spun at 1700 rpm for 45 seconds on a spin-coater. After spin coating, the PMMA film is soft-baked for 30 minutes at 170°C. The resultant PMMA film is 130 ± 0.2 nm thick, has a refractive index of 1.484, which is in excellent agreement with the manufacturer's specification of 1.488, and the contact angle is 63° [89]. Samples for further experimentation are cut from the silicon wafer using a diamond scribe.

For polystyrene films a method similar to one reported on by Stange *et al.* is employed, with slight modification [71]. A spin-coating solution of 1.5%(w/w) polystyrene in toluene is prepared by dissolving 1.3 g of commercial grade polystyrene in 100 mL of toluene. After the polystyrene is completely dissolved, the solution is filtered through a 0.5 μm filter to ensure that it is free of particles. Spin coating on a silicon wafer is carried out at 2500 rpm for 30 seconds. After spin-coating, the polystyrene film is baked at 75°C for 4 hours. The resultant polystyrene film is 92 ± 1 nm thick, has a refractive index of 1.583, which is in excellent agreement with published data [73]. The contact angle is 87° [89]. Samples for further experimentation are cut from the silicon wafer using a diamond scribe.

Silica layer deposition

The deposition of silica layers from the room temperature, vapor phase hydrolysis of tetrachlorosilane has been described in detail elsewhere [54, 64]. A custom built vapor deposition system is employed for depositing the silica films onto clean silicon and onto polymer-coated silicon substrates, simultaneously. A schematic of the vapor deposition system is available in Figure 4.3, and a photograph is available in Figure 4.8. Immediately prior to deposition, the polymer surfaces are activated with a brief, RF oxygen plasma (10W, 250 mTorr, 30 sec). The oxygen plasma is employed to promote good adhesion between the polymer surface and the silica film, but it is not required to achieve silica deposition [54]. In this work, each silica deposition process is accomplished by dosing 20 Torr each of tetrachlorosilane and DI water into the deposition chamber (unless otherwise noted), and the reaction is allowed to proceed for 10 minutes. Detailed instructions are available in reference [64]. Silica-coated samples are prepared within hours before they are used in protein adsorption experiments. Contact angles of less than 6° are indicative of the extremely hydrophilic nature of the silica layer as deposited onto silicon and polymer substrates [89].

10.3.4 Protein adsorption experiments

For protein adsorption experiments, 10 μL of conjugated protein solutions are placed on the surface of appropriately processed samples. The sample surfaces are then covered with a clean glass coverslip (18 mm $\times$ 18 mm) in order to achieve equal wetting. Samples are left in this condition for 30 minutes in a dark environment, and then they are rinsed in copious amounts of PBS (10 mM, pH 7.4) and DI water, in that order, and dried under a stream of air. As a control experiment, non-specific adsorption of dye molecules is monitored by placing 10 μL of unconjugated dye solution onto sample surfaces and proceeding as previously described. This control is included in the experiment to help to ensure that fluorescence observed from conjugated proteins is due primarily to surface-protein interactions as opposed to surface-dye interactions.

10.3.5 Fluorescence microscopy

Fluorescence measurements for protein adsorption studies are performed using an Olympus BX 41 microscope in epifluorescence mode. An excitation filter with a wavelength of 581 nm is used to filter light from X-cite lamp source (series 120). The resulting fluorescence from the sample is passed through an emission filter (596 nm) and imaging is accomplished using an Optronics MicroFire camera. The samples are viewed and images captured for analysis using the manufacturer's software (Optronics PictureFrame 2.0). Each image is recorded at a 5s exposure time. Color intensity data is extracted from still fluorescence microscope images by utilizing the "Measure RGB" plug-in in ImageJ software, which is a free image analysis software provided by the National Institute of Health. Intensity values reported herein are the measured value from the red color channel of each image, as computed in ImageJ.

10.4 Results and Discussion

Adsorption of proteins to surfaces is generally non-specific in nature, the process being influenced by interactions that may be electrostatic, hydrophobic, or those due to van der Waals forces. Therefore, protein-surface interactions can vary greatly from one surface to another, which may be attributed to the relative charge and relative hydrophilicity of the surfaces. The proteins chosen in this study are lysozyme, BSA, and fibrinogen, as they represent a range of isoelectric points (PI) and molecular weights. Lysozyme, which is an arginine-rich, cationic protein with a PI of 11.35, has approximate dimensions of 4.6 nm x 3 nm and a molecular weight of 14.5 kDa [100, 101]. Given its relatively high PI, electrostatic interactions primarily govern its adsorption onto various surfaces. BSA, which is a carrier protein found commonly in blood, is a slightly larger globular protein, with approximate dimensions of 8 nm x 3.8 nm. It's PI is 4.85, and its molecular weight is 66.5 kDa [100]. Both lysozyme and BSA have a high degree of α-helical structure in their native forms. Fibrinogen on the other hand, is a rod-shaped protein comprised of a central domain similar to albumin and dilobed distal domains of dimensions 10 nm x 6 nm. The total length of fibrinogen is 45 nm [102], its molecular weight is 340 kDa, and it has a PI of 5.50 [100]. Fibrinogen is structurally similar to fibronectin, which is an adhesive protein, and it interacts well with surfaces that may be hydrophilic, charged, or hydrophobic. Both BSA and fibrinogen are negatively charged at neutral pH and may thus interact well with cationic surfaces.

The first part of this study is related to characterizing protein adsorption on similar surfaces to those on which the water structure has been characterized by ATR-FTIR [99]. The surfaces involved are clean silicon, PEG-modified silicon, silica layer treated silicon, and a polystyrene coated silicon surface is included as a fouling control [98]. In order to determine if the nanostructure of the silica layer has an impact on its protein adsorption properties, two different silica layer surfaces are produced by two different deposition recipes, and the surfaces are designated as S-Si(20) and S-Si(15). The extracted fluorescence intensity data

for fluorescence images captured after the protein adsorption experiments are available in Figure 10.1. For each protein under study, the fluorescence intensity data are normalized to the fluorescence intensity observed on the polystyrene surface.

The first and most obvious difference between the surfaces under study here is that the only surface that fouls significantly is the polystyrene surface, which is introduced into this experiment as a fouling control. As expected, PEG-modified surfaces exhibit exceptionally low fouling for all proteins under study, but so do clean silicon surfaces. The fact that silicon surfaces do not exhibit appreciable fouling in this study is, at first glance, surprising. Silicon surfaces have been shown to be susceptible to fouling by BSA [88], and they are well-known to foul at physiological pH [21]. However, the previous results describe fouling of silicon surfaces over longer timeframes than those under study here, which may help to explain the low-fouling result in this case.

The S-Si(20) surface displays low fouling toward BSA, with performance nearly identical to clean silicon and PEG-modified silicon surfaces. However, it does not perform as well for FIB and LYS, as indicated by increased fluorescence intensity in these cases. On the other hand, the S-Si(15) surface has low fouling toward all three proteins, although performance is still best for BSA. In fact, for BSA, the fluorescence intensity for the S-Si(15) surface is slightly lower than for the PEG surface. For FIB and LYS, the results for the S-Si(15) surface are not quite as good as for PEG, indicated by an increase in fluorescence intensity by a factor of approximately 2.2-2.4 relative to PEG surfaces, but they still represent significant decreases in fouling relative to the polystyrene surface.

Although the silica layer supports a water structure that is even more extensive and more strongly hydrogen bonded than that which exists on PEG surfaces [99], the non-fouling performance of PEG is still slightly better. One possible explanation for this observance could be due to electrostatic effects. The native silicon oxide surface is known to possess a negative charge at physiological pH due to deprotonation of surface silanol groups [21]. Since the silica layer is believed to possess an increased concentration of silanol groups relative to traditional silica materials [54], it is conceivable that the surface possesses an

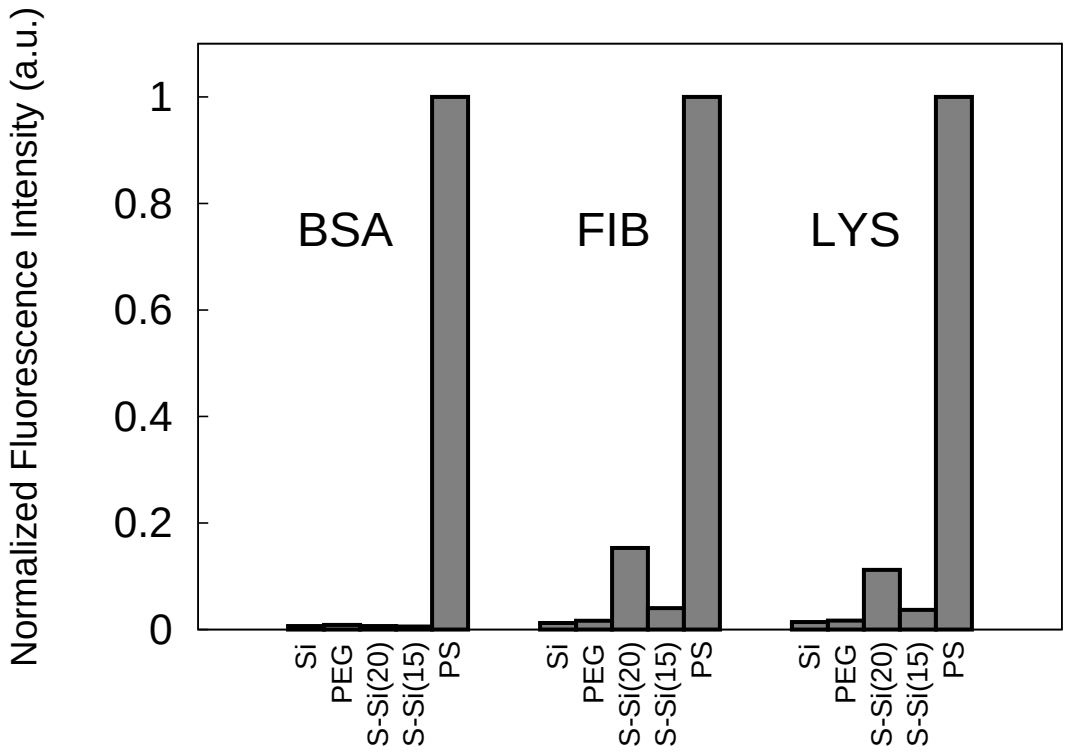

Figure 10.1: Fluorescence intensity data extracted from fluorescence microscope images after protein adsorption. The surface naming convention is as follows: silicon (Si), silica layer on silicon (S-Si, the number designates the pressure of tetrachlorosilane in the deposition recipe), PEG on silicon (PEG), polystyrene on silicon (PS).

increased negative charge relative to traditional silica materials under similar conditions. This may help to explain why the non-fouling results are best for the silica layer for BSA, which is the most negatively charged protein in this experiment, and not quite so good for FIB and LYS, which are less negatively charged and positively charged, respectively.

Non-specific adsorption of unconjugated dye is only observed on the polystyrene surface, and is most likely due to hydrophobic interactions between the dye molecules and the polystyrene surface (data not shown). Fluorescence intensity observed for conjugated proteins on polystyrene surfaces is 3-4 times higher than the fluorescence intensity observed with unconjugated dye molecules in control experiments, even though the concentration of the dye present in the control experiment is much higher than its equivalent concentration in the protein conjugates. The concentration of unconjugated dye in control experiments is approximately 10, 2.5, and 4 times higher than the equivalent concentration in BSA, FIB, and LYS conjugates, respectively. This indicates that the surface-protein interaction dominates the surface-dye interaction, and that fluorescence intensity values indicated in Figure 10.1 are due primarily to adsorption of protein, not of dye.

For fibrinogen and lysozyme, fluorescence intensity is 73.7% and 67.1% lower on the S-Si(15) surface than it is on S-Si(20), respectively. It has been shown previously that both the thickness and surface morphology of the silica film are highly dependent on the deposition recipe [54]. In this case, the S-Si(20) surface is approximately 41 nm thick with an RMS roughness of 3.55 nm, and the S-Si(15) surface is approximately 19 nm thick with an RMS roughness of 2.88 nm. AFM micrographs of these surfaces are available in Figure 10.2. The micrographs clearly show that the topography of these films is significantly different. Although the S-Si(20) film has a higher RMS roughness value than the S-Si(15) film, its nanotopographical features are not well-defined. There is a nanostructure visible in the 20μm $\times$ 20μm scan in Figure 10.2A, but it is hard to distinguish in the 5μm $\times$ 5μm inset scan. On the other hand, the S-Si(15) film has a remarkably well-defined nanostructure, being comprised of many small particulate-like features. The inset in Figure 10.2A is shown so that a direct comparison of the nanostructure on the same size scale can be

made between the two surfaces, and it is clear that they are very different. It has been recently demonstrated that surface topography (and specifically, surface curvature) at the nanoscale has a definite impact on protein adsorption [103]. In fact, Roach *et al.* noted an inverse relationship between the surface curvature and the saturation amount of adsorbed fibrinogen on silica spheres. Since the S-Si(15) surface is comprised of much smaller particles than the S-Si(20) surface, the S-Si(15) surface should have higher curvature. With that understanding, the results here are in agreement with the previous study of Roach *et al.*, and the difference in the non-fouling properties observed between the two silica films can be understood in terms of their differing nanotopgraphy.

The second part of this study involves characterizing protein adsorption on unmodified and silica layer treated polymer surfaces. The surfaces involved are polystyrene, silica layer treated polystyrene, PMMA, and silica layer treated PMMA. Detailed descriptions of the silica layer modified polymer surfaces are available elsewhere [89]. Control experiments are performed with unconjugated dye, and PEG-modified silicon samples are also included for comparison purposes. Fluorescence intensity data is extracted from images captured after the protein adsorption experiments, and values are normalized against the fluorescence intensity observed on polystyrene surfaces for each protein under study. The normalized fluorescence intensity data are shown in Figure 10.3.

Values for the reduction of protein adsorption are calculated by Equation 1. In Equation 1, I_U represents the intensity value recorded from protein adsorption on an unmodified polymer surface, and I_S represents the intensity value recorded from protein adsorption on a silica-coated polymer surface.

$$\% \text{ Reduction} = \frac{(I_U - I_S)_{protein} - (I_U - I_S)_{dye}}{(I_U - I_S)_{protein}} \tag{10.1}$$

The fluorescence microscope images are shown in Figure 10.4, and resulting values for percent reduction are shown in Table 10.1.

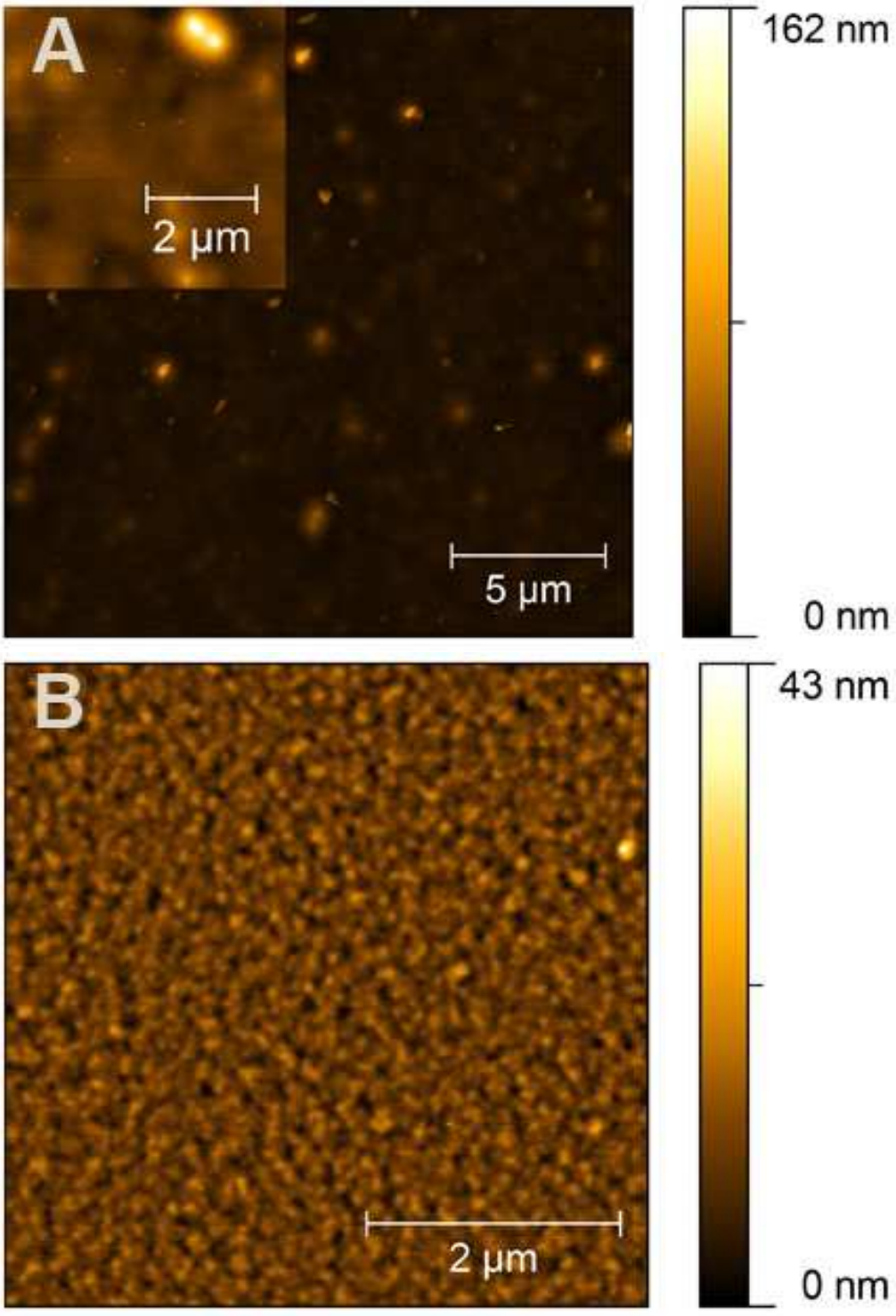

Figure 10.2: AFM micrographs of the A) S-Si(20) and B) S-Si(15) surfaces. The image in A is a 20μm $\times$ 20μm scan with a 5μm $\times$ 5μm inset, and the image in B is a 5μm $\times$ 5μm scan.

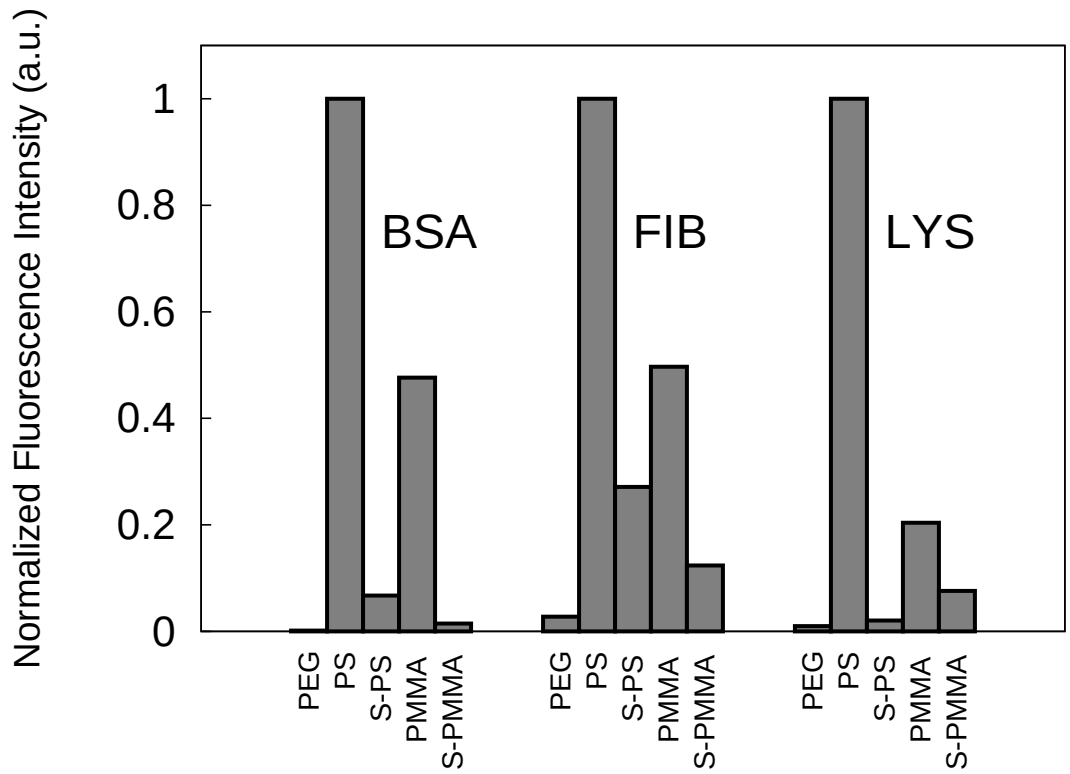

Figure 10.3: Fluorescence intensity data extracted from fluorescence microscope images after protein adsorption. The surface naming convention is as follows: PEG on silicon (PEG), polystyrene on silicon (PS), silica on polystyrene (S-PS), PMMA on silicon (PMMA), and silica on PMMA (S-PMMA).

Table 10.1: Percent reduction of protein adsorption on silica-coated polymer surfaces relative to bare polymer surfaces.

	% Reduction		
Surface	BSA	FIB	LYS
S-PS	95.9	92.7	97.6
S-PMMA	126.2	144.7	164.8

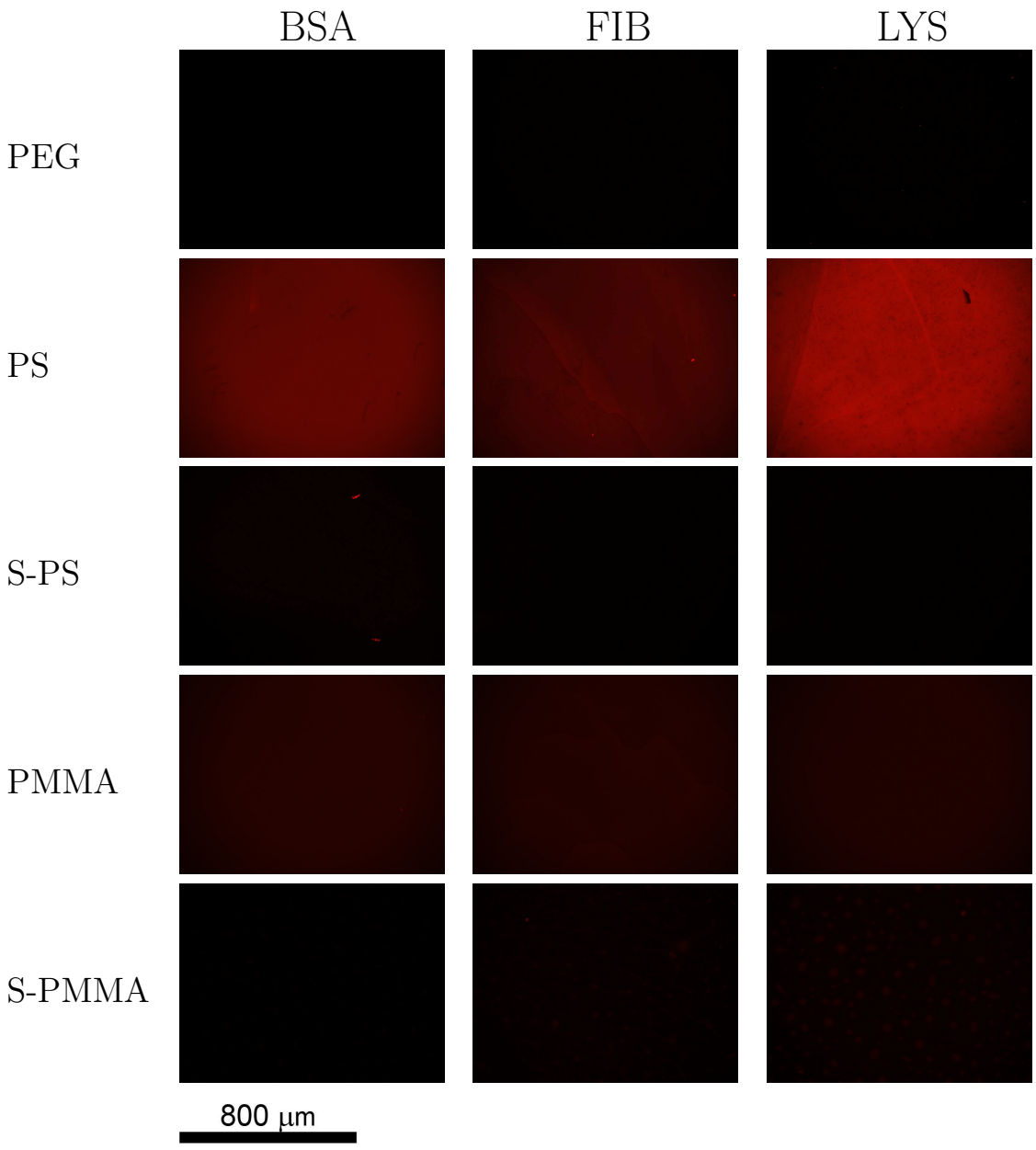

Figure 10.4: Fluorescence microscope images of respective surfaces after exposure to labeled protein solutions for 30 minutes. A red color indicates adsorption of protein to the surfaces. The surfaces shown are as follows: PEG on silicon (PEG), polystyrene on silicon (PS), silica on polystyrene (S-PS), PMMA on silicon (PMMA), and silica on PMMA (S-PMMA).

Figures 10.3 and 10.4 show that unmodified polymer substrates display appreciable fouling, the worst case being polystyrene, the most hydrophobic surface under study. In every case, silica modified polymer substrates have much lower fouling than unmodified polymers, with performance approaching that of PEG in some cases. For polystyrene surfaces, the presence of the silica layer contributes to significant reductions in protein adsorption relative to bare polymer surfaces, with reductions of greater than 90% for each of the proteins. The resistance to protein adsorption is still best for BSA although the S-PS surface performs exceptionally well against LYS adsorption. For PMMA, data for percent reduction are influenced by a non-specific interaction of the dye molecules with the S-PMMA surface. Except in the case of the S-PMMA surface, the control experiments with unconjugated dye indicate a low non-specific interaction between dye molecules and the surfaces under study. For the S-PMMA surface, however, there is a significant interaction of the surface with dye molecules, which contributes to percent reduction values greater than 100% in Table 10.1. Fluorescence microscope images for unconjugated dye adsorption on S-PMMA and S-PS surfaces are shown in Figure 10.5, and the images demonstrate the much greater affinity of unconjugated dye molecules to the S-PMMA surface.

The pattern of the fluorescence observed for the images in Figure 10.5B is very similar to what is observed for conjugated proteins on the S-PMMA surface (Figure 10.4), although it is most clearly visible for the unconjugated dye. Clearly the dye molecules have a non-specific affinity to the S-PMMA surface, and since the pattern of the fluorescence observed for conjugated proteins on the S-PMMA surface is the same as that observed for the unconjugated dye, it is possible that some fluorescence intensity observed for conjugated proteins on S-PMMA surfaces is due to non-specific interaction of the conjugated dye. If this is the case, it may mean that the adsorption observed for these proteins is greater than what would have been observed for the unconjugated proteins in their native state. It is puzzling that the same behavior is not observed for conjugated BSA on the S-PMMA surface, and it is also not observed for any species on other silica coated polymer substrates. We cannot at this time explain this observation.

That there is patterning in these fluorescence microscope images is also an interesting observation. The fluorescent regions in the micrographs for these surfaces may mimic the topography of the silica layer itself, with the fouling occurring at the peaks of silica particles, and non-fouling regions existing in the valleys. This very curious behavior could possibly be due to differences in the local radii of curvature on the peaks and in the valleys of these surfaces, respectively, which may impact on local adsorbed water layer structure. Further studies are underway to try and understand this phenomenon.

Although the results show that the protein resistant properties of the silica layer are good, its performance is not as exceptional as PEG in many cases. However, when compared to PEG coatings, the silica layer does have some strengths which may help to compensate for its slightly lesser protein resistant properties. For instance, it has been shown that PEG autoxidizes rapidly in the presence of oxygen and transition metal ions, which are both commonly found in biochemically relevant fluids [104]. Furthermore, *in-vivo*, the hydroxide groups of PEG are enzymatically converted to aldehydes and acids, which may eventually lead to unwanted cell attachment [104]. These previous results indicate that PEG may, due to chemical instability, lose its desirable non-fouling characteristic after prolonged exposure to biochemical/biological fluids, which is a potentially significant drawback and limits the usefulness of PEG-based coatings in long-term applications. On the other hand, our previous results with the silica layer indicate that it possesses excellent stability in aqueous environments, and since it is inorganic, it is not expected to be susceptible to enzymatic reactions. Furthermore, we have recently demonstrated the silica film can be easily deposited onto a wide variety of substrates, including PDMS, PMMA, and polystyrene, and since the deposition is a vapor-phase process, processing on three-dimensional objects with large aspect ratios, such as sealed microfluidics devices, is also possible.

10.5 Conclusions

The adsorption of fluorescently labeled BSA, lysozyme, and fibrinogen on a variety of surfaces are studied in order to determine the non-fouling performance of a highly hydroxylated silica film. The presence of an extensive adsorbed water layer on the silica layer surfaces yields comparable protein non-fouling behavior to that of PEGylated surfaces in many cases, especially against BSA. However, the resistant properties of the silica layer are slightly less favorable against FIB and LYS adsorption, suggesting the existence of electrostatic effects. This suggests that although adsorbed water structure is critically important in determining non-fouling behavior, other factors must also be considered when engineering non-fouling surfaces. Even so, the silica layer does afford a substantial reduction in adsorption of BSA, FIB, and LYS relative to unmodified polymer surfaces. This is an important result given that modification of polystyrene and PMMA surfaces with PEG may not be easy, but the deposition of silica layers to these substrates is a straightforward and workable solution if protein resistance is desired for these materials.

Another interesting characteristic of the silica layer is the ability to easily tailor its nanotopography by changing the deposition recipe. The results in this study suggest that the non-fouling properties of the silica film may be tuned by changing its nanotopography, which is a very interesting and potentially powerful finding. Further studies are planned in order to establish the link between the nanotopography of the silica layer and its protein resistant properties.

10.6 Bacterial Cells

10.6.1 Background and Motivation

This portion of the work is prompted not only by the nature of the application, since biological agents are commonly encountered in microfluidics applications, but also by some strange experimental observations. When initially performing the aqueous immersion experiments like those described in section 6.2.6, the samples were stored in DI water at

room temperature. However, at this temperature, bacterial contamination became problematic, and confounded the experiments. Interestingly, samples that received the silica layer treatment before modification with hydrophobic organosilane precursors seemed to resist bacterial adhesion, as evidenced by an apparent lower number density of cells on the surface (I say apparent, because controlled measurements were not made). Optical micrographs are shown in figure 10.6. Investigation by AFM confirmed that the particles are bacterial cells (see figure 10.7).

10.6.2 Experimental

In order to further investigate this phenomenon, a silica layer is deposited onto a silicon wafer in a defined pattern, which is created on the silicon wafer by a photolithographic process, in order to see if cells will respond differently to the areas that have received silica layer treatment. After silica deposition, the photoresist is stripped by pirhana treatment, leaving behind domains of the vapor deposited silica layer on the surface of the silicon substrate. After pirhana treatment, surface patterns are no longer visible to the eye, as depicted in Figure 10.8. After pirhana treatment, the surface is functionalized with OTS to recreate the hydrophobic surface chemistry encountered in Figure 10.6. This results in a surface that is hydrophobic, but that also has domains of different nanotopography as a result of the presence of the silica layer. The sample is incubated for 24 hours at 37°C in 10 mL of a bacterial cell solution (2.7 x 10^7 *E. coli* 0157:H7 cells/mL in PBS). After incubation, samples are rinsed in copious PBS and dried under a stream of nitrogen. Then the sample is exposed to the vapors of osmium tetroxide for $\geq$1 hour to fix the cells, and then it is sputtered with gold to prepare it for SEM imaging.

10.6.3 Results and Discussion

SEM images of the surface after incubation in bacterial cell solution for 24 hours are displayed in Figure 10.9. The image on the left in Figure 10.9 clearly shows the photolithographic pattern on the silicon substrate. The visibility of the pattern is due to fouling of

the surface as a result of incubation in the bacterial solution. Octagonal areas are silica layer treated while the rest of the surface is not. Clearly, the portions of the surface that have not received the silica layer treatment are fouled to a much higher degree than the portions of the surface that are silica layer treated. The image on the right is a close-up of a cluster of what are believed to be cells on the surface. The shape is unexpected for *E. coli* 0157:H7, since it is a rod-shaped bacteria. It is possible that, given the hydrophobic nature of the surface, the cell shape is abnormal due to denaturation of cellular surface proteins. The denaturation of proteins on hydrophobic surfaces is a well-documented phenomenon.

In order to test the effect of surface hydrophobicity on cellular shape, the experiment was repeated, but this time without the OTS functionalization after pirhana treatment. In this case, *E. coli* 0157:H7 cell alignment was observed along the interface of silica layer/no silica layer regions, and cells seemed to prefer the region lacking the silica layer treatment. An example SEM image is shown in figure 10.10.

10.6.4 Conclusions

It seems that the presence of the silica layer does have an impact on the behavior of cells at treated surfaces, but these are only preliminary results. At this time it is unknown whether or not cells sense the nanotopographical features of the silica layer surface, or if the nanotopography of the surface perhaps causes a change in protein adsorption, which would in turn affect cellular interactions. Or perhaps the behavior is not related to nanotopography at all, but to some other presently unknown property. More study is needed to determine the effect of the silica layer on bacterial cell adhesion and migration, and whether it is chemical or physical in nature.

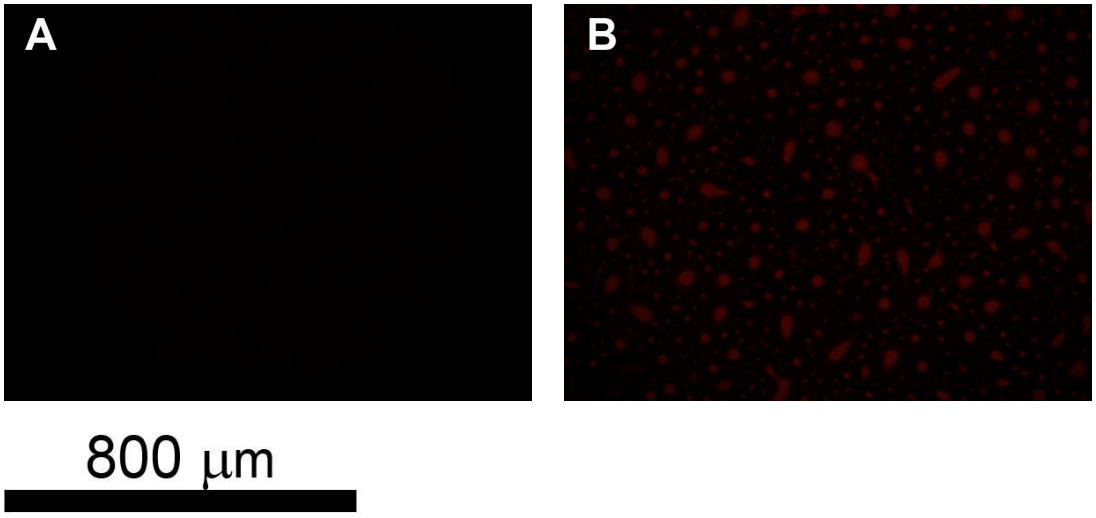

Figure 10.5: Fluorescence microscope images of unconjugated dye adsorption on A) S-PS and B) S-PMMA surfaces.

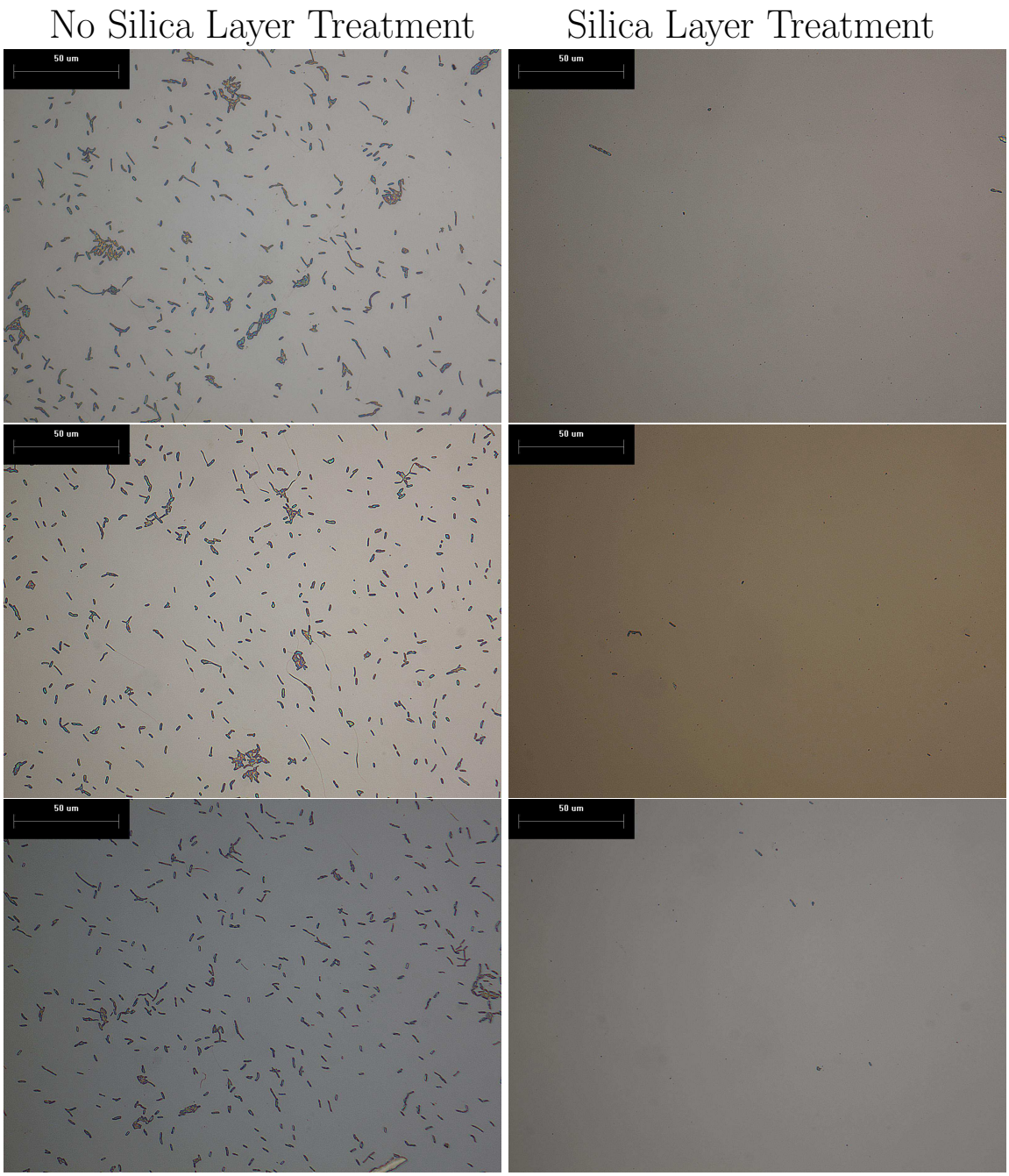

Figure 10.6: Pictured here are optical micrographs of an unknown bacteria on silicon surfaces treated with (row 1) octyltrichlorosilane, (row 2) octyltrimethoxysilane, and (row 3) octadecyltrichlorosilane.

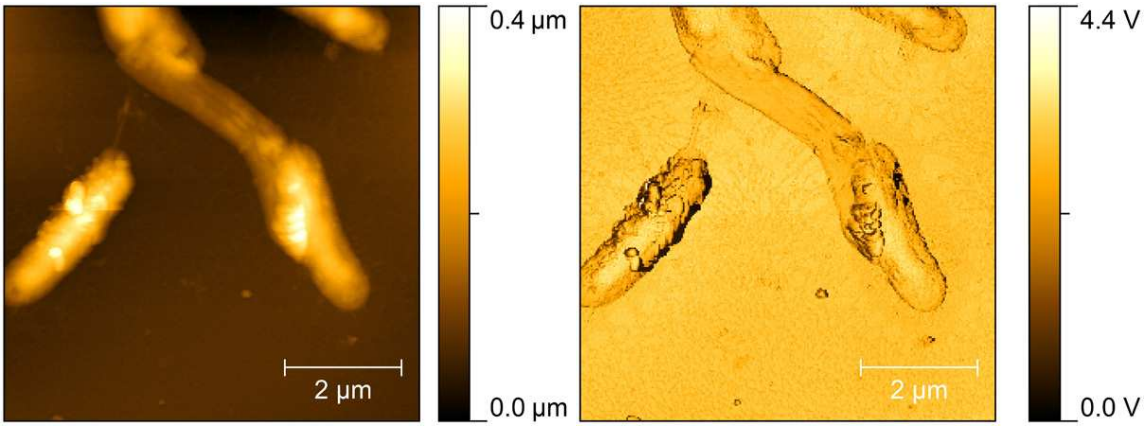

Figure 10.7: These are height (left) and phase (right) images of bacterial cells on hydrophobic silicon surfaces.

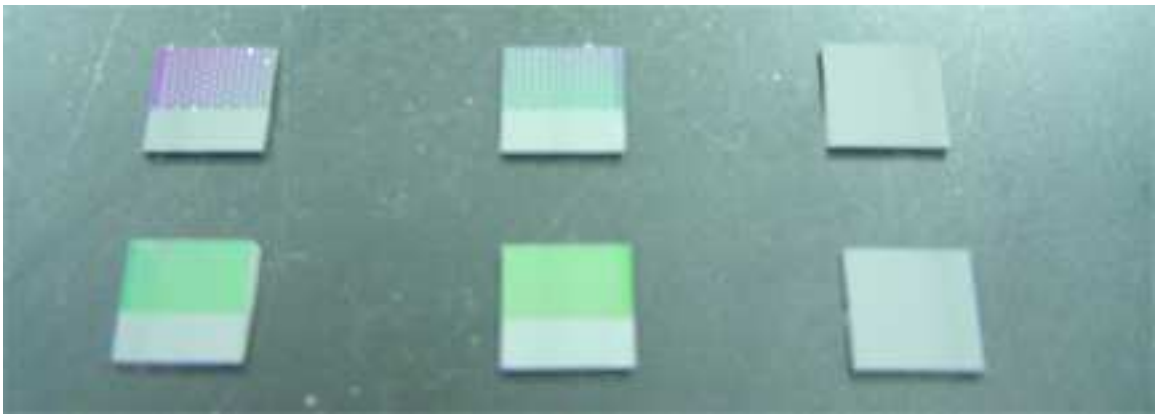

Figure 10.8: This image depicts the sample after each step in the preparation process, beginning with the photolithographically patterned substrate, then after silica deposition, and then after pirhana treatment. Notice that after pirhana treatment, patterns on the substrate are no longer visible.

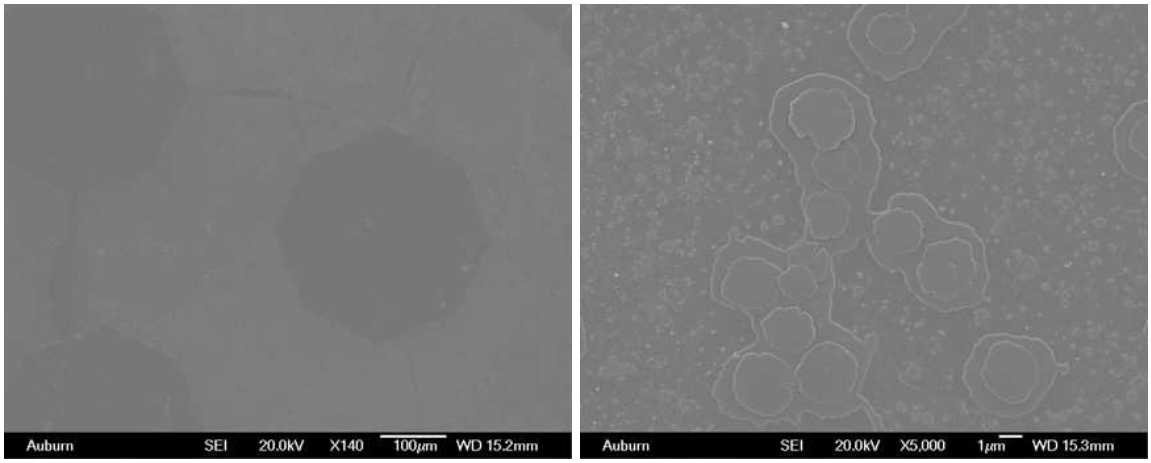

Figure 10.9: The SEM micrograph on the left indicates the patterned deposition of the silica layer on the silicon substrate. Octagonal areas are silica layer treated while the rest of the surface is not. Fouling is substantially greater on the areas that are not coated with the silica layer. The image on the right is a close up image of some cells on the surface of a non-treated area. The cell shape is not as expected for *E. coli* 0157:H7.

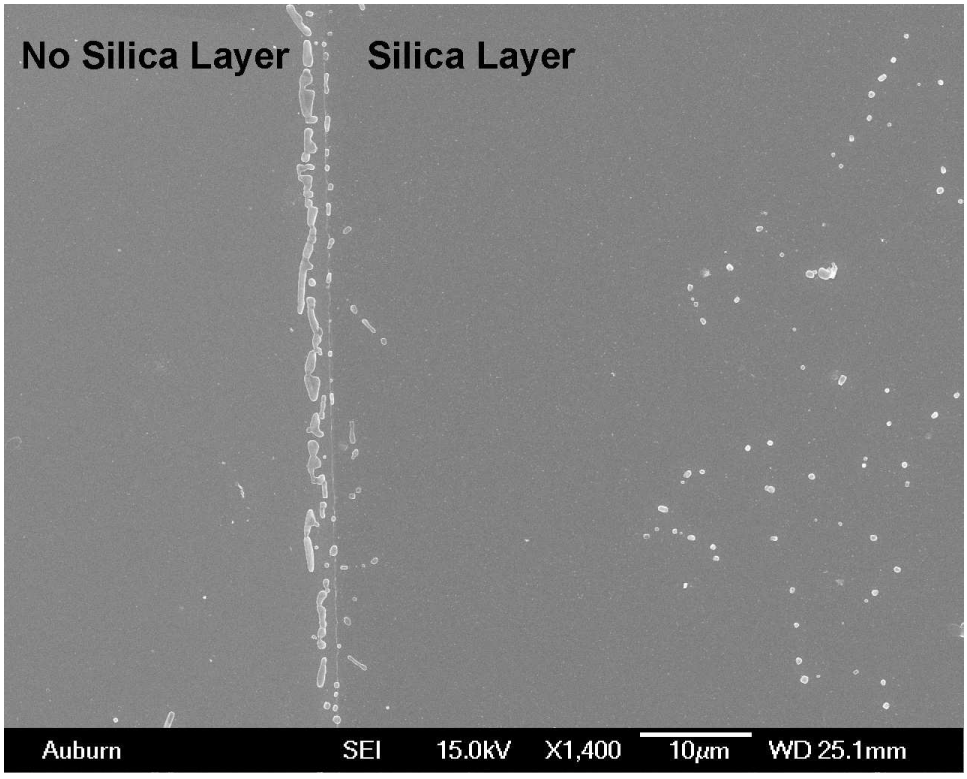

Figure 10.10: This SEM micrograph indicates cell alignment along the interface of silica layer/no silica layer regions. The small particles on the seed region are residual salt crystals from the buffer solution.

Chapter 11

Engineering New Molecular Precursors–A Case Study for Aminated Surfaces Formed from Aminopropyltrimethoxysilane

One of the latest technological needs for aminated surfaces involves their use as intermediate linker-layers in the bioassay and Bio-labchips markets. Uses of amine terminated surfaces from APTMS include immobilization of proteins, enzymes, antibodies, and DNA [8–10] and also inorganic nanoparticles [10,12], as a coupling agent in composites, glass fibers, and adhesive joints [8], chromatographic stationary phases [8, 25, 26], and chemical sensors [10, 25, 26]. In fact, it has been reported that short chain aminosilanes are among the most extensively studied [biochemical] coupling agents [105].

Many research laboratories have studied and used aminopropyltrimethoxysilane as an aminating precursor for years. This precursor is very widely used in the bio-tech area, and a significant market demand is present for pre-aminated surfaces. The number of commercial producers of amine-terminated glass slides has recently arisen in response to this growing need, but there have been a number of difficulties in the technological development of viable low temperature methods that we seek to address.

11.1 Difficulties with Aminopropyltrimethoxysilane

Historically, aminopropyltrimethoxysilane has been deposited from solution-based, or wet chemistry methods [106]. However, the liquid phase deposition is a highly variable process and depends on many factors, including the skill of the operator doing the synthesis. Other process variables, including solvent choice, temperature, deposition time, use of catalysts, solvent pH, annealing method (thermal or in air) and temperature, amount of surface-bound water, and the amount of dissolved water present in the solution phase, are

all shown to have significant effects on the resulting film density, morphology, and homogeneity [8].

It is also common to observe the formation of multilayers of APTMS [8]. In fact, layers up to 100 Å thick during 72 hours of deposition have been observed [1]. Caravajal, *et al.* employed ^{29}Si and ^{13}C NMR to study the effect of the amount of surface-bound water and the post-coating curing temperature on the amount of siloxane attachments and on the amount of unreacted methoxy groups for APTMS on silica gels. It was found that

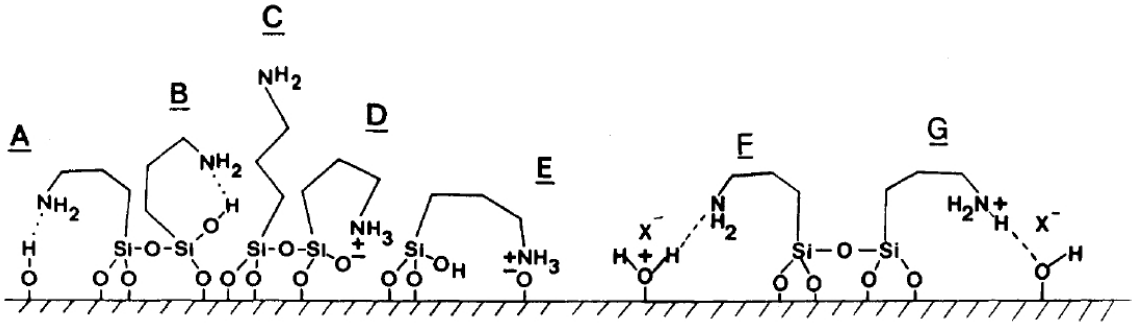

Figure 11.1: Diagram of seven possible conformations of APTMS on a silicon oxide surface. Figure reproduced from Caravajal, *et al.*, Ref. [1].

as the curing temperature increases, the average number of siloxane bonds (between the surface and neighboring silanes) increases, and the number of unhydrolyzed methoxy groups decreases. Additionally, the amount of pre-absorbed surface water was directly proportional to the amount of silicon atoms with three Si-O-Si linkages (either with the surface or with neighboring silanes) and inversely proportional to the amount of unhydrolyzed methoxy groups. It was also shown to be likely that both protonated amines and non-protonated amines could hydrogen bond to surface silanols. Due to the many possible interactions with the surface, and in light of these observations, it is postulated that APTMS can exist in at least seven conformations on a silica surface. Figure 11.1 depicts these, and it is clear that many of them are undesirable since only free amines are able to participate in further functionalization reactions.

Under some conditions, reproducible, flat, stable, homogeneous monolayer films may be produced [12]. In these studies, no investigation of the surface density or the conformation of the amines on the surface had been performed. Other researchers reported the production of very smooth and thin (either single or double layer) APTMS films on silicon by using a solution of 0.5%(vol.) APTMS in anhydrous bicyclohexyl under a nitrogen atmosphere for 15 hours [105]. In this case, high resolution XPS spectra indicate that nearly 85% of the surface amines are free, with the remainder either protonated or hydrogen bound to surface silanols.

The effect of silane concentration, reaction time, bulk water concentration, and curing temperature on the morphology and free amine content of APTMS films formed in toluene has been investigated [10]. The optimum coating procedure found in that study produced films featuring 88.6% free amine determined by XPS. Films of APTMS were compared with those formed from para-aminophenyltrimethoxysilane, which produce surfaces composed of 100% free amine. It was further demonstrated that only these free amines units are capable of participating in coupling reactions [10]. It is important to note that para-aminophenyltrimethoxysilane is not suitable for the MVD method, because the volatility requirements are not met.

Recent progress in vapor processes have routinely produced flat surfaces, but the primary amine content is low, featuring few, if any, free amine units extending from the surface. APTMS can form a penta-coordinated complex that is very sensitive to nucleophilic attack (e.g. by water), and strict control over the presence of water is required [107], and also more easily achieved with vapor processes. It has been shown that, using room temperature vapor deposition processes, all amines remain either hydrogen bonded to the surface or protonated [65, 107, 108]. With the use of catalysts that hydrogen bond to surface silanols more strongly than the amine end of APTMS, it is possible to obtain 40-50% free amine after deposition [107].

In another study, silicon wafers were exposed to the vapors above a refluxing solution of 5% APTMS in toluene and this was shown to produce smooth monolayer films [11].

It was further demonstrated that the films were unstable in protic solvents (e.g. H_2O) resulting in significant hydrolytic degradation and removal of organic molecules form the surface. It is generally found that smooth monolayers may be generated in the vapor phase at elevated temperature, but the layers contained a significant fraction of both free amines and hydrogen-bonded amines [9, 25, 26, 109].

11.2 Engineering Volatile Protected Amine Compounds–Stabase Adducts

As has been suggested by the previous review of the literature on APTMS processing and on the previous experiments outlined in section 7.4, the amine group in APTMS has a very strong tendency to hydrogen-bond with surface silanol sites. This is problematic since it places an unnecessarily low limit on the final concentration of free amine groups in the deposited films, which are required to perform further biological coupling reactions [10].

One approach to alleviate the current processing difficulties encountered with APTMS, which are due mainly to the ability of its amine end to form a strong hydrogen bond with the target surface, is to eliminate its ability to form hydrogen bonds through its amine end. This could be accomplished through chemical alteration, or blocking, of the amine end of the molecule with a labile protecting group. However, typical blocking groups employed by organic chemists are usually very large, precluding their application in vapor phase processes. As has been discussed in section 2.2.1, vapor methods are highly favorable over traditional liquid phase processes, especially for microfluidics applications, which require uniform deposition on constrained geometries with high aspect ratios.

Therefore, a low molecular weight molecule that can serve as a blocking group for the amine end of APTMS is desired. Ideally, the new compound will be sufficiently volatile to be amenable to vapor phase coating strategies, and the blocking chemistry will be reversible to enable regeneration of the amine functionality. Stabase adducts, which were first developed as a simple method for protecting alkylated amino acid derivatives, have been increasingly utilized in organic synthetic methodologies as a protecting unit for primary amines due to their stability to organolithium reagents and amide bases. Surprisingly, considering the

volatility of short chain alkylamine stabase adducts, this moiety has not been investigated in the functionalization of aminoalkyltrimethoxysilane vapor deposition processes.

To achieve the synthesis of a protected amine stabase adduct from APTMS, 1,1,4,4-tetramethyl-1,4-dichlorodisilethylene (Fig. 11.2(a)), was treated with APTMS in dichloromethane, in the presence of excess triethylamine at -20 °C. Warming to room temperature and removal of the volatiles *in vacuo* followed by vacuum distillation resulted in a clear, colorless, never before synthesized adduct (Fig. 11.2(b)) in excellent yields.

11.3 Characterization of the APTMS Stabase Adduct

Since the APTMS stabase adduct is a new compound, there is little guidance with respect to its processing properties or its infrared spectrum. Therefore, Gaussian 03 software is used to optimize the molecular geometry at the B3LYP/6-31G(d) level of theory (available in figure 11.3) and to predict the infrared spectrum. The theoretical results are then used to help interpret the experimental data. Major peaks present in the theoretical infrared spectrum, and their assignments, are presented in table 11.1. Perhaps the most important peak presented in table 11.1 is the peak at 902 cm^{-1} which is due to Si-N-Si asymmetric stretching. The presence of this strongly absorbing peak in experimental spectra should confirm the existence of the five-membered ring, and therefore the intact APTMS stabase adduct. Furthermore, dimunition of this peak with concomitant increase in absorbance from 1590–1620 cm^{-1} will confirm the regeneration of secondary, primary, and hydrogen-bonded amines, indicating the reversible nature of this blocking chemistry.

A small amount of the APTMS stabase adduct was placed onto a zinc selenide ATR crystal and left undisturbed, exposed to air. The infrared spectrum was collected over 150 minutes at 30 minute intervals. The results of this experiment are shown in figure 11.4. Negative peaks at 930 cm^{-1} and new positive features from 1590–1620 cm^{-1} confirm the breaking of the Si-N-Si bond and the formation of various amine species. These data clearly demonstrate the reversible nature of the stabase adduct blocking chemistry.

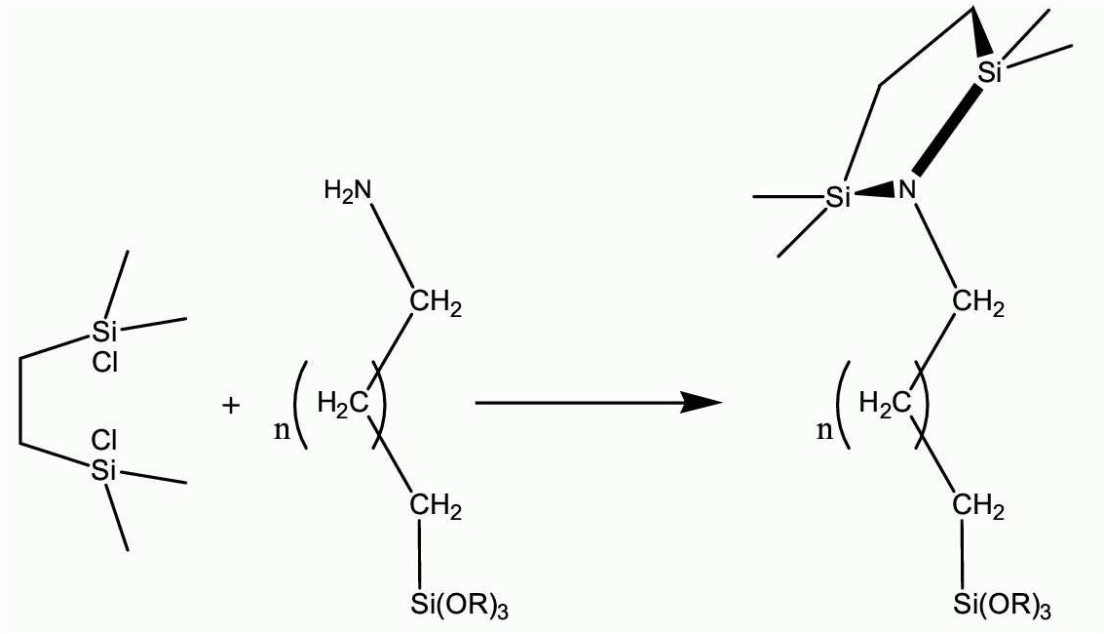

Figure 11.2: Schematic diagram of stabase adduct synthesis. The result is a stabase adduct of aminopropyltrimethoxysilane.

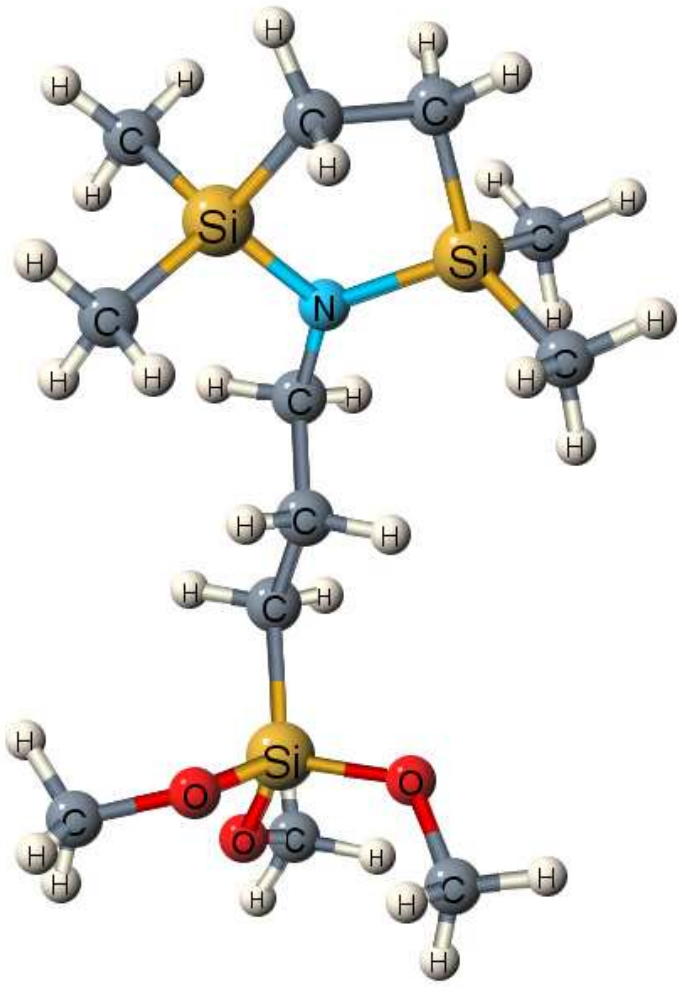

Figure 11.3: Representation of the APTMS stabase adduct after geometry optimization with Gaussian 03 software at the B3LYP/6-31G(d) level of theory.

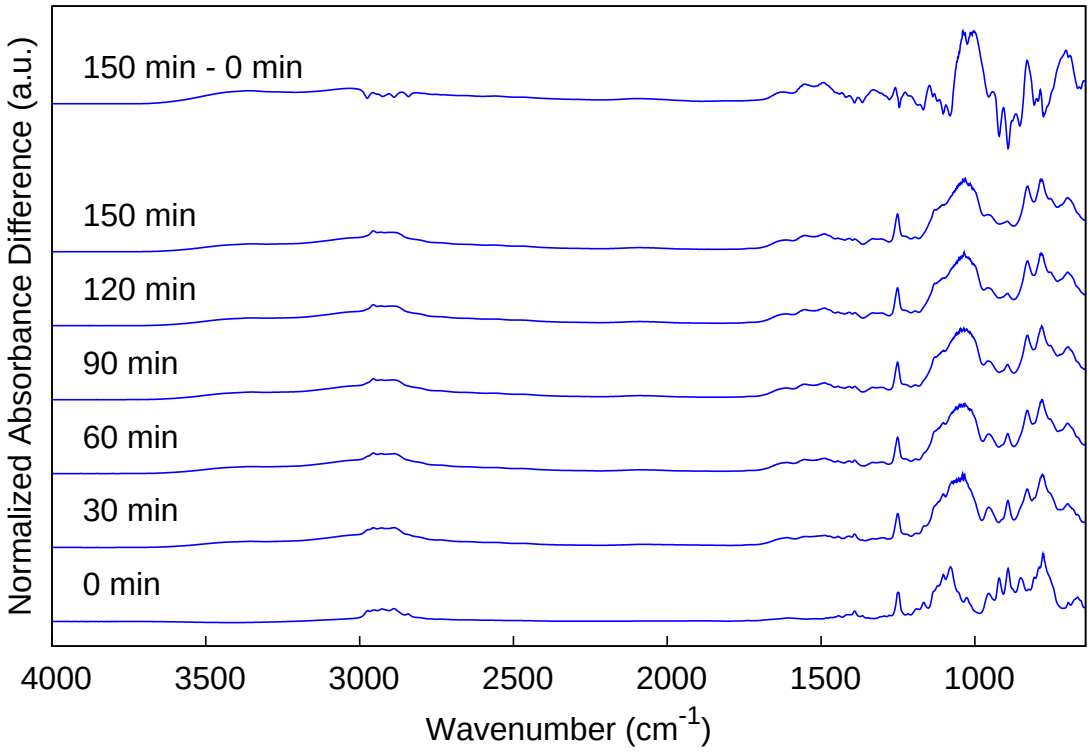

Figure 11.4: This series of infrared spectra represent the results of an experiment where the APTMS stabase adduct was placed on an ATR crystal and left undisturbed, exposed to air. Negative peaks at 930 cm^{-1} and new positive features from 1590–1620 cm^{-1} confirm the breaking of the Si-N-Si bond and the formation of various amine species.

The next step in this research project involves confirming the volatility of the APTMS stabase adduct. A small amount of the APTMS stabase adduct is loaded into a clean glass vial and degassed with multiple freeze-pump-thaw cycles with liquid nitrogen. The transmission cell described in figure 4.7 is fitted with zinc selenide optics, connected to the vapor deposition system, and is then evacuated to base pressure. The APTMS stabase adduct is heated mildly (75°C), and the vapors are allowed to enter the transmission cell. The gas phase spectrum of the APTMS stabase adduct is available in figure 11.5. As is evident in figure 11.5, the experimental spectrum agrees well with the predicted spectrum, indicating that the intact molecule is present in the vapor phase. This experiment confirms the volatility of the APTMS stabase adduct for vapor phase processing.

Next, it is desirable to verify the deposition of the APTMS stabase adduct to a model silica surface. For this purpose, a dispersion of fumed silica in methanol is prepared, and a thin film of fumed silica is deposited onto the small internal window of the transmission cell by solvent evaporation. Clean silicon samples cut from a silicon wafer are also inserted into the transmission cell, which is then placed under vacuum. The silica surface is prepared by heat treatment at 350°C for 30 minutes [51], and then allowed to cool slowly to room temperature. Then the vapors of the APTMS stabase adduct are allowed to enter the transmission cell, and the infrared spectrum is collected. Figure 11.5 shows that the intact APTMS stabase molecule (as indicated by the presence of the peak at 930 cm^{-1}) is interacting with the fumed silica surface through hydrogen bonding with surface silanols, presumably though the methoxy groups. Next, the transmission cell is vented to atmospheric pressure and heated to 115°C for 15 minutes to cause condensation reactions between methoxy groups that are hydrogen bonded to surface silanol groups [53]. Then the transmission cell is cooled slowly to room temperature, and the spectrum is collected. Figure 11.5 demonstrates that after this experiment, some hydrocarbon material remains on the fumed silica surface (peaks present from 2900–3000 cm^{-1}). However, there are spectral artifacts present due to some of the fumed silica film coming loose during the experiment which make it impossible to determine the chemical identity of the surface bound species.

Ellipsometric and contact angle analysis of the treated silicon samples *ex situ* indicates a surface coating which is ∼9Å thick with a contact angle of 87°. The thickness and contact angle data are consistent with what would be expected for monolayer deposition of the APTMS stabase adduct, although this cannot be confirmed by the FTIR spectra.

11.4 Conclusions

Synthesis and characterization of a new protected amine compound has been performed, and it has been demonstrated that the new amine compound is sufficiently volatile to be amenable to vapor phase processing. Furthermore, it has been demonstrated that the blocking chemistry utilized to create the protected amine compound is reversible, enabling regeneration of the amine. Ellipsometric and contact angle data suggest that monolayer films of the protected amine compound form on silicon surface from the vapor phase, but this result cannot be confirmed at this time by spectroscopic methods.

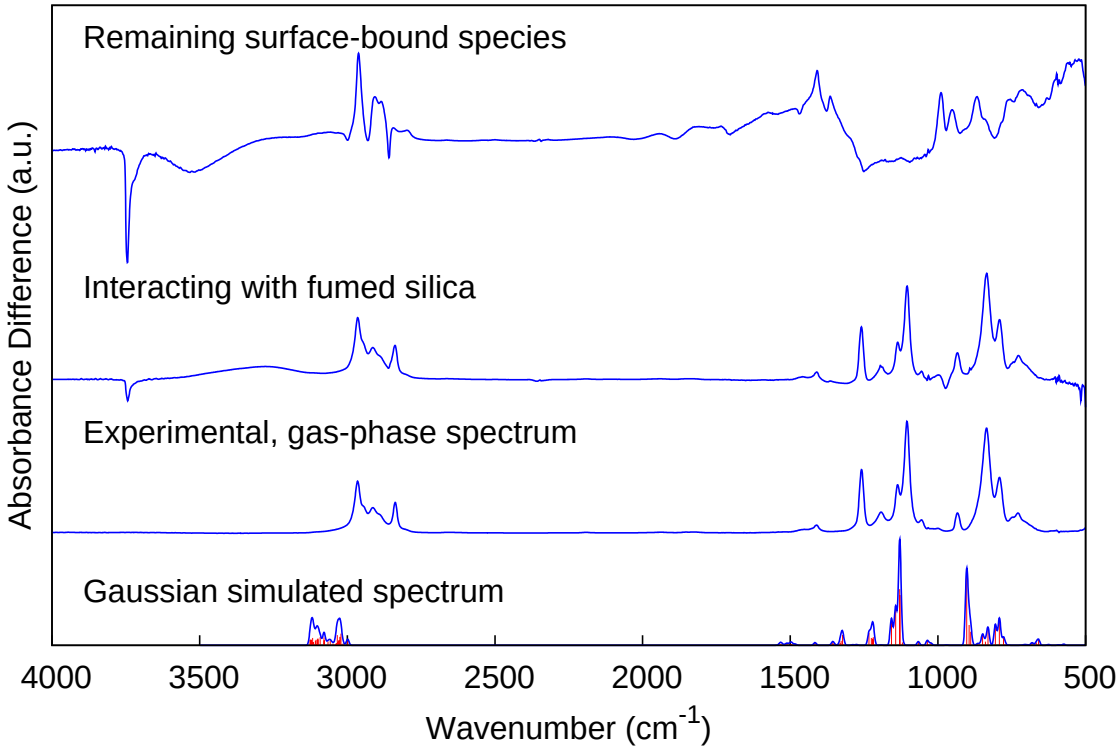

Figure 11.5: A series of transmission infrared spectra concerning the APTMS stabase adduct. The first spectrum (bottom) is the predicted infrared spectrum from Gaussian 03 simulations, and the next spectrum is the actual gas phase spectrum. Also shown is a spectrum of the APTMS stabase adduct interacting (through hydrogen bonding) with a fumed silica surface. Finally the spectrum of the remaining chemisorbed species is shown (top spectrum).

Frequency (cm^{-1})	Assignment	Relative Intensity
792	Si-C stretching in propyl segment	169
805	CH rocking modes on the 5-member ring	130
830	Si-O-C asymmetric stretching	110
848	CH rocking modes on the 5-member ring	68
889	CH twist-rock on 5-member ring	84
894	CH rocking modes on the 5-member ring	127
902	Si-N-Si asymmetric stretch	457
1128–1143	C-O stretching	240–350
1157	C-N stretching	168
1233	C-H out-of-plane bending in propyl segment	78
1322	CH bending on Si-CH_3	65
3014–3035	Symmetric and asymmetric C-H stretching	≤ 73

Table 11.1: The frequency, assignment, and relative intensity of the major vibrations for the APTMS stabase adduct, as predicted by Gaussian 03 simulations.

Chapter 12

Deposition and Characterization of Superhydrophobic Surfaces

12.1 Results and Discussion

The results of previous studies indicate that superhydrophobic surfaces can be obtained by thoughtful engineering of the surface properties, such as the surface roughness and surface energy. Pilotek and Schmidt studied the surface wettability of sol-gel derived surface coatings and characterized the wettability by dividing it into three different regimes–the smooth surface regime, the Wenzel regime, and the superhydrophobic regime–which are separated only by increasing RMS roughness of the surfaces [110]. Later on, Bravo *et al.* investigated superhydrophobic surfaces created by the layer-by-layer deposition of silica nanoparticles, and their results indicated that the transition from Wenzel wetting behavior to superhydrophobic character was a function of increasing RMS roughness of the surface, in agreement with the previous work [111].

For the wettability of surfaces prepared by the current method, however, the transition to superhydrophobic behavior is not simply a function of RMS roughness. Figure 12.1 shows AFM images of four different surfaces with similar RMS roughness values but drastically different contact angles. That the contact angle can vary so significantly with such small changes in the RMS roughness indicates that the RMS roughness, alone, is not sufficient criteria for characterizing the transition to superhydrophobic behavior for surfaces coated by the current method.

By careful examination of the images in Figure 12.1, it becomes obvious that although the RMS roughness values are similar for these surfaces, there are clear differences in the apparent surface coverage on the substrates. The idea of making a distinction between surface coverage and RMS roughness is further demonstrated in Figure 12.2. Figure 12.2

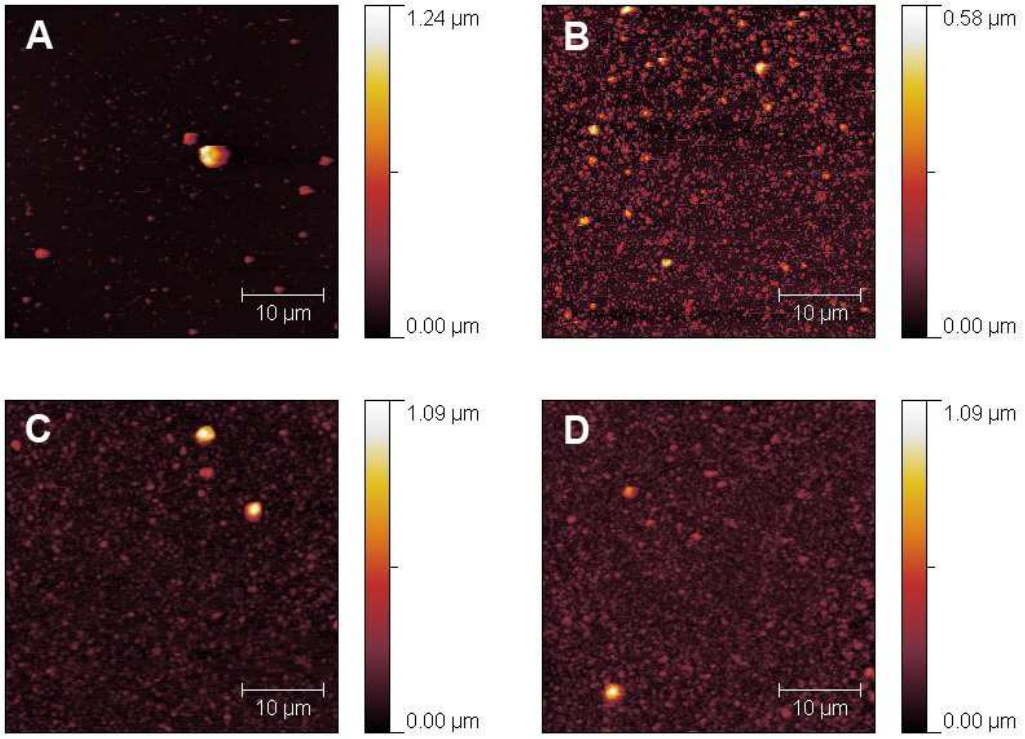

Figure 12.1: AFM micrographs of surfaces representing similar RMS roughness values but drastically different contact angles. The RMS roughness values and contact angles for the images are as follows: A) RMS = 60 nm, CA = 113°, B) RMS = 55 nm, CA = 128°, C) RMS = 63 nm, CA = 134°, D) RMS = 65 nm, CA = 157°. The authors suggest that the surface coverage for each image increases, such that the coverage for D>C>B>A, which is the same trend observed for the contact angle.

depicts two simulated surfaces with identical RMS roughness values but drastically different surface coverages. The image on the right in Figure 12.2 is composed of relatively few particles of larger height, while the image on the left is composed of many more particles of smaller height. The calculated coverage values for the left and right images are 43% and 23%, respectively. This simulation clearly demonstrates the separation of RMS roughness and surface coverage. Aditionally, the apparent surface coverage can also be thought of in terms of a roughness "quality factor," where higher quality indicates a more uniform coating.

In order to proceed in the analysis of our surfaces, a way to calculate the surface coverage was needed. Our initial attempts to extract coverage information from coated substrates relied on techniques involved with analysis and thresholding of image histograms from SEM images. For this method of extracting coverage data, the image is opened in ImageJ software. The "make binary" process, which is an implementation on the Isodata algorithm [112], is used to produce a binary representation of the original image. The Isodata algorithm is an automatic thresholding technique which analyzes an image histogram. The algorithm uses contrast-based information which it computes from the image histogram to separate the image into background and foreground components. After applying the "make binary" process, the image is composed of the background surface (white) and the foreground particles (black). Next, the "analyze particles" tool is used to determine the fraction of the total surface that is occupied by the particles, which represents the surface coverage. It is important to note that the scale bar portion of the image is not included in this analysis. Examples of results from this method are available in Figure 12.3. As is evident from the appearance of the images in Figure 12.3, there is an apparent difference in the coverage between the two surfaces, and this difference is captured quantitatively in the surface coverage calculation.

Even though the previously described method for obtaining surface coverage information from SEM images is workable, a faster method of obtaining the same information is desirable. In order to reduce the time necessary to obtain coverage information, we sought

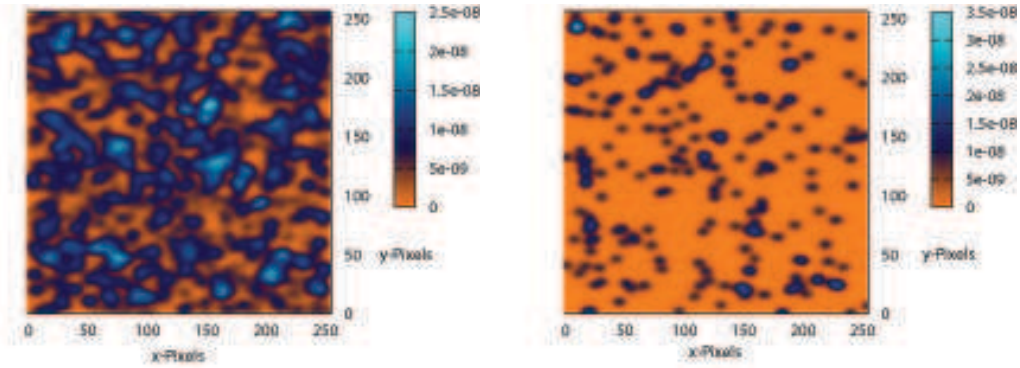

Figure 12.2: Simulated surfaces that demonstrate the concept of separate RMS roughness and surface coverage. Both surfaces have an RMS roughness value of 3.3, but the image on the left has a coverage value of 43%, while the image on the right has a coverage value of 23%.

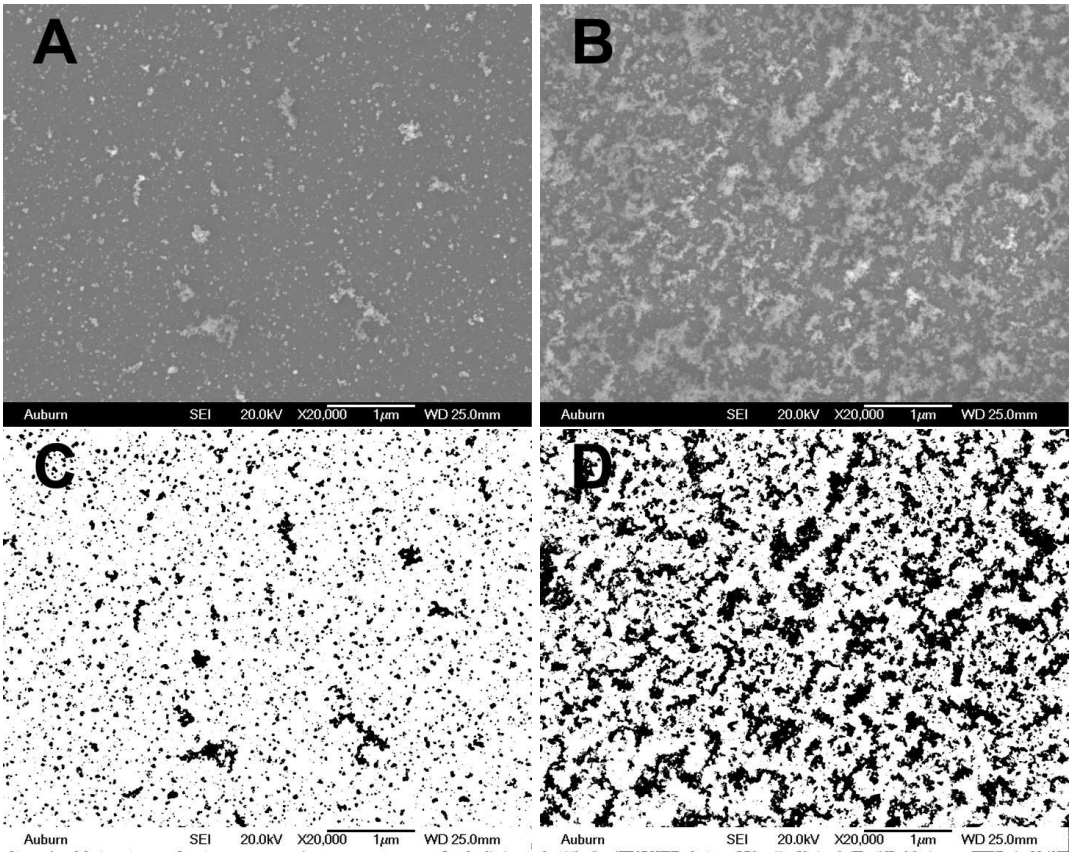

Figure 12.3: These are SEM images and their corresponding binary representations for a non-superhydrophobic sample (A and C) and a superhydrophobic sample (B and D). The coverage values are 9.3% for the non-superdhyrophobic sample and 32.9% for the superhydrophobic sample.

to develop a method of extracting similar coverage information from AFM micrographs, which would allow for elimination of the time requirements for sample preparation for SEM imaging. We also sought a calculation method that could be performed entirely by computer, without the need for human interface during the calculation process. A description of the development of that method follows.

First, AFM images are leveled in Gwyddion software by the following method: "remove polynomial background" with second order polynomials in both scan directions, "correct lines by matching height median," followed by "correct horizontal scars." This leveling process results in satisfactorily leveled AFM images for surfaces with a wide variety of starting topographies and scan qualities. After leveling is completed, the image is exported as ASCII text and a jpeg image for further analysis.

A software program has been developed to assist in the analysis of leveled AFM data. The program takes as arguments the following parameters: the ASCII filename for the AFM data, the filename of the J-PEG image of the surface, the water contact angle of the surface, and the surface's hydrophobic rank. The hydrophobic rank is a subjective, ranked assignment (on a scale of 1-4) of a surface's wetting characteristics based on observations made while measuring the water contact angle. Surfaces with a hydrophobic rank of 1 have a contact angle very similar to that observed on a smooth substrate. A rank of 2 is indicative of a surface with a slightly higher contact angle, but one with which the water drop strongly pins to the surface during contact angle measurement. A rank of three is assigned when the contact angle is high and approaching that of a superhydrophobic surface, but there is still some slight pinning of the water drop to the surface during contact angle analysis especially if the drop is pushed against the substrate. A rank of 4 is given to superhydrophobic surfaces on which there is no pinning of the water drop to the surface during contact angle measurement, even if the drop is pushed against the substrate. The program calculates the raw and refined image histogram, the RMS roughness value, and the surface coverage from the refined image histogram, as determined by an implementation of the Isodata algorithm. All of the sample properties (contact angle, superhydrophobic rank),

the computed properties (RMS roughness, histogram information, and coverage values), and a raster image of the surface are stored as a single entry in a hierarchical data format (.hdf) archive.

The calculation of the surface coverage from AFM data is not as straightforward as for obtaining the same information from SEM data. The issue is that SEM images are comprised solely of contrast information, and the difference between the lightest and darkest colors in an image is only a function of the contrast that is set by the user (or optimized by the instrument at the time of image capture). As a result, edge detection by thresholding techniques are easier to implement. AFM histograms, on the other hand, are representations of physically meaningful data, and the contrast in the image is determined by the height difference between the lowest and highest height. Therefore, in AFM images, the term "contrast" has physical significance which is different from SEM images, so edge detection techniques which rely on contrast-based information, like the Isodata algorithm, do not work as well on raw AFM data.

In order to improve on this method, we have employed the following approach, which works well. The overall goal of the approach is to expand the histogram of the AFM data, which results in improved "contrast" of the image, thereby improving performance of the Isodata algorithm. First, raw AFM data is filtered to remove outlier data. This is accomplished by removing height data from both ends of the image histogram which have fewer than 50 observations in their respective bins. It is important to note that the specification of 50 occurrences as a pre-filter criterion is the only arbitrary part of this method. Then the remaining height data is re-binned into 256 bins to construct a refined histogram. The Isodata algorithm is then applied to the refined histogram to calculate the appropriate height threshold. Once the appropriate threshold has been obtained, it is used to separate the image into background and foreground components, and the surface coverage is calculated.

Figure 12.4 show contact angle and superhydrophobic rank versus RMS roughness (top) and contact angle and superhydrophobic rank versus coverage (bottom) for prepared

surfaces. As is evident from the plots, RMS roughness is not very helpful in describing the superhydrophobic character of these surfaces given that surfaces with superhydrophobic ranks from 1-4 can be obtained at many roughness values. For instance, at an RMS roughness of 60 nm, surfaces with superhydrophobic rank of 1, 2, 3, and 4 can be obtained. On the other hand, the coverage value is much more descriptive of the superhydrophobic character of a surface since the various superhydrophobic rank values are segregated to different ranges of the coverage values. From the data, it is not possible to specify a minimum RMS roughness value required to obtain superhydrophobic character, but it is possible to do so for the coverage value. The minimum coverage value necessary for superhydrophobic character is approximately 30%.

Figure 12.5 shows a plot of RMS roughness values versus the corresponding calculated coverage values for all of the surfaces in this study. It is evident from the figure that there is no direct relationship between the RMS roughness and coverage values, which further supports the necessity for separating RMS roughness and coverage information in order to accurately and completely describe these surfaces and their superhydrophobic character.

12.2 Conclusions

It has been shown that the RMS roughness parameter alone cannot completely describe the transition from hydrophobic to Wenzel to superhydrophobic wetting characteristics, in contrast with previous reports. In this chapter, I have introduced the concept of a coverage parameter which is separate from the RMS roughness, and I have provided two methods of calculating the coverage parameter. The first method is a straightforward implementation of image analysis tools which are provided in ImageJ software, and this method is useful for extracting coverage information from SEM images. The second method, which is also an implementation of the Isodata auto-thresholding algorithm, is useful for extracting coverage information from AFM images. The key to the success of this method is in the refinement of the AFM height histogram, which allows for successful implementation of the Isodata algorithm.

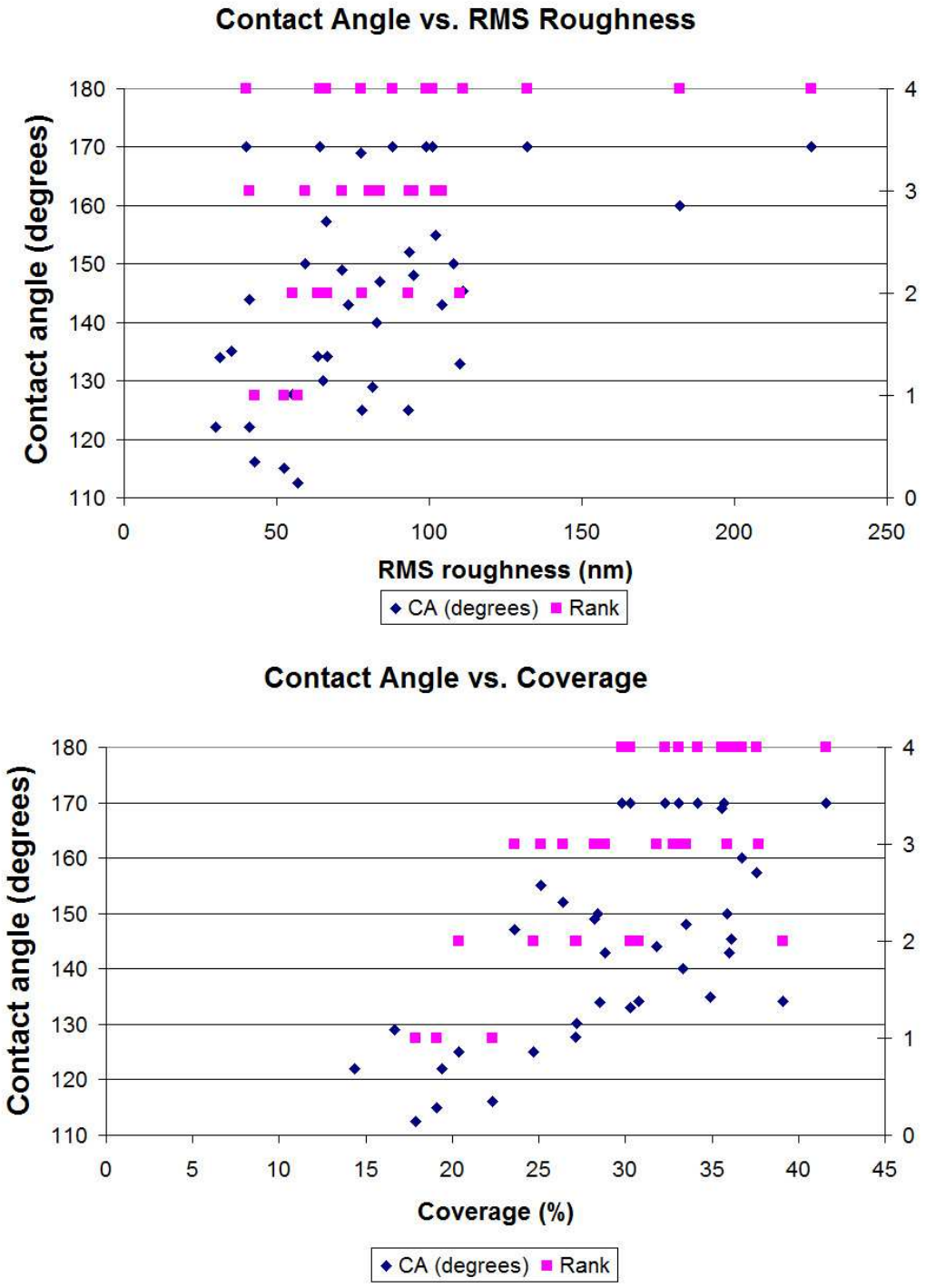

Figure 12.4: Contact angle and superhydrophobic rank versus RMS roughness (top) and contact angle and superhydrophobic rank versus coverage (bottom) for prepared surfaces. The data indicate that the contact angle and superhydrophobic character are more directly dependent on the coverage parameter than on the RMS roughness of the surface.

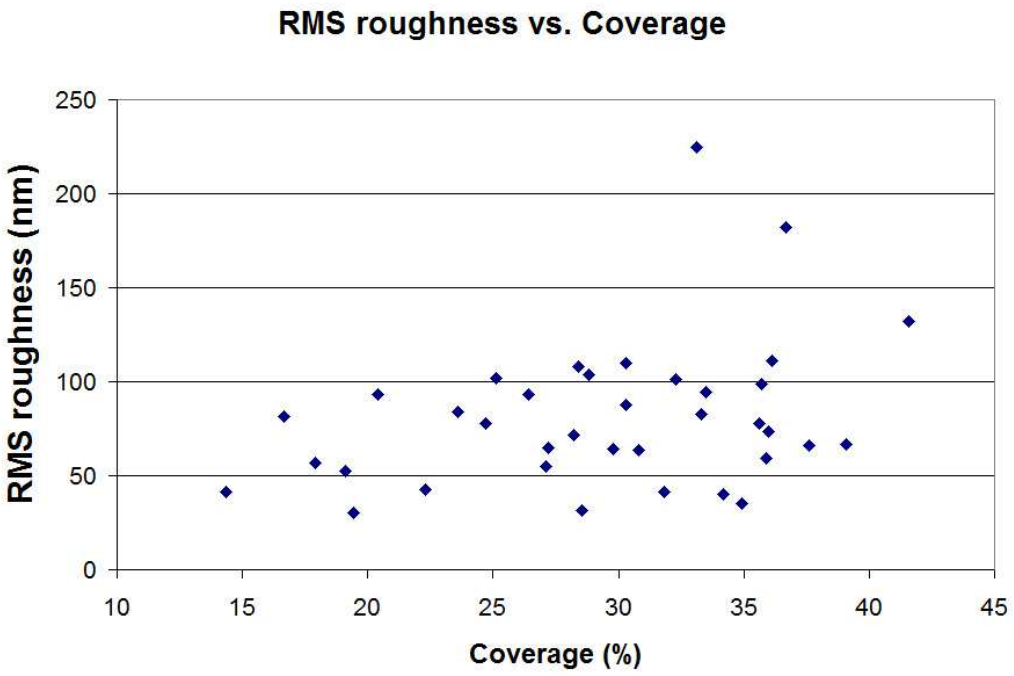

Figure 12.5: Contact angle and superhydrophobic rank versus RMS roughness (top) and contact angle and superhydrophobic rank versus coverage (bottom) for prepared surfaces. The data indicate that the contact angle and superhydrophobic character are more directly dependent on the coverage parameter than on the RMS roughness of the surface.

Chapter 13

Conclusions and Future Work

The goal of this work is to understand the chemical properties and the deposition characteristics of a silica film produced from the low temperature, vapor-phase hydrolysis of tetrachlorosilane. Although this method of creating silica films has been known for approximately fifty years, it has not been practiced extensively, and very little research has been devoted to studying its properties. This process and the film that is produced from it, when well-understood, could be leveraged to meet the pressing technological need of engineering stable surface chemistries for microfluidics applications. Since microfluidics-based devices are being increasingly fabricated from polymeric materials that are oftentimes fairly inert, there currently exist only a very limited number of technologies that are capable of achieving stable and controllable surface chemistries.

In order to achieve the stated goals of this work, a custom-made vapor deposition system was designed and built, and deposition chambers suitable for *in situ* analysis of both the vapor phase and the resultant surface by FTIR were developed and implemented. These systems enabled the analysis of the silica films in their native state, and it was determined that although the films have many commonalities with conventionally prepared silica materials, there are some important distinctions that must be made. The silica film is very highly hydroxylated when compared to conventional silicas, and as a result, all existing surface silanols participate in hydrogen bonding with neighboring silanols–there are no free surface silanols. This fact was demonstrated as an important consideration when investigating the chlorination of these groups by reaction with anhydrous tetrachlorosilane. The hydrogen bonded silanols did not participate in the chlorination reaction to the same extent as has been documented for free silanols, and this difference in reactivity allowed for the explanation of the failure of surface modification of the silica film by heterobifunctional chemistry.

Another important distinction between the silica film studied here and conventional silica materials is most likely due to its highly hydroxylated structure. These silica films undergo thermally-induced condensation of adjacent silanol groups at temperatures much lower than conventional silicas. It is generally agreed that silanol groups on conventional silicas do not undergo condensation until exposed to temperatures in excess of 170°C, but appreciable silanol condensation on the silica film was observed at temperatures as low as 100°C. In fact, at 200°C, the silica film is significantly dehydroxylated. An additional advantage of depositing silica films by this method is the ability to tune the film thickness, and perhaps more importantly, the nanotopography, by varying the pressures of the component gases during the deposition. Four very different film topographies have been obtained and characterized. Furthermore, evidence suggests that the nanotopography of the silica films may elicit responses from bacterial cells, which may lead to the development of surface which resist cellular adhesion.

Another interesting property of the silica film which arises from its highly hydroxylated structure is its ability to support an extensive, strongly hydrogen-bonded interfacial water structure. The existence of this water structure has important implications for engineering protein-resistant surfaces, and in fact, the silica film is, in many cases, protein resistant. Evidence also suggests that various different nanotopographies that can be achieved with the silica layer deposition process may afford different protein adsorption properties, which is a potentially exciting avenue of future research.

The deposition of silica films to various polymers has been performed, and it was discovered that the silica film has the ability to deposit onto a variety of substrates with remarkably different surface chemistries. Immersion studies indicate that the aqueous immersion of the silica layer is very good, but that the film may fail when adhesion to the underlying substrate is poor. Adhesion can be improved in many cases by the application of a brief oxygen plasma to activate the target surface prior to silica deposition, but this was not the case when applying silica films to PMMA surfaces. In contrast to other materials, oxygen plasma treatment of PMMA does not result in an increase in polar groups at the PMMA surface,

but rather results in etching away of the PMMA material. On every substrate studied in this work, with respect to organosilane-based surface modification processes, the silica films have behaved identically to the native oxide on silicon. This implies that this process can be used to make nearly any surface amenable to organosilane-based surface modification processes, including polymers commonly employed in microfluidics applications. Consequently, this process is poised to advance the state-of-the-art in microfluidics-based technologies by enabling, *for the first time*, the application of organosilane-based chemistries to otherwise inert polymer substrates.

Future studies from this work can be grouped into two major areas: 1) Exploiting the flexibility of this deposition method to engineer new films, and 2) further studies aimed at taking advantage of the unique properties of the silica film. Perhaps the most direct extension of the present work would be to deposit silica films on sealed microfluidics devices. Since this deposition process is a vapor phase process, the possibility of achieving uniform deposition to sealed microfluidic channels is favorable; achieving uniform deposition onto sealed microfluidic channels with conventional liquid processes is extremely difficult, if not impossible.

Additionally, this deposition method allows for the precise metering of multiple process gases, which enables one to precisely control the stoichiometry of reactants, and, by extension, products. The silica film should possess a negative charge at physiological pH, and as a result, fouling by positively charged proteins due to electrostatic interactions may become problematic. However, mixed charge films can possibly be produced by this method by incorporating a positively charged precursor, such as APTMS, during the deposition process. It is possible to imagine, then, that films with various overall charge can be designed by varying the relative pressures of tetrachlorosilane, APTMS, and water.

Unique properties of the silica film that deserve further attention are its controllable nanotopography during the deposition process, and the elimination of silanol groups by mild thermal exposure. It has been shown that both water structure, which is governed by the surface concentration of Lewis sites, and nanotopography affect protein adsorption, but

it is usually difficult to engineer both of these parameters on a single surface. The silica film offers a unique platform for protein adhesion research since the concentration of Lewis sites can be altered by thermal exposure, and the nanotopography can be chosen by using an appropriate deposition recipe.

Bibliography

[1] Caravajal, G. S., Leyden, D. E., Quinting, G. R., and Maciel, G. E. *Analytical Chemistry*, **vol. 60**: pp. 1776–1786, **1988**

[2] Ashurst, W. R., Carraro, C., and Maboudian, R. *IEEE Transactions on Device and Materials Reliability*, **vol. 3**: pp. 173–178, **2003**

[3] Ashurst, W. R., Carraro, C., Maboudian, R., and Frey, W. *Sensors And Actuators A-Physical*, **vol. 104**: pp. 213–221, **2003**

[4] Ashurst, W. R. *Surface Engineering for MEMS Reliability*. Ph.D. thesis, University of California at Berkeley, **2003**

[5] Maboudian, R., Ashurst, W. R., and Carraro, C. *Sensors and Actuators A-Physical*, **vol. 82**: pp. 219–223, **2000**

[6] Hiratsuka, A., Muguruma, H., Lee, K. H., and Karube, I. *Biosensors & Bioelectronics*, **vol. 19**: pp. 1667–1672, **2004**

[7] Nehilla, B. J., Popat, K. C., Vu, T. Q., Chowdhury, S., Standaert, R. F., Pepperberg, D. R., and Desai, T. A. *Biotechnology and Bioengineering*, **vol. 87**: pp. 669–674, **2004**

[8] Vandenberg, E. T., Bertilsson, L., Liedberg, B., Uvdal, K., Erlandsson, R., Elwing, H., and Lundstrom, I. *Journal of Colloid and Interface Science*, **vol. 147**: pp. 103–118, **1991**

[9] Kurth, D. G. and Bein, T. *Langmuir*, **vol. 9**: pp. 2965–2973, **1993**

[10] Zhang, F. X. and Srinivasan, M. P. *Langmuir*, **vol. 20**: pp. 2309–2314, **2004**

[11] Haller, I. *Journal of the American Chemical Society*, **vol. 100**: pp. 8050–8055, **1978**

[12] Petri, D. F. S., Wenz, G., Schunk, P., and Schimmel, T. *Langmuir*, **vol. 15**: pp. 4520–4523, **1999**

[13] Popat, K. C., Sharma, S., Johnson, R. W., and Desai, T. A. *Surface and Interface Analysis*, **vol. 35**: pp. 205–215, **2003**

[14] Follstaedt, S. C., Last, J. A., Cheung, D. K., Gourley, P. L., and Sasaki, D. Y. Protein Adhesion on SAM Coated Semiconductor Wafers: Hydrophobic versus Hydrophilic Surfaces. Tech. rep., Sandia National Labs., Albuquerque, NM (US); Sandia National Labs., Livermore, CA (US), **2000**

[15] Sharma, S., Johnson, R. W., and Desai, T. A. *Applied Surface Science*, **vol. 206**: pp. 218–229, **2003**

[16] Sharma, S., Popat, K. C., and Desai, T. A. *Langmuir*, **vol. 18**: pp. 8728–8731, **2002**

[17] Popat, K. C., Johnson, R. W., and Desai, T. A. *Journal of Vacuum Science & Technology B*, **vol. 21**: pp. 645–654, **2003**

[18] Makamba, H., Kim, J. H., Lim, K., Park, N., and Hahn, J. H. *Electrophoresis*, **vol. 24**: pp. 3607–3619, **2003**

[19] Cox, J. D., Curry, M. S., Skirboll, S. K., Gourley, P. L., and Sasaki, D. Y. *Biomaterials*, **vol. 23**: pp. 929–935, **2002**

[20] Peterson, S. L., McDonald, A., Gourley, P. L., and Sasaki, D. Y. *Journal of Biomedical Materials Research Part A*, **vol. 72A**: pp. 10–18, **2005**

[21] Popat, K. C., Robert, R. W., and Desai, T. A. *Surface & Coatings Technology*, **vol. 154**: pp. 253–261, **2002**

[22] Wisniewski, N., Moussy, F., and Reichert, W. M. *Fresenius Journal of Analytical Chemistry*, **vol. 366**: pp. 611–621, **2000**

[23] Auerbach, A., Soller, B., and Peura, R. In *Proceedings of the 1994 20th Annual Northeast Bioengineering Conference*, pp. 108–109, **1994**

[24] Wang, B., Abdulali-Kanji, Z., Dodwell, E., Horton, J. H., and Oleschuk, R. D. *Electrophoresis*, **vol. 24**: pp. 1442–1450, **2003**

[25] Ek, S., Iiskola, E. I., Niinisto, L., Vaittinen, J., Pakkanen, T. T., Keranen, J., and Auroux, A. *Langmuir*, **vol. 19**: pp. 10601–10609, **2003**

[26] Ek, S., Iiskola, E. I., and Niinisto, L. *Langmuir*, **vol. 19**: pp. 3461–3471, **2003**

[27] Sieburth, S. M. *Bioactive Organosilanes*, chap. 1, pp. 76–83. Gelest, **2008**

[28] de Mello, A. *Lab on a Chip*, **vol. 2**: pp. 31N–36N, **2002**

[29] Barbier, V., Tatoulian, M., Li, H., Arefi-Khonsari, F., Ajdari, A., and Tabeling, P. *Langmuir*, **vol. 22**: pp. 5230–5232, **2006**

[30] Nissen, K. E., Stuart, B. H., Stevens, M. G., and Baker, A. T. *Journal of Applied Polymer Science*, **vol. 107**: pp. 2394–2403, **2007**

[31] Hong, J. W., Studer, V., Hang, G., Anderson, W. F., and Quake, S. R. *Nature Biotechnology*, **vol. 22**: pp. 435–439, **2004**

[32] *http://www.fluidigm.com/technology/nanoflex.html*

[33] Linder, V., Verpoorte, E., Thormann, W., de Rooij, N., and Sigrist, M. *Analytical Chemistry*, **vol. 73**: pp. 4181–4189, **2001**

[34] Szunerits, S. and Boukherroub, R. *Langmuir*, **vol. 22**: pp. 1660–1663, **2006**

[35] Bannikova, A., Podvigalkina, G., and Khalezova, G. *Instruments And Experimental Techniques-USSR*, pp. 492–493, **1969**

[36] Kobrin, B., Chinn, J., and Ashurst, W. In *Technical Proceedings for the 2005 NSTI Nanotechnology Conference and trade Show*, vol. 2, **2005**

[37] Kobrin, B., Chinn, J., Ashurst, R. W., and Maboudian, R. In *Proc. SPIE Int. Soc. Opt. Eng.*, vol. 5716, pp. 151–157. SPIE, San Jose, CA, USA, **2005**

[38] Grimes, M. and Kobrin, B. *Solid State Technology*, **vol. 51**: pp. 28–31, **2008**

[39] Spanring, J., Buchgraber, C., Ebel, M., Svagera, R., and Kern, W. *Polymer*, **vol. 47**: pp. 156–165, **2006**

[40] Deng, J., Wang, L., Liu, L., and Yang, W. *Progress in Polymer Science*, **vol. 34**: pp. 156–193, **2009**

[41] Hozumi, A., Inagai, H., Yokogawa, Y., and Kameyama, T. *Thin Solid Films*, **vol. 437**: pp. 89–94, **2003**

[42] Hozumi, A., Asakura, S., Fuwa, A., Shirahata, N., and Kameyama, T. *Langmuir*, **vol. 21**: pp. 8234–8242, **2005**

[43] Fritz, J. and Owen, M. *Journal of Adhesion*, **vol. 54**: pp. 33–45, **1995**

[44] Toth, A., Bertoti, I., Blazio, M., Banhegyi, G., Bognar, A., and Szaplonczay, P. *Journal of Applied Polymer Science*, **vol. 52**: pp. 1293–1307, **1994**

[45] Bhushan, B., Hansford, D., and Lee, K. K. *Journal of Vacuum Science & Technology A*, **vol. 24**: pp. 1197–1202, **2006**

[46] Lenz, P., Ajo-Franklin, C., and Boxer, S. *Langmuir*, **vol. 20**: pp. 11092–11099, **2004**

[47] Ro, K., Chang, W., Kim, H., Koo, Y., and Hahn, J. *Electrophoresis*, **vol. 24**: pp. 3253–3259, **2003**

[48] Wu, D., Luo, Y., Zhou, X., Dai, Z., and Lin, B. *Electrophoresis*, **vol. 26**: pp. 211–218, **2005**

[49] Owen, M. J. and Smith, P. J. *Journal of Adhesion Science and Technology*, **vol. 8**: pp. 1063–1075, **1994**

[50] Chen, H.-Y., Elkasabi, Y., and Lahann, J. *Journal of the American Chemical Society*, **vol. 128**: pp. 374–380, **2006**

[51] Tripp, C. P. and Hair, M. L. *Langmuir*, **vol. 7**: pp. 923–927, **1991**

[52] Morrow, B. A., Tripp, C. P., and Mcfarlane, R. A. *Journal of the Chemical Society-Chemical Communications*, pp. 1282–1283, **1984**

[53] Anderson, A. and Ashurst, W. R. *Thin Solid Films*, **vol. 516**: pp. 7538–7546, **2008**

[54] Anderson, A. and Ashurst, W. R. *Langmuir*, **vol. 24**: pp. 7947–7954, **2008**

[55] McDonald, R. S. *Journal Of Physical Chemistry*, **vol. 62**: pp. 1168–1178, **1958**

[56] Benesi, H. A. and Jones, A. C. *Journal Of Physical Chemistry*, **vol. 63**: pp. 179–182, **1959**

[57] Socrates, G., ed. *Infrared and Raman Characteristic Group Frequencies, Tables and Charts*. John Wiley and Sons, Ltd., **2001**

[58] Marcinko, S. and Fadeev, A. Y. *Langmuir*, **vol. 20**: pp. 2270–2273, **2004**

[59] Lee, S. W. and Laibinis, P. E. *Biomaterials*, **vol. 19**: pp. 1669–1675, **1998**

[60] Peters, R., Nealey, P., Crain, J., and Himpsel, F. *Langmuir*, **vol. 18**: pp. 1250–1256, **2002**

[61] Fadeev, A. Y. and McCarthy, T. J. *Langmuir*, **vol. 16**: pp. 7268–7274, **2000**

[62] Herrmann, C. F., DelRio, F. W., Bright, V. M., and George, S. M. *Journal of Micromechanics and Microengineering*, **vol. 15**: pp. 984–992, **2005**

[63] Parker, E. E. *Microelectromechanical Systems (MEMS) Tribology in Microfluidic Environments*. Master's thesis, University of California at Berkeley, **2004**

[64] Anderson, A. and Ashurst, W. R. *Journal of Vacuum Science and Technology–A*, **vol. 26**: pp. 1357–1361, **2008**

[65] White, L. D. and Tripp, C. P. *Journal of Colloid and Interface Science*, **vol. 232**: pp. 400–407, **2000**

[66] Hair, M. *Infrared Spectroscopy in Surface Chemistry*. Marcel Dekker, Inc., **1967**

[67] Young, G. *Journal of Colloid Science*, **vol. 13**: pp. 67–85, **1958**

[68] Zhu, X. Y., Boiadjiev, V., Mulder, J. A., Hsung, R. P., and Major, R. C. *Langmuir*, **vol. 16**: pp. 6766–6772, **2000**

[69] Zhu, X. Y., Mulder, J. A., and Bergerson, W. F. *Langmuir*, **vol. 15**: pp. 8147–8154, **1999**

[70] *http://webbook.nist.gov/chemistry/*

[71] Stange, T., Mathew, R., and Evans, D. *Langmuir*, **vol. 8**: pp. 920–926, **1992**

[72] Kim, B., Peterson, E. T. K., and Papautsky, I. In *Proceedings of the 26th Annual International Conference of the IEEE EMBS*, **2004**

[73] Prosycevas, I., Tamulevicius, S., and Guobiene, A. *Thin Solid Films*, **vol. 453-54**: pp. 304–311, **2004**

[74] Vezenov, D. V., Mayers, B. T., Wolfe, D. B., and Whitesides, G. M. *Applied Physics Letters*, **vol. 86**: pp. 041104–1–041104–3, **2005**

[75] Lee, S., Shin, H.-J., Yoon, S.-M., Yi, D. K., Choi, J.-Y., and Paik, U. *Journal of Materials Chemistry*, **vol. 18**: pp. 1751–1755, **2008**

[76] Jang, J. S., Kim, S., and Lee, K. J. *Chemical Communications*, pp. 2689–2691, **2007**

[77] Arkles, B. and Larson, G. Silicon Compounds: Silanes and Silicones–A Survey of Properties and Chemistry, **2004**. Gelest catalog

[78] Qin, D. *Applied Spectroscopy*, **vol. 55**: pp. 871–876, **2001**

[79] Liang, C. Y. and Krimm, S. *Journal of Polymer Science*, **vol. 27**: pp. 241–254, **1958**

[80] Lee, J. N., Park, C., and Whitesides, G. *Analytical Chemistry*, **vol. 75**: pp. 6544–6554, **2003**

[81] Ashurst, W. R., Yau, C., Carraro, C., Maboudian, R., and Dugger, M. T. *Journal of Microelectromechanical Systems*, **vol. 10**: pp. 41–49, **2001**

[82] Vogler, E. A. *Journal Of Biomaterials Science-Polymer Edition*, **vol. 10**: pp. 1015–1045, **1999**

[83] Zheng, J., Li, L., Tsao, H.-K., Sheng, Y.-J., Chen, S., and Jiang, S. *Biophysical Journal*, **vol. 89**: pp. 158–166, **2005**

[84] Li, L., Chen, S., Zheng, J., Ratner, B., and Jiang, S. *Journal of Physical Chemistry B*, **vol. 109**: pp. 2934–2941, **2005**

[85] Vogler, E. A. *Advances in Colloid and Interface Science*, **vol. 74**: pp. 69–117, **1998**

[86] Berg, J. M., Eriksson, L. G. T., Claesson, P. M., and Borve, K. G. N. *Langmuir*, **vol. 10**: pp. 1225–1234, **1994**

[87] Alcantar, N. A., Aydil, E. S., and Israelachvili, J. *Effect of Water Plasma on Silica Surfaces: Synthesis, Characterization and Applications*, pp. 212–222. Cambridge, UK: Royal Society of Chemistry, **1999**

[88] Alcantar, N. A., Aydil, E. S., and Israelachvili, J. N. *Journal Of Biomedical Materials Research*, **vol. 51**: pp. 343–351, **2000**

[89] Anderson, A. and Ashurst, W. R., **2009**

[90] Asay, D. B. and Kim, S. H. *Journal of Physical Chemistry B*, **vol. 109**: pp. 16760–16763, **2005**

[91] Ewing, G. *Journal of Physical Chemistry B*, **vol. 108**: pp. 15953–15961, **2004**

[92] Scherer, J. R. *Advances in Infrared and Raman Spectroscopy*. Heyden: London, **1978**

[93] Downing, H. D. and Williams, D. *Journal of Geophysical Research*, **vol. 80**: pp. 1656–1661, **1975**

[94] Harrick, N. J. *Internal Reflection Spectroscopy*. Interscience Publishers, **1967**

[95] Flounders, A. W., Bell, S. A., and Hess, D. W. *Journal of the Electrochemical Society*, **vol. 140**: pp. 1414–1424, **1993**

[96] Chen, S. and Jiang, S. *Advanced Materials*, **vol. 20**: pp. 335–338, **2008**

[97] S. Shah, S., Lee, J. Y., Verkhoturov, S., Tuleuova, N., Schweikert, E. A., Ramanculov, E., and Revzin, A. *Langmuir*, **vol. 24**: pp. 6837–6844, **2008**

[98] Cha, P., Krishnan, A., Fiore, V. F., and Vogler, E. A. *Langmuir*, **vol. 24**: pp. 2553–2563, **2008**

[99] Anderson, A. and Ashurst, W. R., **2009**

[100] Sapsford, K. E. and Ligler, F. S. *Biosensors and Bioelectronics*, **vol. 19**: pp. 1045 – 1055, **2004**

[101] Sophianopoulos, A. J., Rhodes, C. K., Holcomb, D. N., and Van Holde, K. E. *Journal of Biological Chemistry*, **vol. 237**: pp. 1107–1112, **1962**

[102] Wigren, R., Elwing, H., Erlandsson, R., Welin, S., and Lundstrom, I. *FEBS Letters*, **vol. 280**: pp. 225–228, **1991**

[103] Roach, P., Farrar, D., and Perry, C. *Journal of the American Chemical Society*, **vol. 128**: pp. 3939–3945, **2006**

[104] Ostuni, E., Chapman, R. G., Holmlin, R. E., Takayama, S., and Whitesides, G. M. *Langmuir*, **vol. 17**: pp. 5605–5620, **2001**

[105] Allen, G. C., Sorbello, F., Altavilla, C., Castorina, A., and Ciliberto, E. *Thin Solid Films*, **vol. 483**: pp. 306–311, **2005**

[106] Hicks, J. C. and Jones, C. W. *Langmuir*, **vol. 22**: pp. 2676–2681, **2006**

[107] Kanan, S. A., Tze, W. T. Y., and Tripp, C. P. *Langmuir*, **vol. 18**: pp. 6623–6627, **2002**

[108] White, L. D. and Tripp, C. P. *Journal of Colloid and Interface Science*, **vol. 227**: pp. 237–243, **2000**

[109] Boerio, F. J., Wagh, V. H., and Dillingham, R. G. *Journal of Adhesion*, **vol. 81**: pp. 115–142, **2005**

[110] Pilotek, S. and Schmidt, H. K. *Journal of Sol-Gel Science and Technology*, **vol. 26**: pp. 789–792, **2003**

[111] Bravo, J., Zhai, L., Wu, Z., Cohen, R., and Rubner, M. *Langmuir*, **vol. 23**: pp. 7293–7298, **2007**

[112] Ridler, T. W. and Calvard, S. *IEEE Transactions on Systems, Man and Cybernetics*, **vol. 8**: pp. 630–632, **1978**